
Theses and Dissertations

2014

Forward physics in CMS : simulation of PMT hits in HF and Higgs mass reconstruction methods with a focus on forward jet tagging

Anthony Richard Moeller
University of Iowa

Copyright 2014 Anthony Moeller

This dissertation is available at Iowa Research Online: <http://ir.uiowa.edu/etd/4700>

Recommended Citation

Moeller, Anthony Richard. "Forward physics in CMS : simulation of PMT hits in HF and Higgs mass reconstruction methods with a focus on forward jet tagging." PhD (Doctor of Philosophy) thesis, University of Iowa, 2014.
<http://ir.uiowa.edu/etd/4700>.

Follow this and additional works at: <http://ir.uiowa.edu/etd>



Part of the [Physics Commons](#)

FORWARD PHYSICS IN CMS: SIMULATION OF PMT HITS IN HF AND
HIGGS MASS RECONSTRUCTION METHODS WITH A FOCUS ON
FORWARD JET TAGGING

by

Anthony Richard Moeller

A thesis submitted in partial fulfillment of the
requirements for the Doctor of Philosophy
degree in Physics
in the Graduate College of
The University of Iowa

May 2014

Thesis Supervisor: Professor Yasar Onel

Graduate College
The University of Iowa
Iowa City, Iowa

CERTIFICATE OF APPROVAL

PH.D. THESIS

This is to certify that the Ph.D. thesis of

Anthony Richard Moeller

has been approved by the Examining Committee for the
thesis requirement for the Doctor of Philosophy degree
in Physics at the May 2014 graduation.

Thesis Committee: _____

Yasar Onel, Thesis Supervisor

Jane Nachtman

Steven Spangler

Yannick Meurice

Mark Madsen

ACKNOWLEDGEMENTS

I would like to thank my advisor, Yasar Onel for his support during my graduate studies at the University of Iowa.

I would also like to thank the other members of my committee: Jane Nachtman, Steven Spangler, Yannick Meurice, and Mark Madsen for their support during the process of completing this thesis.

In addition, I would like to thank Ed Norbeck, who unfortunately passed away before I was able to complete and defend my thesis. Without frequent, in depth, conversations with him about my research and what exactly was required of a PhD thesis I don't know if I would have ever started writing.

And finally, I would like to thank my wife Sarah for her love and support through this entire process. Without her weekend trips with our two girls to Grandma and Grandpa's house, I never would have found the peace and quiet required to finish writing this thesis.

ABSTRACT

Abnormally high energy events were seen in the Hadronic Forward (HF) calorimeter for pion and muon data during testbeam in 2004. Analysis of testbeam data suggested that such events were caused by particles traveling the entire length of HF and striking the photomultiplier (PMT) windows in the readout box behind HF. Charged particles traversing the window of the PMT emit Cerenkov radiation, which creates abnormally high energy events in the data. To further study these events, a modification of the existing official CMS HF simulation was created that added the PMT windows to the simulation as sensitive detectors. In agreement with testbeam data, abnormally high energy events in the PMTs were seen in the simulation for muons and pions. The simulation was then extended to jets simulated with Pythia, and then for collision like events as well. PMT hits were seen in both of these cases. Energy sharing between PMTs for long and short fibers in HF as well as timing differences between normal HF events and PMT events were investigated as methods to tag such abnormal events. While both methods were somewhat successful, it was determined that they were not sufficient. The simulation was also modified to use thinner PMT windows. Reducing the thickness of the window reduced the number of PMT hits, and drastically reduced the energy of these hits, bringing most of them below standard jet energy thresholds. These results led to the replacement of the existing PMTs with new PMTs with a smaller, thinner window.

Higgs mass reconstruction methods were applied to Monte Carlo datasets for

115 and 130 GeV Higgs produced through vector boson fusion. In these datasets, the Higgs boson decayed to two tau particles, each of which decayed leptonically. The mass reconstruction methods successfully created a peak at the proper mass for both datasets. In addition to creating a Higgs, the vector boson fusion signal also has two forward jets. These jets are not found in the signal of the dominant background processes. By applying forward jet cuts to both the Higgs and the background events, it was possible to drastically improve the signal to background ratio for this channel. The Higgs boson was recently discovered at the LHC with a mass of approximately 125 GeV. As the methods discussed in this study are appropriate only for a low mass Higgs as the one discovered, they may prove useful in more precisely determining the mass of the Higgs.

TABLE OF CONTENTS

LIST OF TABLES	viii
LIST OF FIGURES	ix
CHAPTER	
1 THE LHC AND THE CMS DETECTOR	1
1.1 Introduction	1
1.1.1 A Very Brief History of Particle Discoveries	1
1.1.2 Structure of this Thesis	3
1.2 The Large Hadron Collider	3
1.2.1 The Detectors of the LHC	5
1.3 CMS	6
1.3.1 ECAL	7
1.3.2 HCAL	8
1.3.3 HF	9
1.3.4 Other subsystems	11
2 ABNORMAL EVENTS IN HF: TESTBEAM 2004	15
2.1 Abnormally High Energy Events Discovered in 2004 Testbeam Data	15
2.2 Early Attempts to Characterize Abnormal Events	16
2.3 Analysis of Abnormally High Energy Events in HF	17
2.3.1 Origin of Abnormally High Energy Events	27
2.3.2 Dataset	29
2.3.3 Energy in Long and Short Fibers	32
3 HF PMT SIMULATION	40
3.1 Modifications to original GEANT4 Simulation of HF for Studying Abnormal Events	40
3.2 Simulation of PMT Hits for Single Particles and Pythia Jets	43
3.2.1 Datasets	44
3.2.2 Long and Short Fiber Energies	44

3.2.3	PMT Hits	44
3.2.4	GenJets and RecJets for Pythia Jets	46
3.2.5	Timing	48
3.2.6	$S/(L+S)$	54
3.2.7	$(L-S)/(L+S)$	56
3.3	Simulation of PMT Hits for Minimum	
Bias Events		58
3.3.1	Datasets	58
3.3.2	PMT Hits	59
3.3.3	RecJet Distributions	59
3.3.4	Timing	61
3.3.5	$(L-S)/(L+S)$	67
3.4	Comparison of Two Different PMT	
Window Thicknesses		67
3.4.1	Datasets	67
3.4.2	PMT Hits	69
3.4.3	RecJet Distributions	69
3.5	Discussion of HF PMT Simulation Results	71
4	VECTOR BOSON FUSION HIGGS	74
4.1	The Standard Model	74
4.2	The Higgs Boson	75
4.3	Vector Boson Fusion	77
4.3.1	Higgs Decay Products	77
4.4	Data Set	79
4.5	The $qqH \rightarrow \tau \tau \rightarrow$ Leptons Signal	80
5	MASS RECONSTRUCTION METHODS	84
5.1	Higgs Mass Reconstruction	84
5.1.1	Method 1	85
5.1.2	Method 2	86
6	FORWARD JET TAGGING	89
6.1	Forward Jets	89
6.2	Combining Forward Jet Tagging with	
Mass Reconstruction Methods		91
7	APPLYING MASS RECONSTRUCTION METHODS AND FORWARD	
JET TAGGING TO BACKGROUNDS		97

7.1	Use of Forward Jet Tagging to Reduce Background	97
7.2	Discussion of Method 2 and Forward Jet Tagging	98
8	CMS RESULTS: THE HIGGS BOSON	101
8.1	Experimental Results	101
8.2	Nobel Prize for Englert and Higgs	102
9	TYING IT ALL TOGETHER: A BRIEF STUDY ON THE IMPOR- TANCE OF HF TO FORWARD JET TAGGING	107
9.1	Conclusion: HF PMT Hits	107
9.2	Conclusion: Higgs Mass Reconstruction Methods	108
9.3	A Connection between Chapters 2-3 and 4-8	110
9.4	Forward Jets from $qqH \rightarrow \tau \tau \rightarrow$ Leptons Signal in HF	111
	REFERENCES	114

LIST OF TABLES

Table	
2.1	Test beam runs used for early characterization of abnormal events. Cuts made on this data were intended to eliminate muons. 16
2.2	Beam type, energy, and run numbers used for $\frac{S}{L+S}$ analysis. 31
3.1	Events eliminated for both PMT and normal events when all events with hits of less than 46, 47, 48, 49, or 50 ns are rejected. 52
3.2	Number of events per dataset. 58
3.3	Events eliminated for both PMT and normal events when all events with hits of less than 46, 47, 48, 49, or 50 ns are rejected. 65
5.1	Number of events per file, as well as the number of Higgs mass reconstructions for Method 1 and Method 2 using generator level information. 88
7.1	Number of events remaining after p_T cuts on jets for signal and backgrounds. 99
7.2	Number of events expected in 30 fb^{-1} of data for various jet p_T cuts. Note that for both Higgs entries, the cross section given is actually the cross section times the branching ratio for the leptonic decay channel of interest to this study. 99
7.3	Significance for 115 and 130 GeV datasets with backgrounds $S = \sqrt{2 \ln Q}$, $Q = (1 + \frac{N_S}{N_B})^{N_S + N_B} e^{-N_S}$ (30 GeV jet p_T cut). 100
9.1	Forward jet pairs from Higgs mass reconstruction study which have at least one jet in the HF region. The colors in the first column refer to Figure 9.1 113

LIST OF FIGURES

Figure		
1.1	Schematic of major LHC components	4
1.2	The CMS coordinate system. The z axis is along the beamline and the pseudorapidity is defined as $\eta = -\ln \tan(\theta/2)$	7
1.3	The CMS Detector.	8
1.4	Photograph of HF wedge.	12
1.5	Cross sectional schematic of individual HF wedge.	13
1.6	HF tower numbers and η values for an individual wedge. Each tower reads out to two PMTs with one PMT for the short fibers and another for the long fibers.	14
2.1	Data recorded for 30 GeV electron beams. Top: Energy in long fibers. Middle: Energy in short fibers. Bottom: Scatter plot of energy in short fibers vs. energy in short fibers.	18
2.2	Data recorded for 50 GeV electron beams. Top: Energy in long fibers. Middle: Energy in short fibers. Bottom: Scatter plot of energy in short fibers vs. energy in short fibers.	19
2.3	Data recorded for 100 GeV electron beams. Top: Energy in long fibers. Middle: Energy in short fibers. Bottom: Scatter plot of energy in short fibers vs. energy in short fibers.	20
2.4	Data recorded for 150 GeV electron beams. Top: Energy in long fibers. Middle: Energy in short fibers. Bottom: Scatter plot of energy in short fibers vs. energy in short fibers.	21
2.5	Data recorded for 30 GeV pion beams. Top: Energy in long fibers. Middle: Energy in short fibers. Bottom: Scatter plot of energy in short fibers vs. energy in short fibers.	22

2.6	Data recorded for 50 GeV pion beams. Top: Energy in long fibers. Middle: Energy in short fibers. Bottom: Scatter plot of energy in short fibers vs. energy in short fibers.	23
2.7	Data recorded for 100 GeV pion beams. Top: Energy in long fibers. Middle: Energy in short fibers. Bottom: Scatter plot of energy in short fibers vs. energy in short fibers.	24
2.8	Data recorded for 150 GeV pion beams. Top: Energy in long fibers. Middle: Energy in short fibers. Bottom: Scatter plot of energy in short fibers vs. energy in short fibers.	25
2.9	Channels with abnormal events for 100 GeV pions. The numbers indicate the number of abnormal events in each tower for long and short fibers. .	26
2.10	A picture of the HF PMT glass section. The glass shape is plano-convex and the thickness in the center (1 mm) increases towards the edges (6.1 mm). Interaction of relativistic particles with glass create Cerenkov photons.	29
2.11	Muons produce a large signal when they hit the PMT glass. The location and periphery of the PMT window can be seen clearly by a 150 GeV muon beam (left). The energy measured from PMT events is on the order of 100 GeV as expected (right).	30
2.12	Normal 300 GeV pions, $\frac{S}{L+S}$	34
2.13	Fraction of events cut when all events outside of Δ Cut from the mean of the plot to the left are rejected.	34
2.14	Abnormal 300 GeV pions, all channels, $\frac{S}{L+S}$	35
2.15	Fraction of events cut when all events outside of Δ Cut from the mean of $\frac{S}{L+S}$ for normal 300 GeV pions are rejected.	35
2.16	Normal 100 GeV pions, $\frac{S}{L+S}$	35
2.17	Fraction of events cut when all events outside of Δ Cut from the mean of the plot to the left are rejected.	35
2.18	Abnormal 100 GeV pions, all channels, $\frac{S}{L+S}$	36
2.19	Fraction of events cut when all events outside of Δ Cut from the mean of $\frac{S}{L+S}$ for normal 100 GeV pions are rejected.	36

2.20	Normal 150 GeV muons, $\frac{S}{L+S}$	36
2.21	Fraction of events cut when all events outside of Δ Cut from the mean of the plot to the left are rejected.	36
2.22	Abnormal 150 GeV muons, all channels, $\frac{S}{L+S}$	37
2.23	Fraction of events cut when all events outside of Δ Cut from the mean of $\frac{S}{L+S}$ for normal 150 GeV muons are rejected.	37
2.24	Normal 50 GeV electrons, $\frac{S}{L+S}$. (There are no abnormal events for 50 GeV electrons.)	37
2.25	Fraction of events cut when all events outside of Δ Cut from the mean of the plot to the left are rejected.	37
2.26	Normal 100 GeV electrons, $\frac{S}{L+S}$	38
2.27	Fraction of events cut when all events outside of Δ Cut from the mean of the plot to the left are rejected.	38
2.28	Abnormal 100 GeV electrons, all channels, $\frac{S}{L+S}$	38
2.29	Fraction of events cut when all events outside of Δ Cut from the mean of $\frac{S}{L+S}$ for normal 100 GeV electrons are rejected.	38
3.1	Diagram of HF. The readout box (indicated by the red box) is located at $3 \leq \eta \leq 3.2$. The red arrow represents particles passing through HF coming from the direction of the interaction point.	40
3.2	A conceptual diagram showing the disks which simulate the PMT windows in the modified HF simulation.	41
3.3	Energy in long and short fibers (depths 1 and 2, respectively) for 100 GeV Pions. Energies are in photoelectrons.	45
3.4	Energy in long and short fibers (depths 1 and 2, respectively) for 100 GeV Electrons. Energies are in photoelectrons.	45
3.5	Energy in PMTs for 150 GeV Muons. Energy in photoelectrons. The red line is a gaussian fit of the peak only ($30 \text{ p.e.} < \text{energy} < 70 \text{ p.e.}$).	46

3.6	Energy in PMTs for 100 GeV Pions. Energy in photoelectrons. The red line is a gaussian fit of the peak only (30 p.e. < energy < 70 p.e.).	47
3.7	Energy in PMTs for 50 GeV p_T Pythia Jets. Energy in photoelectrons. The red line is a gaussian fit of the peak only (30 p.e. < energy < 70 p.e.).	47
3.8	p_T of GenJets for 50 GeV p_T Pythia Jets.	48
3.9	p_T of leading RecJet for 50 GeV p_T Pythia Jets. The left figure includes PMT events, the right figure does not.	49
3.10	Timing information for 100 GeV Electrons. Pcalohit time on the left, rechit time on the right. Time in ns.	50
3.11	Timing information for 150 GeV Muons. PMT hits are indicated by the green line. Pcalohit time on the left, rechit time on the right. Time in ns.	50
3.12	Timing information for 100 GeV Pions. PMT hits are indicated by the green line. Pcalohit time on the left, rechit time on the right. Time in ns.	51
3.13	Timing information for 50 GeV p_T Pythia Jets. PMT hits are indicated by the green line. Pcalohit time on the left, rechit time on the right. Time in ns.	51
3.14	Total ADC counts for 150 GeV Muons. Non-PMT events on the left, PMT events on the right.	53
3.15	Total ADC counts 100 GeV Pions. Non-PMT events on the left, PMT events on the right.	53
3.16	Total ADC counts for 50 GeV p_T Pythia Jets. Non-PMT events on the left, PMT events on the right.	53
3.17	S/(L+S) for 100 GeV electrons. Testbeam on the left [28], simulation on the right.	54
3.18	S/(L+S) for 150 GeV muons, testbeam. "Normal" events on the left, "Abnormal" events on the right [28].	55
3.19	S/(L+S) for 150 GeV muons, simulation. Non-PMT events on the left, PMT events on the right.	55
3.20	S/(L+S) for 100 GeV pions, testbeam. "Normal" events on the left, "Abnormal" events on the right [28].	55

3.21	S/(L+S) for 100 GeV pions, simulation. Non-PMT events on the left, PMT events on the right.	56
3.22	(L-S)/(L+S) for 100 GeV electrons.	57
3.23	(L-S)/(L+S) for 150 GeV muons. Non-PMT events on the left, PMT events on the right.	57
3.24	(L-S)/(L+S) for 100 GeV pions. Non-PMT events on the left, PMT events on the right.	57
3.25	(L-S)/(L+S) for 50 GeV p_T Pythia Jets. Non-PMT events on the left, PMT events on the right.	58
3.26	Energy in PMTs for 7 TeV minimum bias events. Energy in photoelectrons. The red line is a gaussian fit of the peak only (30 p.e. < energy < 70 p.e.)	60
3.27	Energy in PMTs for 10 TeV minimum bias events. Energy in photoelectrons. The red line is a gaussian fit of the peak only (30 p.e. < energy < 70 p.e.)	60
3.28	Energy in PMTs for 14 TeV minimum bias events. Energy in photoelectrons. The red line is a gaussian fit of the peak only (30 p.e. < energy < 70 p.e.)	61
3.29	p_T of RecJets for 7 TeV minimum bias events. The solid blue line is the leading RecJet p_T for all events, the dotted red line excludes PMT hit events.	62
3.30	p_T of RecJets for 10 TeV minimum bias events. The solid blue line is the leading RecJet p_T for all events, the dotted red line excludes PMT hit events.	62
3.31	p_T of RecJets for 14 TeV minimum bias events. The solid blue line is the leading RecJet p_T for all events, the dotted red line excludes PMT hit events.	62
3.32	Timing information for 7 TeV minimum bias events. Pcalohit time on the left, rechit time on the right. Time in ns.	63
3.33	Timing information for 10 TeV minimum bias events. PMT hits are indicated by the green line. Pcalohit time on the left, rechit time on the right. Time in ns.	64

3.34	Timing information for 14 TeV minimum bias events. PMT hits are indicated by the green line. Pcalohit time on the left, rechit time on the right. Time in ns.	64
3.35	Total ADC counts for 7 TeV minimum bias events. Non-PMT events on the left, PMT events on the right.	66
3.36	Total ADC counts for 10 TeV minimum bias events. Non-PMT events on the left, PMT events on the right.	66
3.37	Total ADC counts for 14 TeV minimum bias events. Non-PMT events on the left, PMT events on the right.	67
3.38	(L-S)/(L+S) for 7 TeV minimum bias events. Non-PMT events on the left, PMT events on the right.	68
3.39	(L-S)/(L+S) for 10 TeV minimum bias events. Non-PMT events on the left, PMT events on the right.	68
3.40	(L-S)/(L+S) for 14 TeV minimum bias events. Non-PMT events on the left, PMT events on the right.	68
3.41	Energy in PMTs for 150 GeV muons. Results for the 6 mm window on the left, 0.6 mm window on the right. Energy in photoelectrons. The red line is a gaussian fit of the peak only.	70
3.42	Energy in PMTs for 50 GeV p_T Pythia jets. Results for the 6 mm window on the left, 0.6 mm window on the right. Energy in photoelectrons. The red line is a gaussian fit of the peak only.	70
3.43	Energy in PMTs for 7 TeV minimum bias events. Results for the 6 mm window on the left, 0.6 mm window on the right. Energy in photoelectrons. The red line is a gaussian fit of the peak only.	70
3.44	p_T of RecJets for 50 GeV Pythia jets. Results for the 6 mm window on the left, 0.6 mm window on the right. The solid blue line is the leading RecJet p_T for all events, the dotted red line excludes PMT hit events.	71
3.45	p_T of RecJets for 7 TeV minimum bias events. Results for the 6 mm window on the left, 0.6 mm window on the right. The solid blue line is the leading RecJet p_T for all events, the dotted red line excludes PMT hit events.	72
4.1	The Standard Model.	76

4.2	Higgs cross section for various production mechanisms as a function of Higgs mass. Of particular note are gluon fusion (shown on graph as $gg \rightarrow H$) and vector boson fusion (shown on graph as $qq \rightarrow Hqq$.)	78
4.3	Feynman diagram of a vector boson fusion higgs decaying into two tau particles.	78
4.4	η of generated leptons for 115 and 130 GeV Higgs boson decaying to taus.	81
4.5	p_T of generated leptons for 115 and 130 GeV Higgs boson decaying to taus.	81
4.6	η of reconstructed leptons for 115 and 130 GeV Higgs decaying to taus. .	82
4.7	p_T of reconstructed leptons for 115 and 130 GeV Higgs decaying to taus.	82
4.8	Generator level \cancel{p}_T (indicated as Gen MET Pt on the graph) for 115 and 130 GeV Higgs decaying to taus.	82
4.9	Reconstructed level \cancel{p}_T (indicated as Rec MET Pt on the graph) for 115 and 130 GeV Higgs decaying to taus.	83
5.1	Angle (in degrees) between generator level leptons and neutrinos for 115 and 130 GeV Higgs.	85
5.2	Mass reconstruction of 115 and 130 GeV Higgs using generated leptons and \cancel{E}_T , Method 1.	87
5.3	Mass reconstruction of 115 and 130 GeV Higgs using generated leptons and \cancel{E}_T , Method 2.	87
5.4	Dilepton mass for 115 and 130 GeV Higgs from generated leptons.	87
5.5	X_1 and X_2 (labeled as X_a and X_b in figure) for 115 and 130 GeV Higgs from generated leptons and \cancel{E}_T	88
6.1	p_T of reconstructed jets for 115 and 130 GeV Higgs.	90
6.2	η of forward jets for 115 and 130 GeV Higgs.	90
6.3	Multiplicity of reconstructed leptons (PID=11 corresponds to electrons, 13 to muons).	93
6.4	Dilepton mass for 115 and 130 GeV Higgs from reconstructed leptons. . .	93

6.5	X_1 and X_2 (labeled as X_a and X_b in figure) for 115 and 130 GeV Higgs from reconstructed leptons and \cancel{E}_T	94
6.6	Results of forward jet p_T cuts on Higgs mass reconstruction (115 GeV Higgs, Method 2). The top left histogram does not make use of forward jet cuts. For the remaining three histograms, jet $\Delta\eta > 4.5$, and $\eta_{j1}\eta_{j2} < 0$. The top right histogram is for jet $p_T > 10$ GeV, bottom left for jet $p_T > 20$ GeV, and the bottom right for jet $p_T > 30$ GeV.	95
6.7	Results of forward jet p_T cuts on Higgs mass reconstruction (130 GeV Higgs, Method 2). The top left histogram does not make use of forward jet cuts. For the remaining three histograms, jet $\Delta\eta > 4.5$, and $\eta_{j1}\eta_{j2} < 0$. The top right histogram is for jet $p_T > 10$ GeV, bottom left for jet $p_T > 20$ GeV, and the bottom right for jet $p_T > 30$ GeV.	96
6.8	Mass of 115 GeV and 130 GeV Higgs using Method 2, gen level and rec level results superimposed on same histogram. The y axis is in arbitrary units.	96
7.1	This stack plot shows the result of applying the mass reconstruction method to the background processes in the Higgs search.	98
7.2	Reconstructed mass of the Higgs and backgrounds in GeV. The left figure is with minimal cuts while the right figure includes jet based cuts.	100
8.1	Di-photon mass for Higgs decay to two photons.	103
8.2	Four-lepton mass for Higgs decay to ZZ to four leptons.	104
8.3	Di-lepton mass for Higgs decay to WW to two leptons.	105
8.4	Di-tau mass for Higgs decay to two taus.	106
8.5	Combined confidence level for multiple Higgs decay channels.	106
9.1	Total cross section for single and double Higgs boson production for various production mechanisms as a function of collision energy for a Higgs mass of 120 GeV.	110
9.2	Forward jets from Higgs mass reconstruction study.	112

CHAPTER 1

THE LHC AND THE CMS DETECTOR

1.1 Introduction

1.1.1 A Very Brief History of Particle Discoveries

Particle accelerators have allowed physicists to probe the fundamental nature of matter at the most basic level, but such discoveries have only been made in relatively recent history. J.J. Thomson discovered the electron in 1897 [1] using a cathode ray tube, which is simply a very primitive particle accelerator which accelerates a beam of particles between two electrodes with a potential difference between them. This beam is then manipulated using electric and magnetic fields [2]. Although more modern particle accelerator designs were developed in the 1920s, most particle discoveries in the period 1930-1950 came from cosmic ray studies, as the beam energies were quite low. Some of these discoveries included the muon in 1937 [3] as well as the pion [4], [5] and kaon [6] in 1947.

Cosmic ray studies were not sufficient to discover more massive particles such as the antiproton (938 MeV). A discovery such as this required a particle accelerator with enough energy to create both a proton and an antiproton at the same time. In general, as newer, higher energy accelerators were developed, new physics discoveries followed. Construction on a new particle accelerator, the Bevatron, began in 1949 at The University of California Radiation Laboratory at Berkeley. The first beam at the full energy of 6.2 GeV was delivered on April 1, 1954 [7]. The antiproton was

discovered shortly after in 1955 [8].

The Stanford Linear Accelerator (SLAC) began operation in 1966 with a 30 GeV electron beam. In 1969 the up, down, and strange quarks were discovered at SLAC [9], [10]. In 1974 the J/Ψ was discovered independently at both SLAC and Brookhaven, which proved the existence of the charm quark [11], [12]. The discovery of the tau soon followed in 1975, also at SLAC [13].

The bottom quark was discovered through the observation of the upsilon (the bound state of the bottom quark and its corresponding anti-particle). It was discovered in 1977 at the Fermilab's Proton Center fixed target area [14].

The Super Proton Synchrotron (SPS) opened at CERN in 1976 with an energy of 400 GeV. The W and Z bosons were discovered here in 1983 [15], [16]. The SPS is still in operation as the proton injector for the Large Hadron Collider (LHC)(see the next section for more about the LHC).

The Tevatron was completed at Fermilab in Batavia, Illinois in 1983. By the end of 1986 it was colliding protons and anti-protons at an energy of 1.8 TeV in its 6.86 km ring. The top quark, the last quark to be discovered, was found at the Tevatron in 1995 [17], [18]. The Tevatron was shut down in 2011.

That brings us to the Large Hadron Collider and the search for the Higgs Boson, which will be discussed later in this work.

The above is only a highlight of the discoveries in particle physics over the past 120 years, and is in no way intended to be a complete list of all influential discoveries or accelerators.

1.1.2 Structure of this Thesis

This thesis contains studies of two topics regarding high energy physics. The remainder of the current chapter will discuss the Large Hadron Collider as well as the CMS detector, which are relevant to both topics. The first topic is a study on forward detector performance utilizing computer simulations and testbeam data from the initial testing of the detector. This study is presented in Chapters 2-3. The second topic explores mass reconstruction methods in the search for the Higgs Boson, which will be discussed in Chapters 4-8. Finally, Chapter 9 will present a brief study that shows how these two rather different topics are actually quite related.

1.2 The Large Hadron Collider

The Large Hadron Collider (LHC) is located at the European Organization for Nuclear Research (CERN). At the time of this work, it is the world's largest particle accelerator. The CERN council voted to approve the construction of the LHC in December of 1994, and it was started up for the first time almost fourteen years later in September of 2008 [19]. The LHC is located in a 27 km ring buried under the French and Swiss countryside. At its maximum design energy, it will collide protons at a center of mass energy of 14 TeV. The LHC is also capable of colliding lead ions at up to 2.76 TeV, but a description of heavy ion collisions is beyond the scope of this particular work.

The following is a brief description of the steps in which the opposing proton beams are accelerated up to their full energy before they collide. For a more detailed

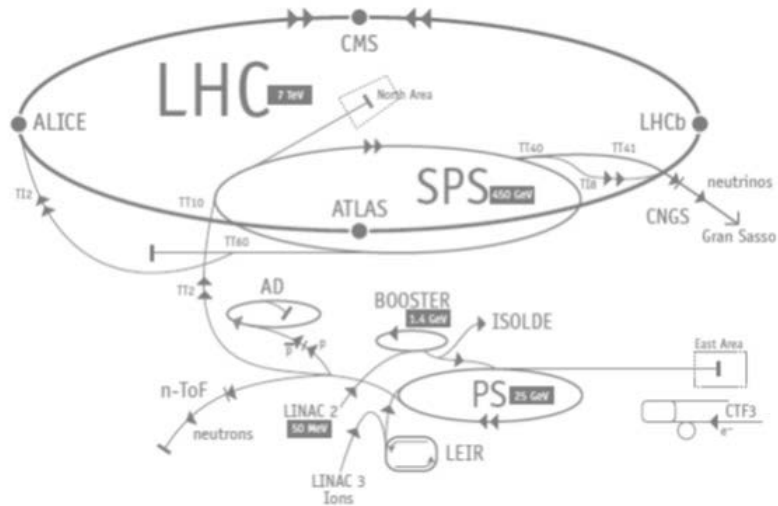


Figure 1.1: Schematic of major LHC components [19].

account of the design and operation of the LHC, see [20], [21] and [22]. For a schematic of the major components of the LHC, see Figure 1.1.

The process of accelerating the proton beams begins with ordinary hydrogen. The electrons are stripped from the hydrogen to obtain protons. The protons are accelerated to 50 MeV in Linac2. The proton beam from Linac2 is then injected in the PS Booster (PSB), where they are accelerated to 1.4 GeV. This beam then moves on to the Proton Synchrotron (PS) where the protons are accelerated to 25 GeV. The beam is then injected into the Super Proton Synchrotron (SPS) where the protons are accelerated one more time before being injected into the LHC at 450 GeV, both in clockwise and anticlockwise directions. These opposing proton beams are then accelerated to their full energy inside the LHC using RF cavities. Once the protons are accelerated to full energy, these cavities keep the energy constant by compensating

for energy losses. The beams are kept in a circular orbit by superconducting dipole magnets, and are focused by superconducting quadrupole magnets [19].

The beams then collide at four points along the ring, each one corresponding to the location of one of the four major detectors installed at the LHC.

1.2.1 The Detectors of the LHC

The ATLAS (A Toroidal LHC Apparatus) experiment is a general-purpose detector designed to search for physics such as the Higgs boson, Extra Dimensions, and Dark Matter. ATLAS is located 100 m underground, weighs 7000 tons, is 46 m long, 25 m high, and 25 m wide.

ALICE (A Large Ion Collider Experiment) is a detector designed for use during the periods when the LHC is colliding lead ions instead of protons. One of its primary objectives is to investigate quark-gluon plasma. Quark-gluon plasma is a theorized state of matter at high temperatures and/or high densities in which quarks and gluons are not confined by strong force interactions. ALICE weighs 10,000 tons, is 26 m long, 16 m high and 16 m wide.

LHCb (Large Hadron Collider beauty) is an experiment that studies "beauty" quarks (more commonly known as "bottom" quarks) to investigate the differences between matter and antimatter. LHCb weighs 5600 tons, is 21 m long, 10 m high, and 13 m wide.

The remainder of this work is associated with the CMS (Compact Muon Solenoid) experiment, which will receive a more thorough description in the following

section.

There are also two smaller experiments which are situated near the collision points for the other detectors. TOTEM (Total elastic and diffractive cross-section measurement) is a forward particle detector located near the CMS detector. LHCf (Large Hadron Collider forward) uses the particles resulting from LHC collisions to simulate cosmic rays and is located near ATLAS.

1.3 CMS

CMS is a general purpose detector which was designed to investigate physics topics including, but not limited to, the Higgs boson, Supersymmetric particles, new massive vector bosons, heavy-ion physics (during those periods when the LHC will be colliding lead ions instead of protons), as well as such standard model physics topics as QCD, electroweak, and flavor physics.

Figure 1.3 shows the major components of the CMS detector. As can be seen from the people added to the drawing to help indicate the scale of the detector, CMS is very large. It is 21.6 m long, has a diameter of 14.6 m, and weighs 12,500 tons. Inside the detector is a 13 m long 5.9 m diameter superconducting solenoid which produces a magnetic field of 4 T. A large magnetic field is required in order to bend the path of charged particles enough to allow precise measurements of their momentum. The solenoid is sufficiently large that the tracker and most of the calorimetry (both electromagnetic and hadronic) are contained inside. The muon system as well as the hadronic forward (HF) calorimeter are outside the solenoid [34].

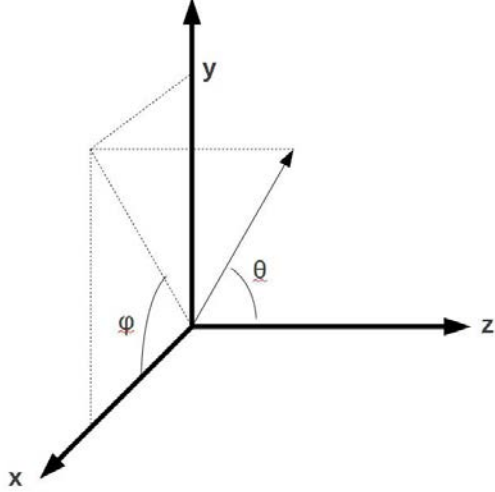


Figure 1.2: The CMS coordinate system. The z axis is along the beamline and the pseudorapidity is defined as $\eta = -\ln \tan(\theta/2)$.

CMS uses a (z, η, ϕ) coordinate system with the origin located at the interaction point. The z axis is along the beamline, η is the pseudorapidity which is related to the polar angle θ by $\eta = -\ln \tan(\theta/2)$, and ϕ is azimuthal angle. See Figure 1.2.

1.3.1 ECAL

An electromagnetic calorimeter measures the energy from particles that interact primarily by the electromagnetic force (electrons, photons, etc.). The electromagnetic calorimeter (ECAL) is composed of two parts, a barrel section (EB) and two endcaps (EE). Both EB and EE are composed of lead tungstate crystals. ECAL contains 75,848 of these crystals in all. Lead tungstate crystals were chosen both because of their short radiation and Moliere lengths (0.89 cm and 2.2 cm, respectively), and because of their speed. 80% of light is emitted from the crystals within 25 ns. Additionally, these crystals are radiation hard, allowing them to be in operation longer

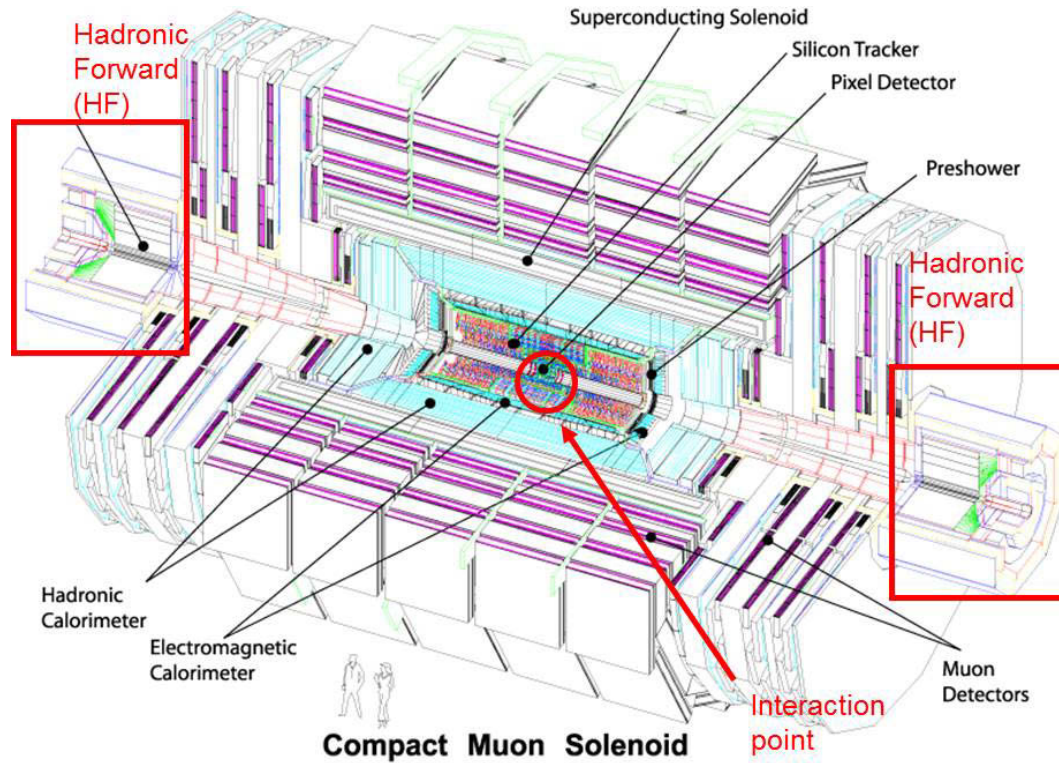


Figure 1.3: The CMS Detector.

before needing to be replaced. The tradeoff is that these crystals have a relatively low light yield, which requires photodetectors with a high gain that can operate in strong magnetic fields. Avalanche photodiodes are used in EB, and vacuum phototriodes are used in EE. EB has a pseudorapidity coverage of $0 < \eta < 1.479$. EE extends that coverage to $\eta = 3.0$ [34].

1.3.2 HCAL

A hadronic calorimeter measures the energy from particles that interact primarily through the strong force (particles containing quarks). Much of the hadronic calorimeter (HCAL) is situated between ECAL and the magnet. It is divided into four

sections: hadron barrel (HB), hadron outer (HO), hadron endcap (HE) and hadron forward (HF). The absorber material in much of HCAL is brass, as it has a short interaction length, is non-magnetic, and is easy to machine. The absorber consists of brass plates with spaces to insert plastic scintillator plates. The light from the scintillator plates is then read out of the absorber through wavelength shifting fibers. Once out of the absorber, the wavelength shifting fibers are connected to clear fibers which direct the light to a readout system of multi-channel hybrid photodiodes (HPD) [34].

The barrel calorimeter, HB, is constructed of two half barrels, and covers a pseudorapidity of $-1.4 < \eta < 1.4$. It is located inside the solenoid.

The outer calorimeter, HO, is located outside of the solenoid, and covers a pseudorapidity of $-1.26 < \eta < 1.26$. HO helps to catch hadron showers that leak through HB, extending HCAL's calorimetry to approximately 10 interaction lengths.

The endcap calorimeters, HE, are on either side of HB, and cover a pseudorapidity of $1.3 < \eta < 3.0$ and $-1.3 < \eta < -3.0$.

A more detailed description of HF will be given in the following section as Chapters 2 and 3 deal extensively with HF.

1.3.3 HF

The hadron forward (HF) calorimeter is located outside of the solenoid on opposite ends of CMS detector, with the front faces of HF located at 11.2 m from the interaction point. See Figure 1.3. HF is designed to detect particles at relatively small angles from the beamline, covering a pseudorapidity range of $2.853 < |\eta| < 5.191$

corresponding to $0.638^\circ < |\theta| < 6.60^\circ$. Note that lower values of η correspond to higher values of θ , in other words, $\eta = 2.853$ corresponds to 6.60° , *not* 0.638° .

Each forward calorimeter is a 1.65 meter long cylindrical steel absorber with quartz fibers inserted into holes in the steel, with the fibers reading out into a readout box containing photomultiplier tubes (PMTs). Each of these calorimeters is divided into 18 wedges. Figure 1.4 shows an individual wedge with the fibers and PMTs, and Figure 1.5 shows a cross sectional schematic of an HF wedge. To see how these figures correspond, note that the two rectangular arrays of circles near the front of the photograph are the two readout boxes which are located near the top left of the schematic. In the photograph, an HF wedge is shown from the back, while the schematic shows the wedge from the side.

While HF is generally associated with HCAL, it is actually both an electromagnetic and a hadronic calorimeter. To achieve this, the quartz fibers are of different lengths. Half of the fibers run the entire length of the steel absorber, while the other half start at a depth of 22 cm from the front face of the absorber. The long (L) and short (S) fibers are then read out by separate PMTs. Thus energy from electrons and photons are only seen in the long fibers, as they do not travel far enough in the steel to reach the short fibers. Hadronic particles, meanwhile, deposit energy in both long and short fibers [23].

Each HF wedge is separated into 24 towers, see Figure 1.6. Each wedge has two readout boxes of PMTs. There are two PMTs for each tower, one for the long fibers and the other for the short fibers. These readout boxes are located at approximately

$3.0 < |\eta| < 3.2$, which means that they sit directly behind towers 2, 3, 15, and 16 on each HF.

1.3.4 Other subsystems

The inner tracker system consists of a large array of silicon micro-detectors located very near the interaction point, see Figure 1.3. It can be divided into three regions. Very near the interaction point, where the particle flux is at its highest, high spatial resolution is needed. At radial distances of less than 20 cm, pixel detectors are used. One pixel is about $100 \mu\text{m} \times 150 \mu\text{m}$. As the distance from the interaction point increases, the particle flux decreases. Between 20 and 55 cm, silicon microstrip detectors are used that have a cell size of about $10 \text{ cm} \times 150 \mu\text{m}$. Beyond 55 cm, the flux is small enough to allow even larger silicon microstrips with cell sizes of about $25 \text{ cm} \times 180 \mu\text{m}$ [34].

The outside of CMS is covered by the muon detection system, as muons are the only detectable particles that penetrate the entire CMS detector. This outer muon system uses gaseous detectors to identify muons. Three different types of detectors are used. The barrel region of the muon system ($-1.2 < \eta < 1.2$) uses drift tube chambers. The endcap regions of the muon system $|\eta| \leq 2.4$ utilizes cathode strip chambers. Resistive plate chambers are used in both regions.



Figure 1.4: Photograph of HF wedge.

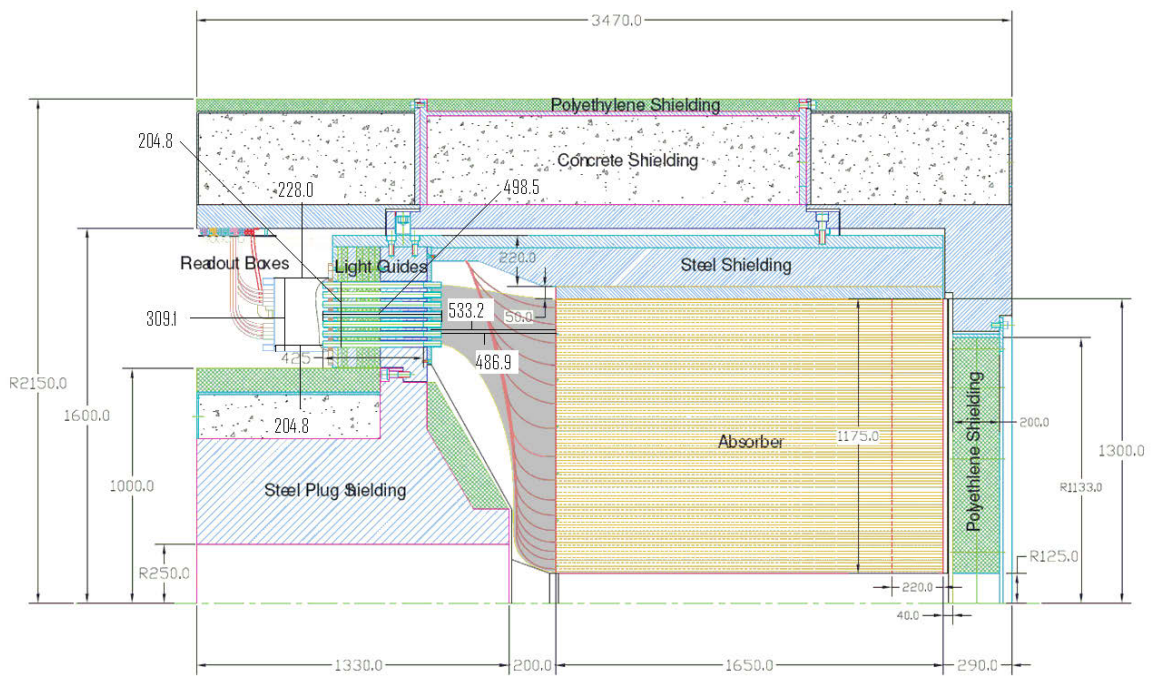


Figure 1.5: Cross sectional schematic of individual HF wedge.

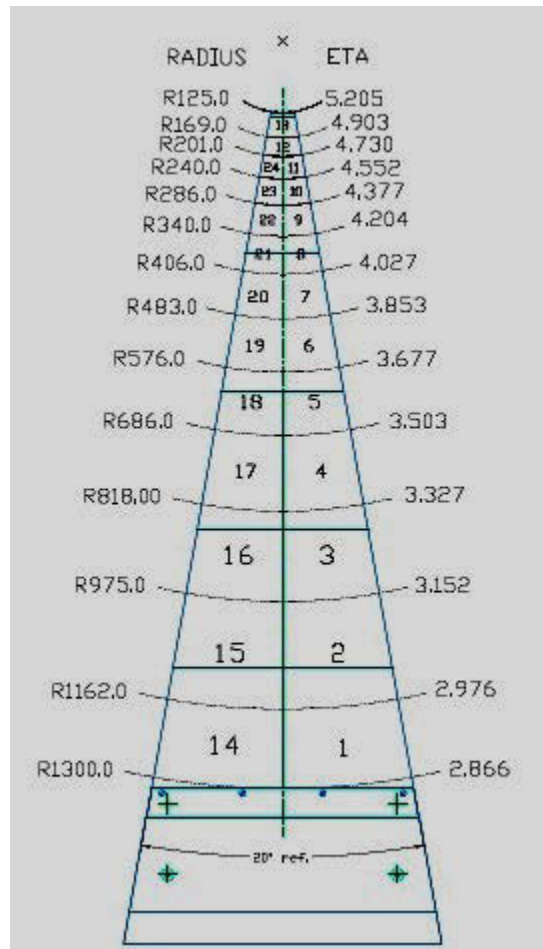


Figure 1.6: HF tower numbers and η values for an individual wedge. Each tower reads out to two PMTs with one PMT for the short fibers and another for the long fibers.

CHAPTER 2 ABNORMAL EVENTS IN HF: TESTBEAM 2004

2.1 Abnormally High Energy Events Discovered in 2004 Testbeam Data

Before being added to the CMS detector in the LHC beamline, each detector component was thoroughly tested in a controlled testbeam facility. In 2004, HF was tested at the CERN testbeam facility H2. For the remainder of this document, this HF test will be referred to as TB04. More detailed information about the testbeam setup and analysis results not directly related to this study can be found at [23].

During TB04, an HF wedge was placed in the beamline at the H2 facility where it was subject to electrons, muons, and pions of known energies up to 300 GeV. Analysis of the testbeam data revealed a number of high energy events with energies ranging from several hundred GeV up to over 1 TeV. As an energetic particle cannot deposit more energy than it has when it collides with the calorimeter, this is not a physically allowable result. Although the rate of such high energy events was small (0.17% for muons, 0.002% for electrons, and 0.16% for pions with at least 600 GeV per tower), they could still adversely affect the forward jet triggers, and they could create an artificial transverse momentum (p_T). This would cause an appearance of fake missing transverse energy (an imbalance of transverse energy), which could lead to a false indication of new physics. Therefore, since many signatures of new physics have such a transverse energy imbalance, the source of such abnormal

Table 2.1: Test beam runs used for early characterization of abnormal events. Cuts made on this data were intended to eliminate muons.

Beam	Energy(GeV)	Run No.	Before Cuts	After Cuts
e	30	22851	100,320	92965
e	50	22865	100,210	92,918
e	100	22867	100,270	91,595
e	150	22881	100,400	87,719
pi	30	22931	100,030	70,100
pi	50	22916	100,480	89,516
pi	100	22904	100,240	88,997
pi	150	22886	100,280	87,060

events must be identified and corrected.

2.2 Early Attempts to Characterize Abnormal

Events

The causes of these high energy events were initially unknown. Before the source of these events could be determined, it was necessary to make an attempt to categorize them. In these first attempts at categorization of such events from TB04, only electron and pion runs ranging from 30 to 150 GeV were studied. The testbeam runs studied are shown in Table 2.1. All testbeam data discussed here are from Wedge 2-13, with the beam incident on Tower 2. See section 1.3.3 for an explanation of the geometry of HF.

Histograms of the energy in the long and short fibers (see Section 1.3.3 for an explanation of long and short fibers in HF) were made for all events passing the muon cuts. From these histograms it was possible to visually identify obvious outlier

events in terms of energy in the long or short fibers. Scatter plots of the energy in the short fibers verses the energy in the long fibers were then made as a somewhat more informational method of visually identifying such abnormal events. With these scatter plots it is possible to tell with a glance if an abnormal event gives abnormally high energies in both long and short fibers, or if the high energy only occurs in one or the other. The histograms and scatter plots for the run numbers given in Table 2.1 are shown in Figures 2.1-2.8.

For many of the events identified as abnormal, the signal appeared outside of Tower 2. Figure 2.9 shows the channels and towers which were identified as abnormally high energy events for the 100 GeV pion run. In this figure, Tower 2 is light blue. Hits in long and short fibers are shown separately. For the purposes of this figure, an event was considered abnormal if: it occurred in Tower 2 and had an energy that exceeded three times the beam energy, or it occurred in any other tower and had an energy that exceeded the beam energy. As can be seen in the figure, all of the abnormal events occurred on the same side of the wedge (This is also true of the abnormal events from all other runs shown in Table 2.1). At the time of this study, it was thought that this was an indication that the showers from the incident particles are not fully contained by the stainless steel absorber of HF, and are in fact striking the fiber bundles leading to the PMTs.

2.3 Analysis of Abnormally High Energy

Events in HF

The results presented in this section were first reported in [28].

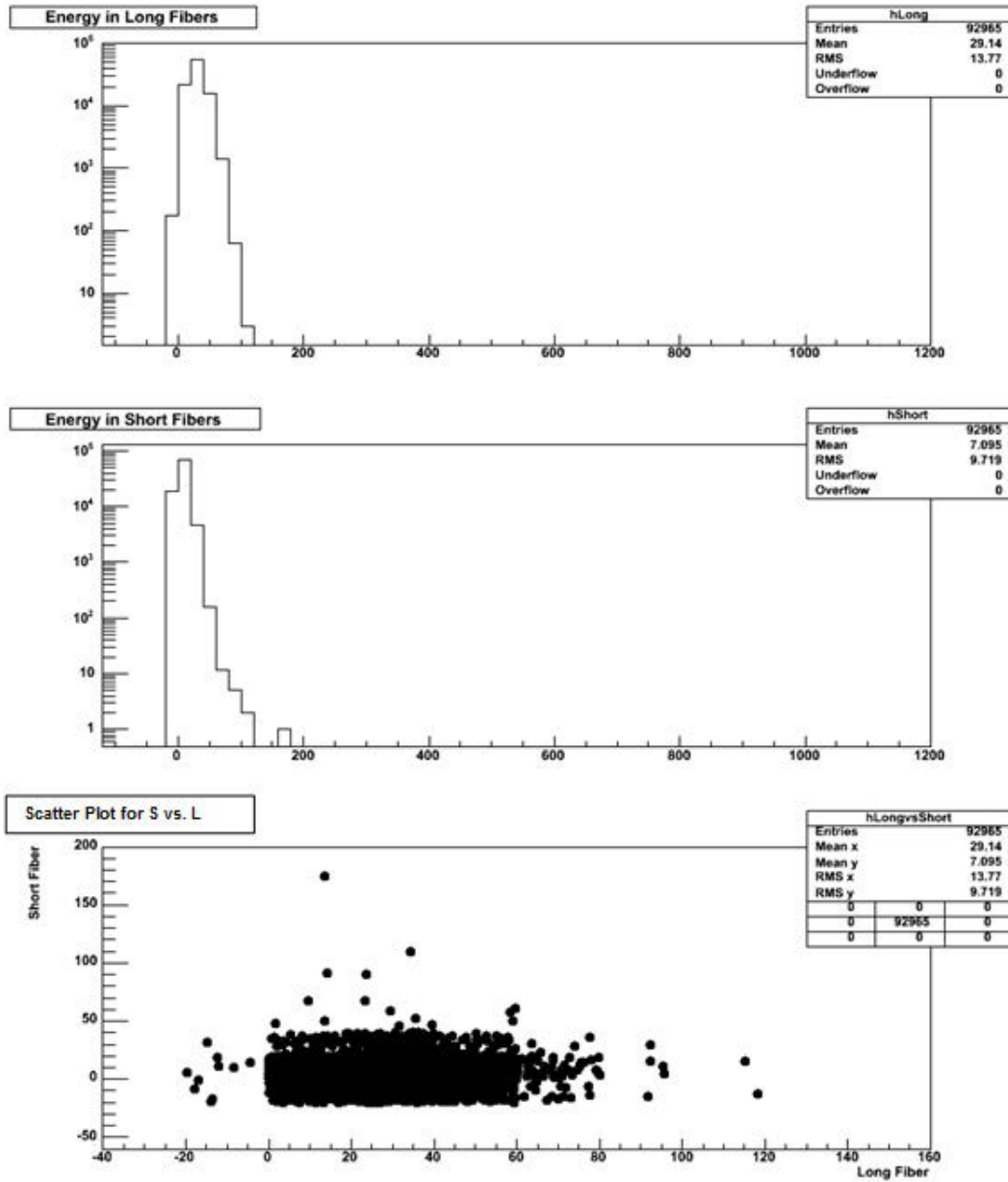


Figure 2.1: Data recorded for 30 GeV electron beams. Top: Energy in long fibers. Middle: Energy in short fibers. Bottom: Scatter plot of energy in short fibers vs. energy in short fibers.

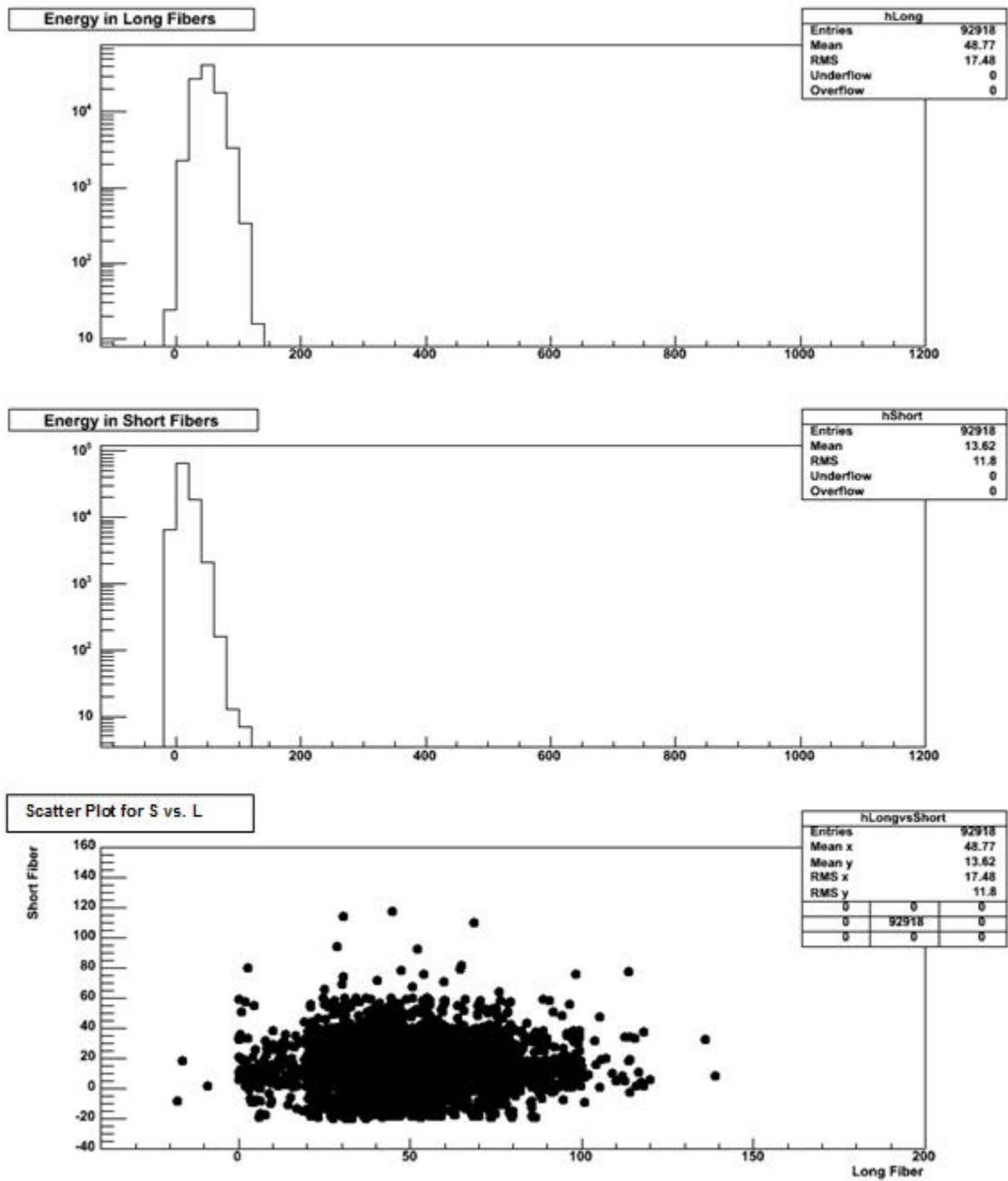


Figure 2.2: Data recorded for 50 GeV electron beams. Top: Energy in long fibers. Middle: Energy in short fibers. Bottom: Scatter plot of energy in short fibers vs. energy in short fibers.

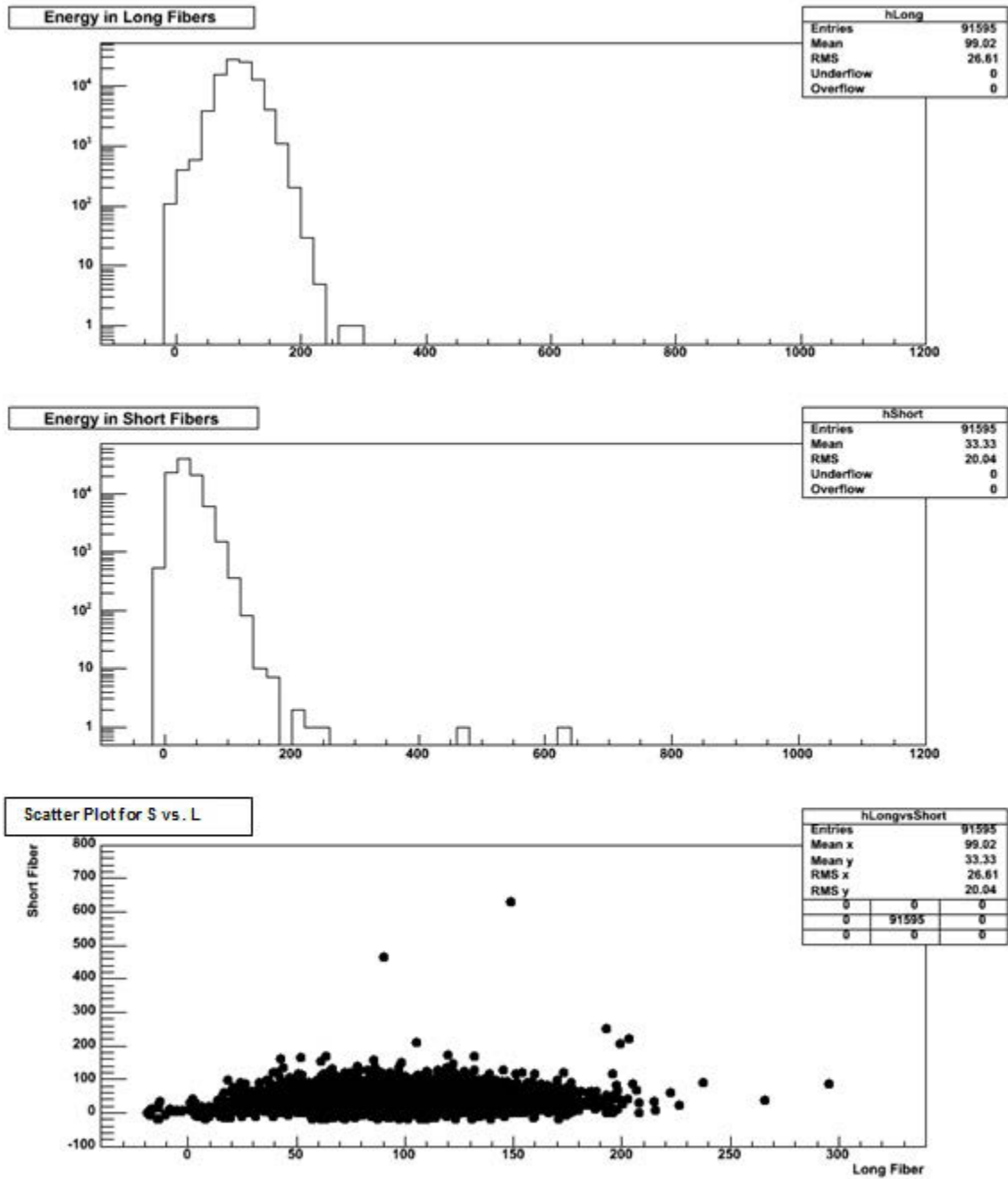


Figure 2.3: Data recorded for 100 GeV electron beams. Top: Energy in long fibers. Middle: Energy in short fibers. Bottom: Scatter plot of energy in short fibers vs. energy in long fibers.

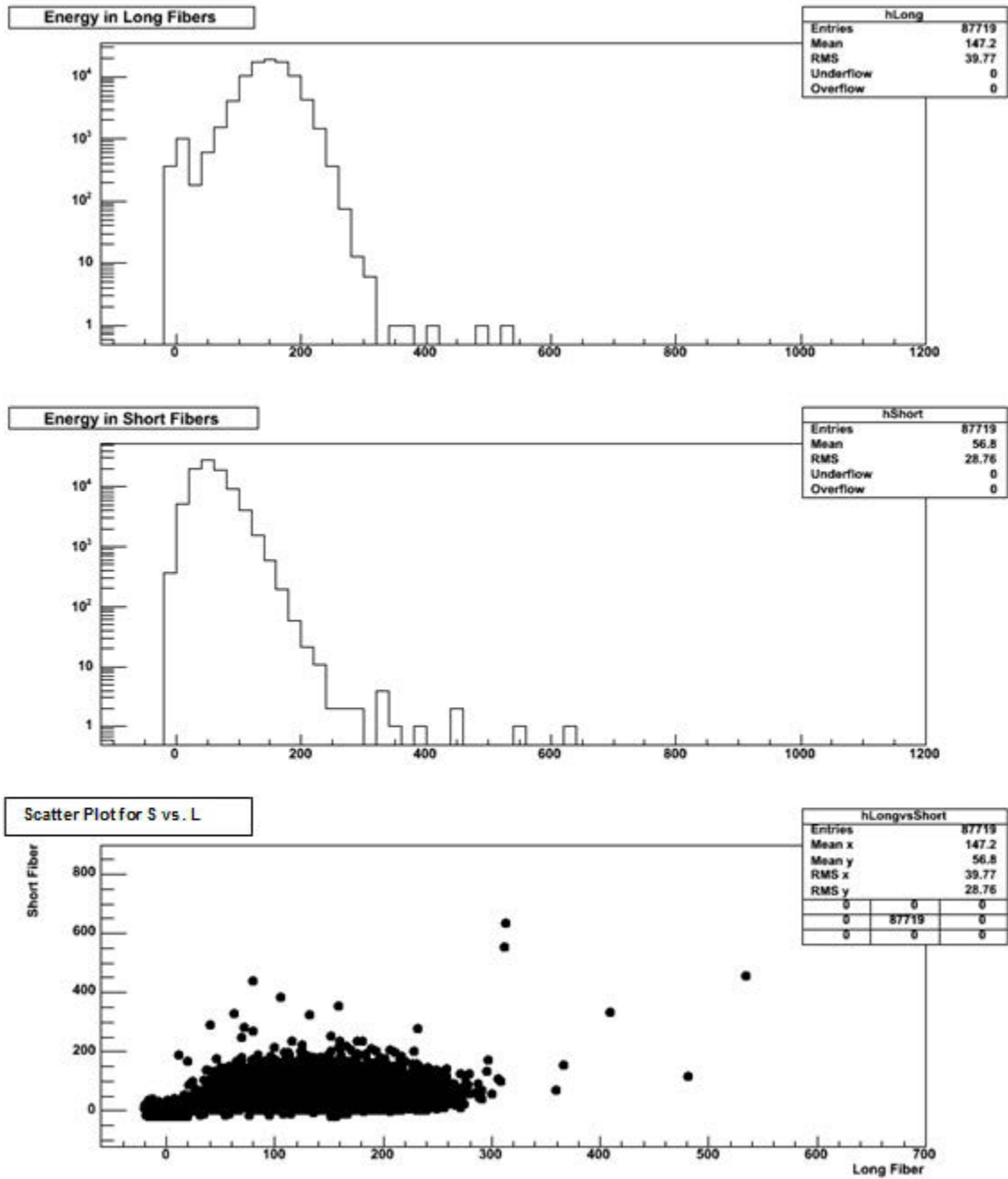


Figure 2.4: Data recorded for 150 GeV electron beams. Top: Energy in long fibers. Middle: Energy in short fibers. Bottom: Scatter plot of energy in short fibers vs. energy in short fibers.

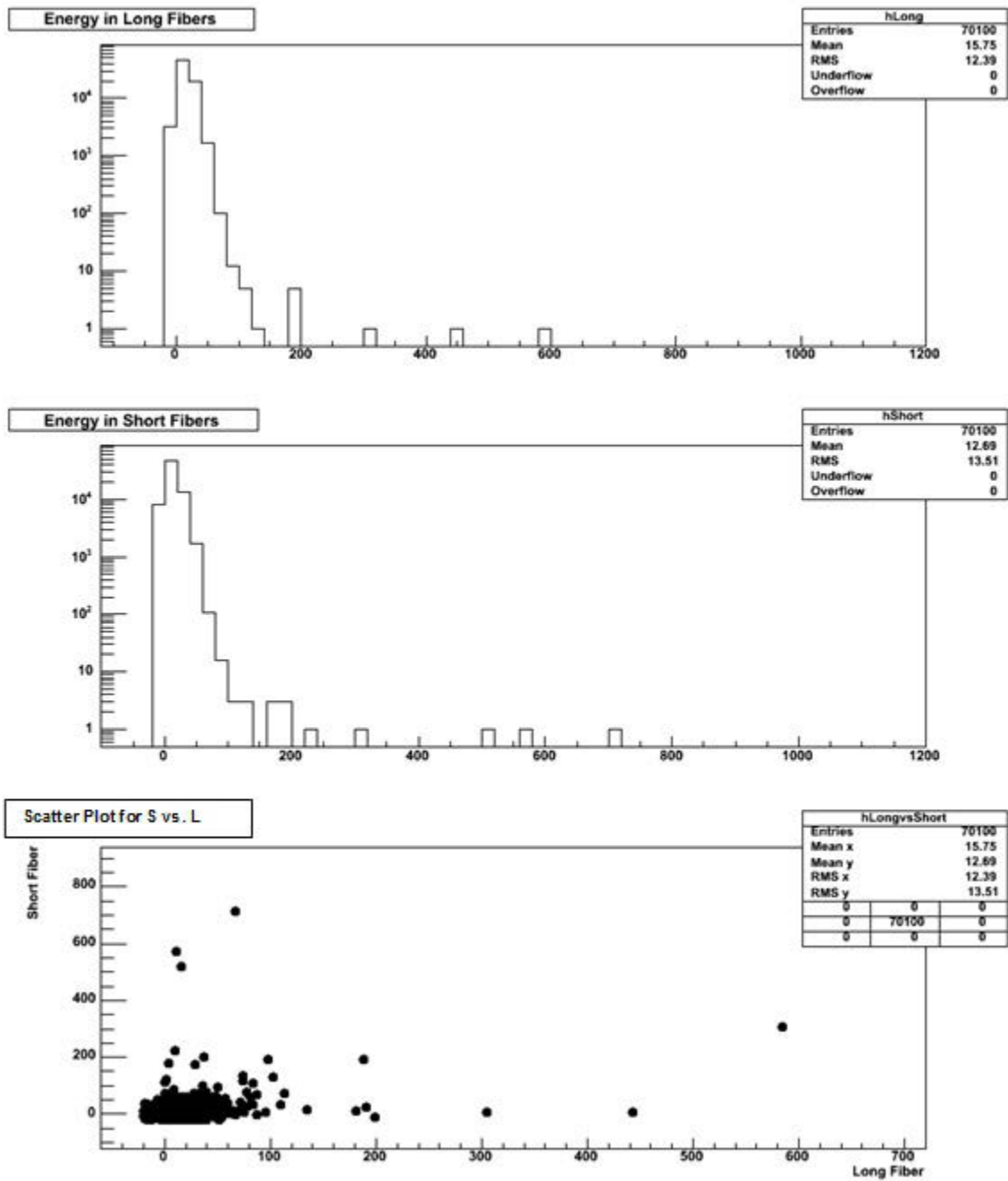


Figure 2.5: Data recorded for 30 GeV pion beams. Top: Energy in long fibers. Middle: Energy in short fibers. Bottom: Scatter plot of energy in short fibers vs. energy in short fibers.

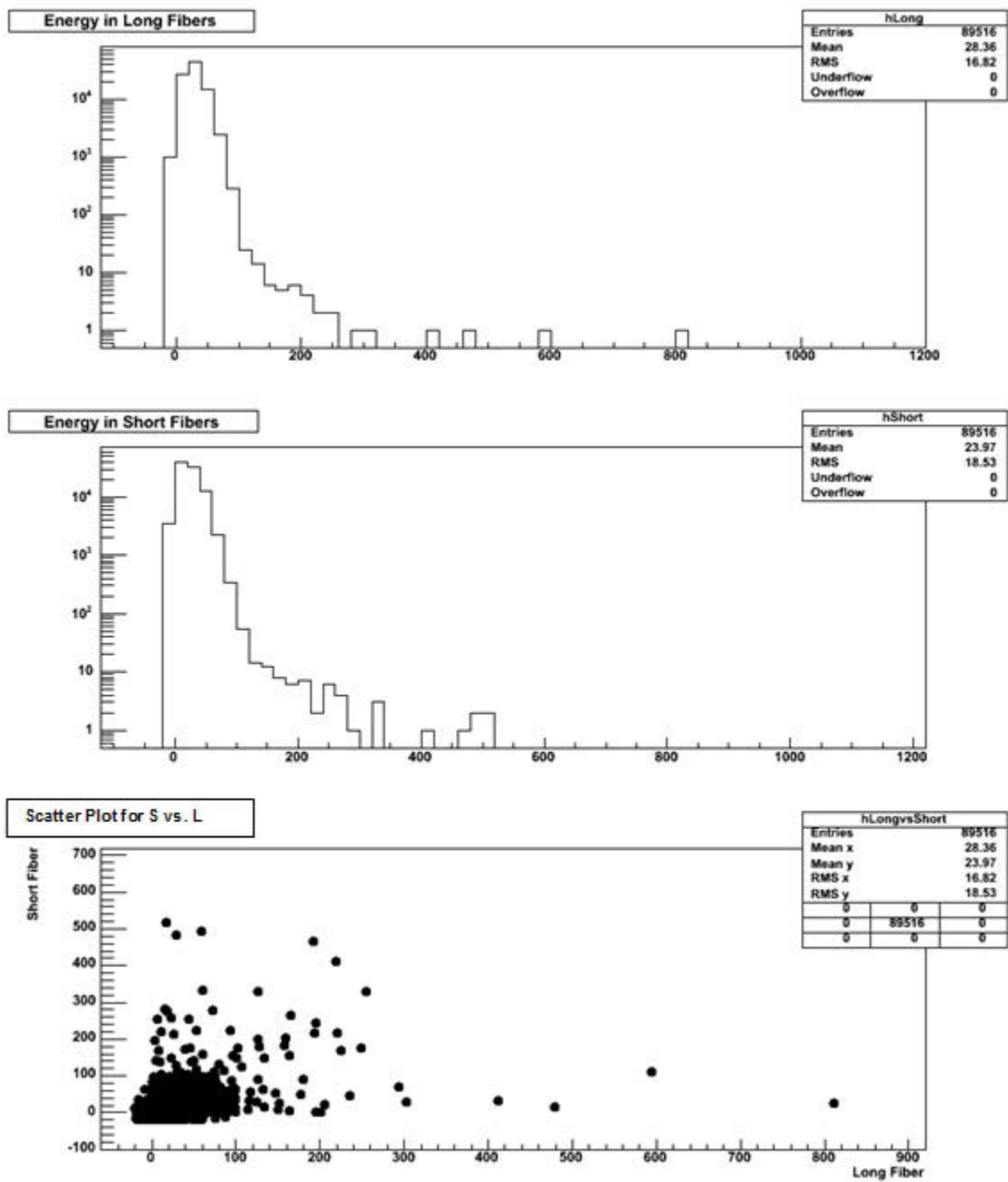


Figure 2.6: Data recorded for 50 GeV pion beams. Top: Energy in long fibers. Middle: Energy in short fibers. Bottom: Scatter plot of energy in short fibers vs. energy in short fibers.

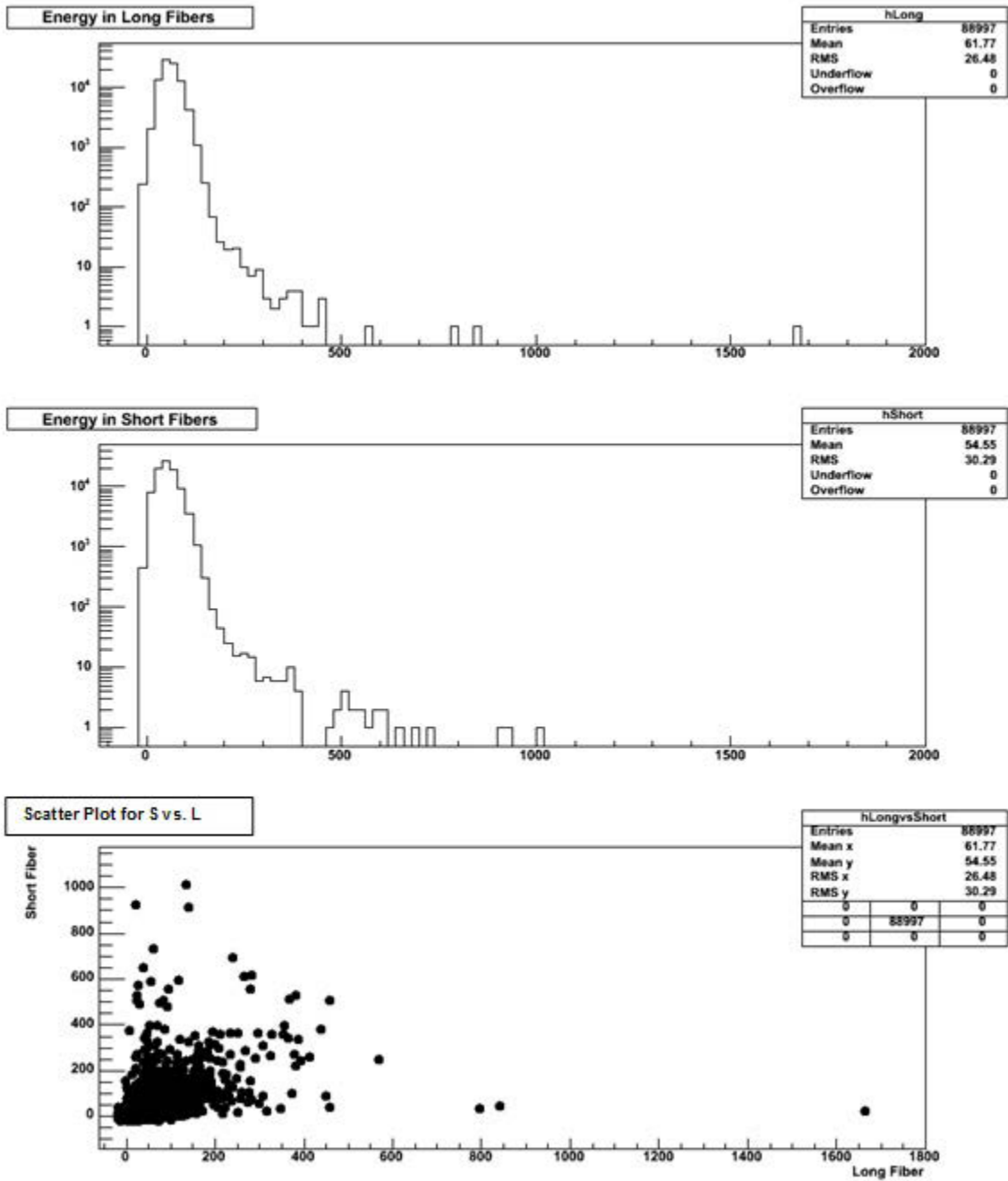


Figure 2.7: Data recorded for 100 GeV pion beams. Top: Energy in long fibers. Middle: Energy in short fibers. Bottom: Scatter plot of energy in short fibers vs. energy in short fibers.

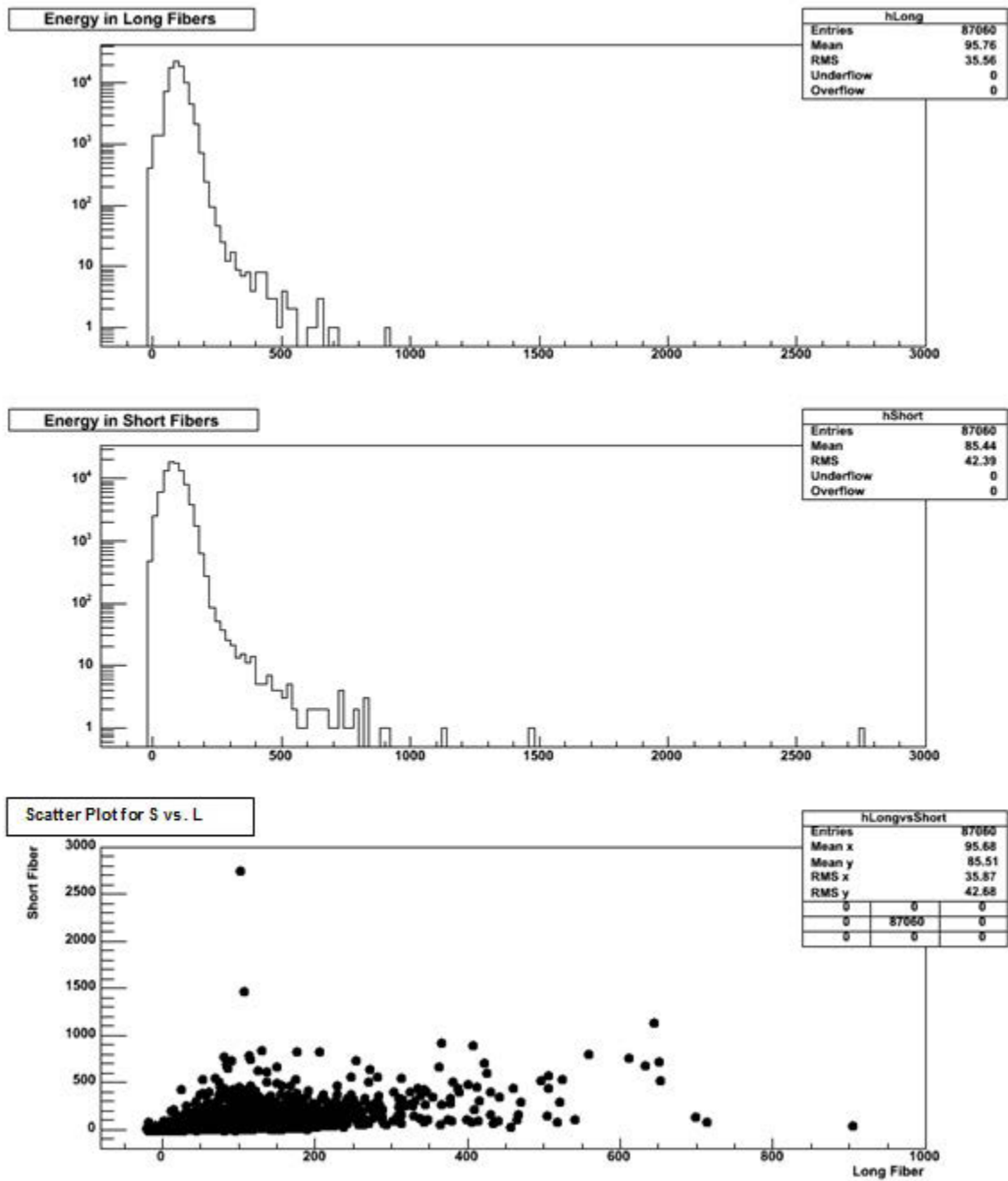


Figure 2.8: Data recorded for 150 GeV pion beams. Top: Energy in long fibers. Middle: Energy in short fibers. Bottom: Scatter plot of energy in short fibers vs. energy in short fibers.

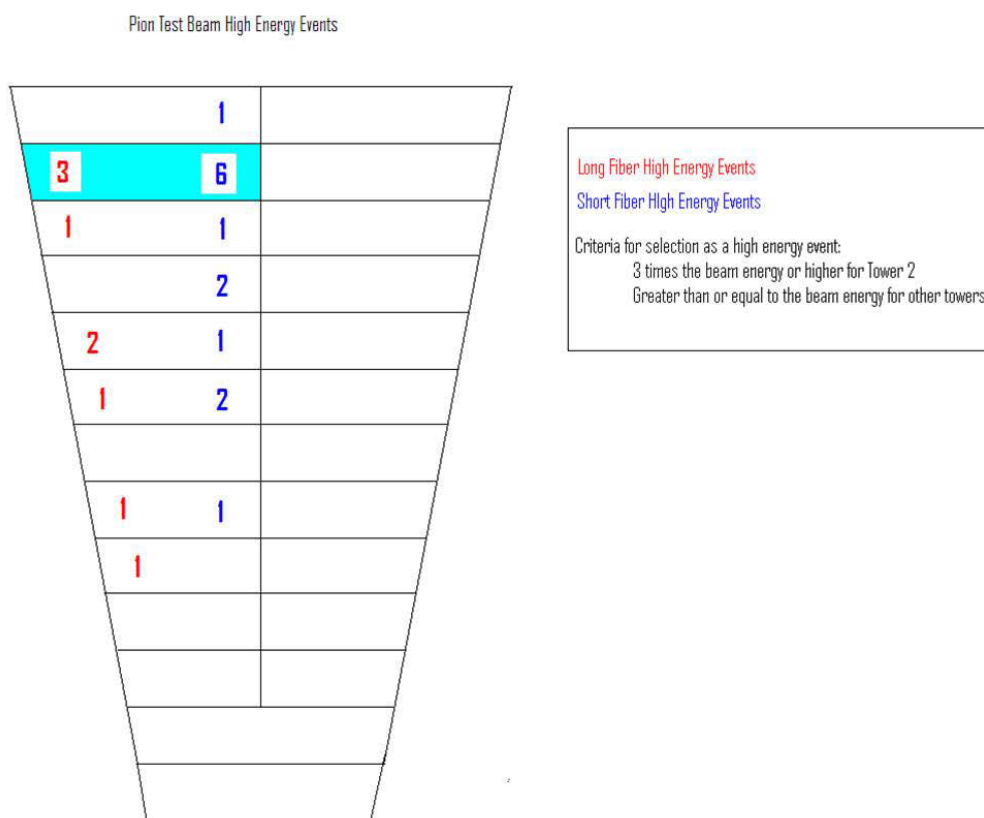


Figure 2.9: Channels with abnormal events for 100 GeV pions. The numbers indicate the number of abnormal events in each tower for long and short fibers.

2.3.1 Origin of Abnormally High Energy Events

It was later determined that the abnormal events were not caused by late showers striking the fiber bundles that lead to the PMTs, but rather by the showers striking the PMT windows directly. A more detailed description follows below.

In the HF calorimeter the signal from the fibers is produced when Cerenkov photons from traversing relativistic particles are captured inside the fiber due to the numerical aperture ($\text{N.A.} = \sqrt{n_{\text{core}}^2 - n_{\text{clad}}^2}$) between the fiber core and cladding (which gives a 71° critical angle)[24]. Since the detector works using the collection of Cerenkov photons, HF is mostly sensitive to electromagnetic (e.m.) showers. Hadronic showers have an e.m. shower core due to π^0 production and subsequent decay to photons in hadronic interactions, and therefore the lateral and longitudinal size of the e.m. component is determined by the fluctuation of π^0 production. Since the e.m. core of the hadronic showers is absorbed by the fibers, the hadronic showers are relatively short and narrow in HF compared to the other hadronic calorimeters[25]. However, the production of π^0 fluctuates throughout shower development, and late production of π^0 s may occur. The passive material in HF, which is stainless steel, is 165 cm long ($\sim 10\lambda_I$) and provides 95% containment of the longitudinal shower profiles for hadrons. The e.m. components of hadronic showers, however, may not be confined in this depth due to late production of π^0 s. The small e.m. showers from π^0 decays may strike the photomultipliers (PMT), contributing to the signal. Another source are muons, since they traverse all of HF without losing much of their energy. Direct hits to PMTs give rise to detected signal.

The PMTs which are used in HF are Hamamatsu R7525[27]. They have a plano-convex glass face, 1 mm thick in the center expanding to 6.1 mm at the outer radius of the window as shown in Fig. 2.10. The PMT window is a source of Cerenkov photons which will yield fake energy deposition signals in HF. An estimate of the size of the effect follows from[26]:

$$\frac{d^2N}{dE dx} \approx 370 \sin^2 \theta_c \quad eV^{-1} cm^{-1}$$

where $\theta_c = \cos^{-1}(1/\sqrt{n\beta})$, and n is the refractive index of the glass. Using 1.5 for the index of the glass, a fast particle traversing the thickest part of the window makes 124 Cerenkov photons in an energy range of 1 eV. Taking the quantum efficiency of the photocathode to be 25%, and using the test beam conversion factor of 0.25 photoelectrons per GeV, we expect that a single fast charged particle will appear to deposit ~ 124 GeV when traversing the thickest part of the PMT window. Indeed, this effect is observed. Muons in the beam test can be used to demonstrate this effect since they behave like minimum ionizing particles. The energy depositions from muons inside HF are expected from δ -electrons, minimum ionization and bremsstrahlung processes resulting in a few GeV signal[25]; therefore large energy readouts are due to the interaction with the PMT glass. Figure 2.11[23] shows the transverse spatial distribution of events with large energy deposits for HF illuminated by muons[24]. Note that the highest probability density occurs on the periphery of the PMT window, as expected. Note also that the energy deposited by such events is entirely consistent with the estimated energy deposit made by the Cerenkov light production mechanism. Therefore, the effect is well understood and that understanding

allows us to explore ways of mitigating the effect.



Figure 2.10: A picture of the HF PMT glass section. The glass shape is plano-convex and the thickness in the center (1 mm) increases towards the edges (6.1 mm). Interaction of relativistic particles with glass create Cerenkov photons.

2.3.2 Dataset

The beam types used in this study were electrons, charged pions, and muons. After the run numbers were decided, several event selection criteria were applied. First, beam events were chosen from the data stream (there are LED, laser or pedestal events in a run file). Then a phase requirement was applied ($140 \text{ TDC counts} < \text{Phase} < 180 \text{ TDC counts}$). The phase was calculated as the time difference between the timing reported from the TTC (short for Trigger Timing and Control, which provides transmission of the L1 accept decision) unit and from the beam coincidence hit from scintillating beam triggers at H2. Then the five wire chambers were used to select

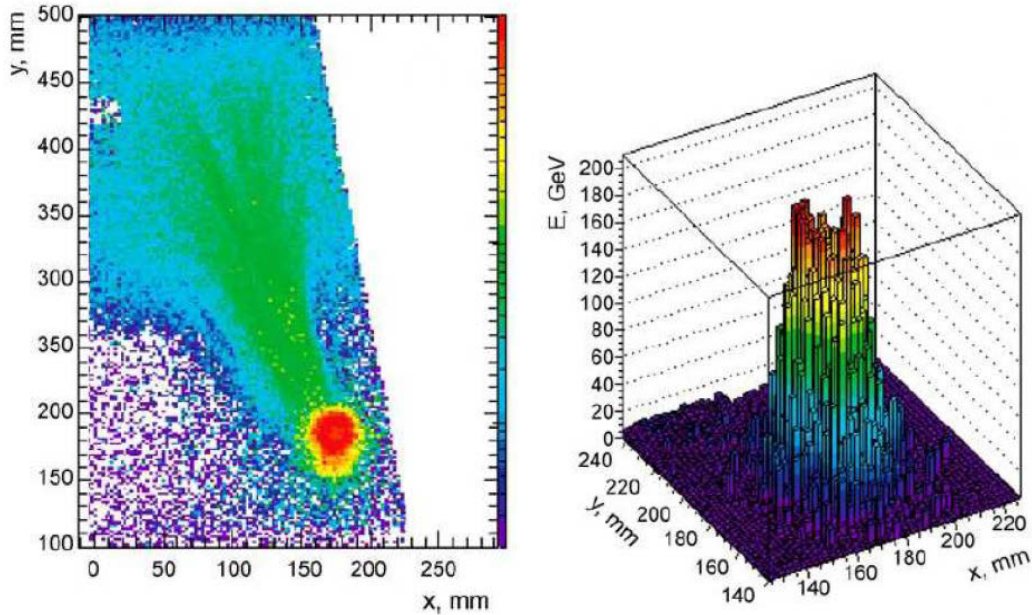


Figure 2.11: Muons produce a large signal when they hit the PMT glass. The location and periphery of the PMT window can be seen clearly by a 150 GeV muon beam (left). The energy measured from PMT events is on the order of 100 GeV as expected (right).

a rather broad incident area in terms of the x and y position ($|x, y| < 60$ mm). In order to avoid reducing the number of events significantly, a single hit condition in the wire chambers was applied only on the first chamber (elimination of events which had beam line interactions require tighter cuts on all wire chambers). Muon contamination in the electron and pion beam was cleaned by using the muon veto counter.

For the pion and electron runs, the beam was incident on tower two, and the HF table positions for both x and y were close to the center of the tower. For muons, the beam was incident on tower fourteen. Towers two and fourteen are both positioned in front of the readout boxes (See section 1.3.3). Therefore they provide

Table 2.2: Beam type, energy, and run numbers used for $\frac{S}{L+S}$ analysis.

Beam Type	Energy	Run Numbers
Pions	300 GeV	20566, 20579, 17457
Pions	100 GeV	19977-19979, 19998-2000, 20580, 20591
Muons	150 GeV	20441-20452, 20481-20492, 20521-20532, 20548-20557
Electrons	100 GeV	14884-14923
Electrons	50 GeV	22447, 22865, 16916, 16919

useful information for studying abnormal events. In addition, this selection also reduces the effect of shower leakage for pions. The runs that satisfy these requirements were selected based on the HF table position and beam type/energy information recorded in the run database. 300 and 100 GeV pion runs, 150 GeV muon runs, and 100 and 50 GeV electron runs were selected as indicated in Table 2.2.

The detector response was calibrated and converted to GeV by using 100 GeV electrons at tower number two.

From this point on in all discussions of the L and S analysis, all pion and electron signals roughly corresponding to more than 600 GeV will be referred to as abnormal events. Similarly, muon signals of more than 100 GeV will be referred to as abnormal. While events with signals corresponding to energies below these thresholds will be referred to as normal in this study, it should be noted that these thresholds are quite arbitrary, as the values were chosen to be large enough that all events selected as abnormal are truly abnormal events.

2.3.3 Energy in Long and Short Fibers

A key difference between these high energy PMT events and more normal events is localization. Since the HF readout box is designed to have two PMTs for each tower to read long and short fibers separately, we don't expect to see correlation between these two PMTs for high energy events. Therefore a comparison of the signal from the long fibers with that from the short ones can be used to help characterize high energy events.

For each beam type (particle and energy) in the energy study, the events were categorized as normal or abnormal based on the criteria given in the previous section. The ratio $\frac{S}{L+S}$ was determined for all 48 channels in the HF wedge. High values of this ratio would indicate that the short fibers received much more energy than the long fibers, which could be an indication that particles were directly striking the window of PMTs for short fibers, as the energy from late showering particles in HF should be approximately equal in the long and short fibers. Low values of the ratio $\frac{S}{L+S}$, on the other hand, could indicate two different situations. This ratio could be low due to particles directly striking the window of PMTs for long fibers, or it could be low due to early showering particles, such as electrons, depositing the majority of their energy before the short fibers begin.

The ratio $\frac{S}{L+S}$ was then plotted for normal and abnormal events of each particle and energy (if abnormal events were present for that particle and energy), to see if there was a significant difference in the ratio for normal and abnormal events. The mean value of the ratio for normal events was then used to make a cut on both normal

and abnormal events. Plots were produced for both normal and abnormal events for events cut verses Δ cut, where Δ cut was the distance from the mean of $\frac{S}{L+S}$ for normal events of that particle and energy. All events with a value of $\frac{S}{L+S}$ more than Δ cut away from the mean for normal particles were rejected. With the appropriate choice of Δ cut, it is hoped that the majority of normal events can be accepted, and the majority of abnormal events rejected.

Figures 2.12-2.29 show the ratio $\frac{S}{L+S}$ for abnormal and normal events of each particle and energy shown in Table 2.2, as well the corresponding plots of events cut verses Δ cut.

For 300 GeV pions, the results for normal and abnormal pions are quite distinct. Figure 2.12 shows that the mean value of $\frac{S}{L+S}$ for normal 300 GeV pions is 0.413, with very few events having extremely high or low values. The corresponding histogram for abnormal 300 GeV pions is shown in Figure 2.14. In contrast with normal events, there are very few events close to the mean, with large peaks near 0 and 1, meaning that it is likely that particles are directly striking the PMT windows. Looking at the corresponding plots of events cut verses Δ cut (Figures 2.13 and 2.15), choosing a Δ cut of 0.2 only cuts $\sim 5\%$ of normal events, and cuts $\sim 80\%$ of abnormal events. The results for 100 GeV pions, as shown in Figures 2.18 - 2.19), are quite similar to those for 300 GeV pions, although the peak of the $\frac{S}{L+S}$ histogram for normal events appears to be somewhat broader.

For 150 GeV muons, from Figure 2.20, it is likely that the “abnormal” threshold could be set at a lower energy. But for the muons that were selected as abnormal,

as shown in Figure 2.22, the $\frac{S}{L+S}$ histogram consists primarily of two sharp peaks at 0 and 1. With the muons, even a Δ cut as high as 0.4 eliminates $\sim 90\%$ (or more) of these events.

As somewhat expected, 50 GeV electrons have no abnormal events, Figures 2.24 and 2.25 show $\frac{S}{L+S}$ and events cut verses Δ cut for normal 50 GeV electrons, with a mean $\frac{S}{L+S}$ of 0.1238. Figure 2.26 and 2.27 show $\frac{S}{L+S}$ and events cut verses Δ cut for normal 100 GeV electrons, which have a mean of 0.1986. As shown in Figure 2.28, there were only 6 abnormal events for 100 GeV electrons, making any statistics of these events quite irrelevant.

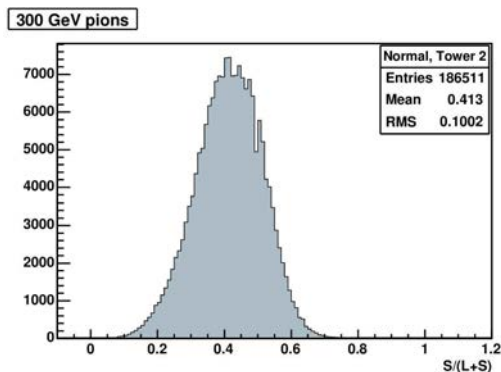


Figure 2.12: Normal 300 GeV pions, $\frac{S}{L+S}$.

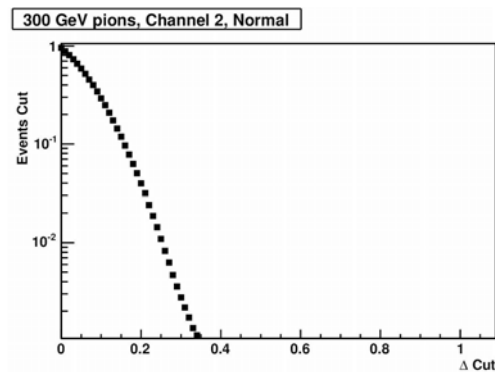


Figure 2.13: Fraction of events cut when all events outside of Δ Cut from the mean of the plot to the left are rejected.

The values of $\frac{S}{L+S}$ are significantly different for normal and abnormal events, and the sharp peaks at 0 and 1 for abnormal pions and muons are a good indication

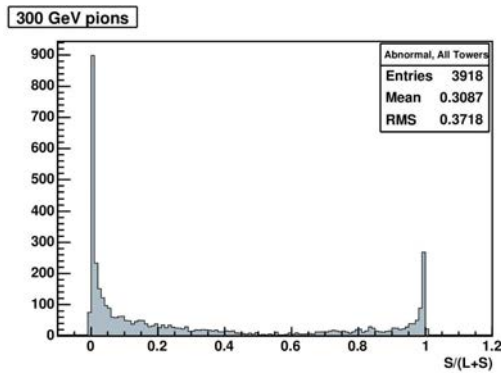


Figure 2.14: Abnormal 300 GeV pions, all channels, $\frac{S}{L+S}$.

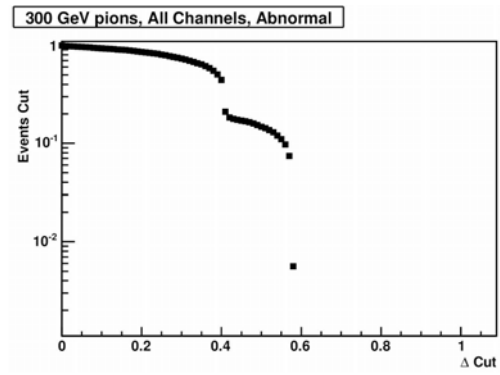


Figure 2.15: Fraction of events cut when all events outside of Δ Cut from the mean of $\frac{S}{L+S}$ for normal 300 GeV pions are rejected.

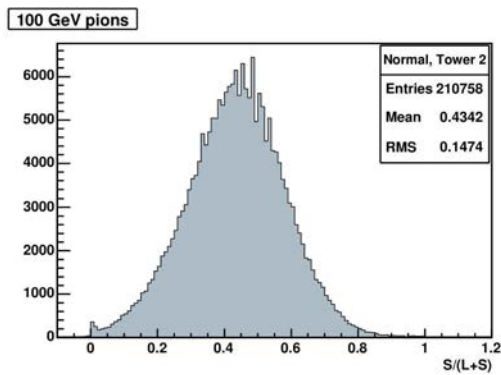


Figure 2.16: Normal 100 GeV pions, $\frac{S}{L+S}$.

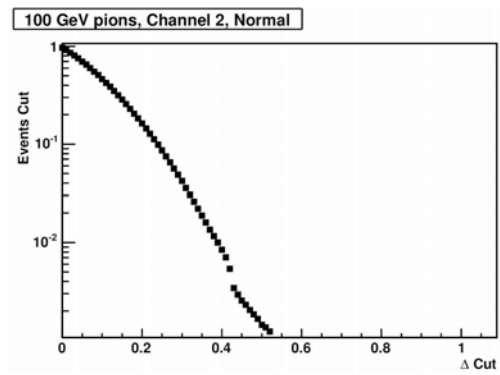


Figure 2.17: Fraction of events cut when all events outside of Δ Cut from the mean of the plot to the left are rejected.

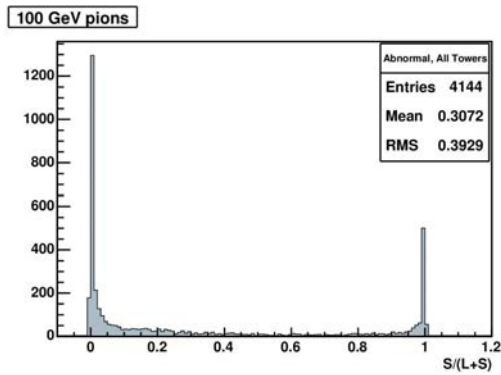


Figure 2.18: Abnormal 100 GeV pions, all channels, $\frac{S}{L+S}$.

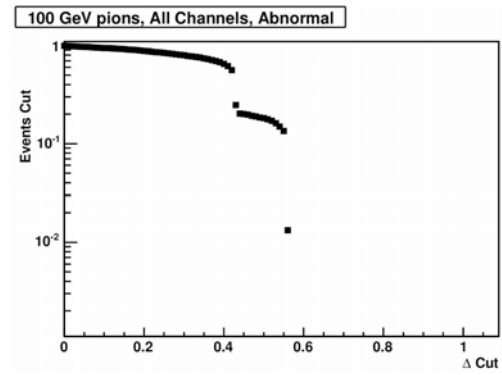


Figure 2.19: Fraction of events cut when all events outside of Δ Cut from the mean of $\frac{S}{L+S}$ for normal 100 GeV pions are rejected.

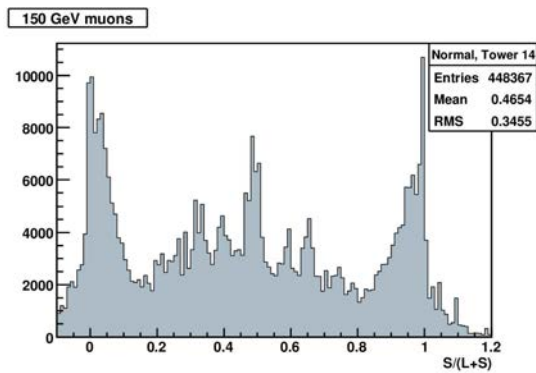


Figure 2.20: Normal 150 GeV muons, $\frac{S}{L+S}$.

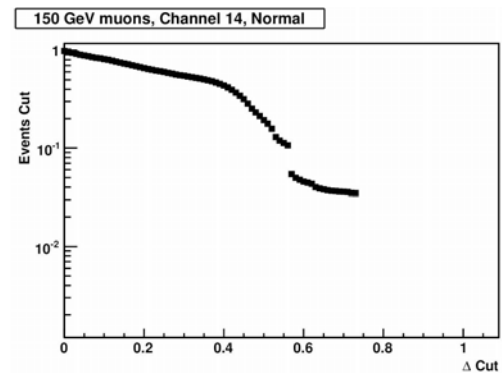


Figure 2.21: Fraction of events cut when all events outside of Δ Cut from the mean of the plot to the left are rejected.

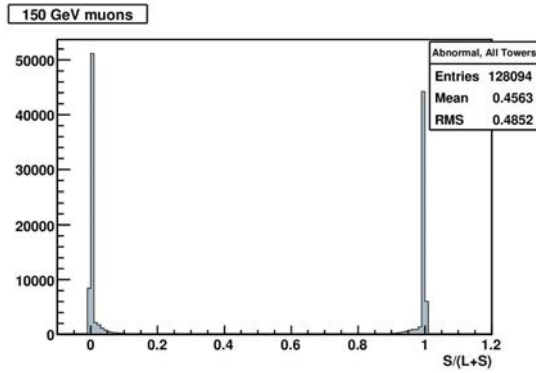


Figure 2.22: Abnormal 150 GeV muons, all channels, $\frac{S}{L+S}$.

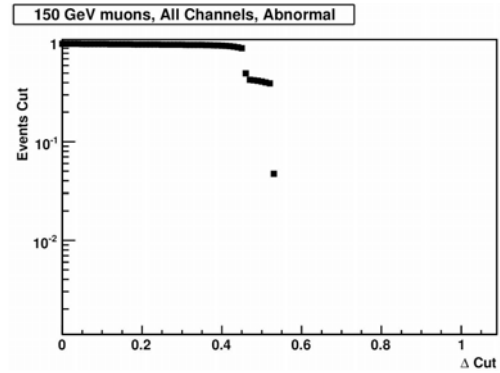


Figure 2.23: Fraction of events cut when all events outside of Δ Cut from the mean of $\frac{S}{L+S}$ for normal 150 GeV muons are rejected.

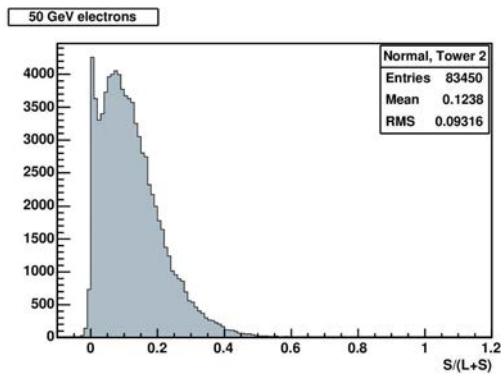


Figure 2.24: Normal 50 GeV electrons, $\frac{S}{L+S}$. (There are no abnormal events for 50 GeV electrons.)

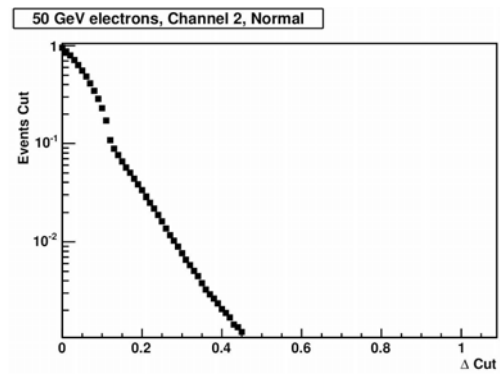


Figure 2.25: Fraction of events cut when all events outside of Δ Cut from the mean of the plot to the left are rejected.

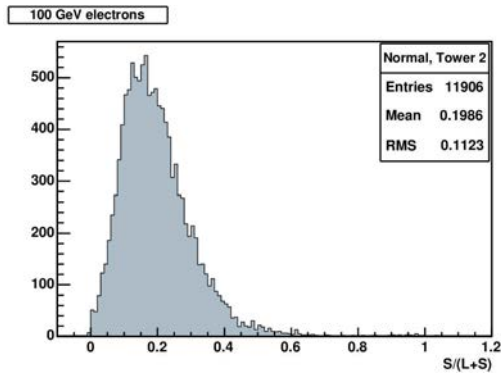


Figure 2.26: Normal 100 GeV electrons, $\frac{S}{L+S}$.

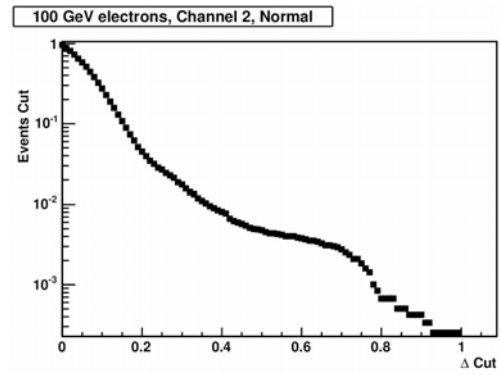


Figure 2.27: Fraction of events cut when all events outside of Δ Cut from the mean of the plot to the left are rejected.

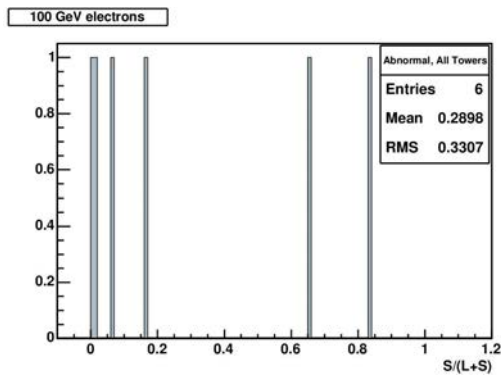


Figure 2.28: Abnormal 100 GeV electrons, all channels, $\frac{S}{L+S}$.

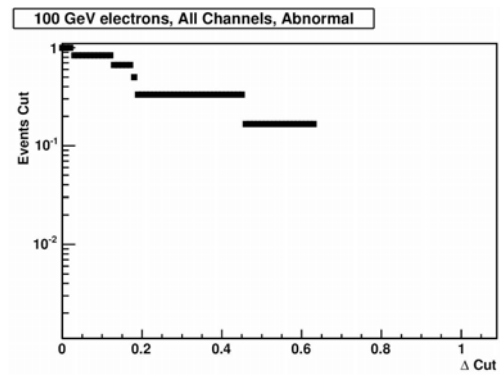


Figure 2.29: Fraction of events cut when all events outside of Δ Cut from the mean of $\frac{S}{L+S}$ for normal 100 GeV electrons are rejected.

that many of these abnormal events are particles directly striking the PMT window. While using this ratio to determine cuts is somewhat efficient when the incoming particle is known, it may not be practical to use if particles have yet to be identified. Different particles have different characteristic values of $\frac{S}{L+S}$. For example, if we said that a reasonable starting point was an $\frac{S}{L+S}$ was 0.45, and chose a Δ cut of 0.2, then the majority of normal electrons would be cut. While it is likely that a high value of $\frac{S}{L+S}$ indicates an abnormal event, if the total energy deposited is not taken into account, a low value of $\frac{S}{L+S}$ could indicate an abnormal event, or it could be an electron.

In summary, $\frac{S}{L+S}$ can be a useful indicator for tagging abnormal events, but to be a truly effective means of eliminating such events, it would need to be used along with some other indicator (One such indicator could be timing, which will be discussed in the simulation study of Chapter 3), otherwise it has a high likelihood of eliminating early showering particles such as electrons.

CHAPTER 3 HF PMT SIMULATION

3.1 Modifications to original GEANT4

Simulation of HF for Studying Abnormal Events

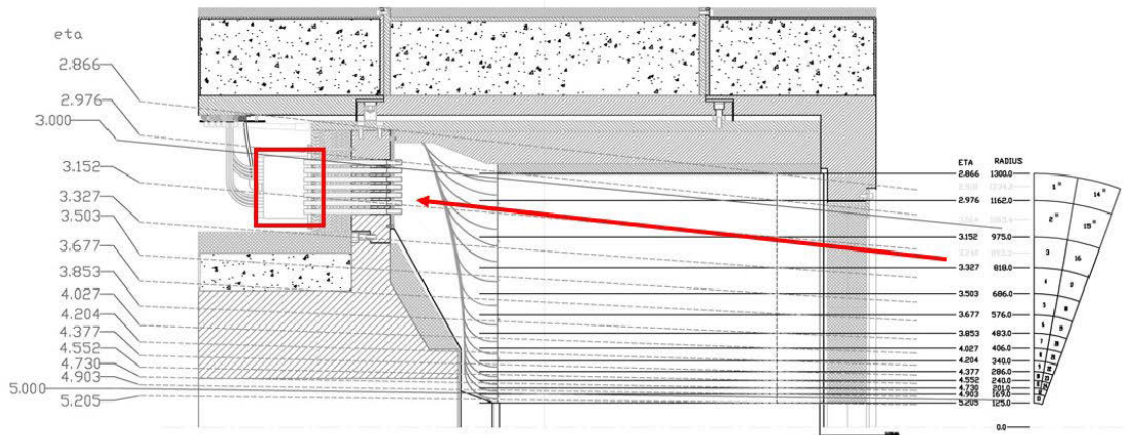


Figure 3.1: Diagram of HF. The readout box (indicated by the red box) is located at $3 \leq |\eta| \leq 3.2$. The red arrow represents particles passing through HF coming from the direction of the interaction point.

To further study and verify the abnormally high energy events discussed in the previous chapter, the exiting full simulation using CMSSW and Geant4 was modified. The PMT windows were added as separate sensitive detectors behind HF to account for the PMT readout box assembly sitting behind the calorimeter at roughly $3 \leq |\eta| \leq 3.2$, see Figure 3.1. For more on HF, see Section 1.3.3 and reference [34]. The PMT

windows are currently incorporated as disks of uniform thickness (6 mm), although the windows of the PMTs currently installed on HF are plano-convex. Additionally these disks are divided into two groups to account for the PMTs that read out the long fibers and for those that read out the short fibers. See Figure 3.2. The current window is 6 mm thick at the edges, but is much thinner in the center. Any differences in window thickness will have an impact in the distribution of Cerenkov photons produced in the windows, whether it be the difference between the real PMTs and the simulation, or with the replacement PMTs that will be installed for future LHC runs [33].

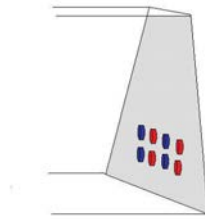


Figure 3.2: A conceptual diagram showing the disks which simulate the PMT windows in the modified HF simulation.

The standard HF simulation utilizes shower libraries for hadronic as well as electromagnetic showers. In this approach any hadron, electron, positron or photon entering the forward calorimeter is removed and replaced by a number of photoelectrons (1 p.e. corresponds to about 4 GeV) which are obtained from a pre-generated shower kept in a library. This approach needs to be modified to take care of shower

leakage in case of hadronic showers. The new approach for a parameterization of showers in HF continues to utilize the shower library for electrons, positrons, and photons. Hadrons are treated differently. The hadrons themselves are transported using Geant4, while the electromagnetic component of the hadronic showers are either transported using Geant4 or are replaced using the shower library depending on their longitudinal position within HF [29], [30].

Before discussing the simulation results, a brief description of the simulation chain and a few definitions will be helpful to the reader.

The first step in the simulation is to use a generator (such as Pythia) to produce simulated particles. The output could be as basic as a single electron, or it could be numerous particles from a proton-proton collision, but the key point here is that it is just the particles themselves. At this point there is no detector information in the data. An electron from the particle generator is just an electron with its mass, charge, energy, etc. It has not yet interacted with any detector, and at this stage could be injected into a simulation of *any* detector, whether it be CMS, a different LHC detector, or a future detector that has not been physically constructed. Particles at this stage are referred to as generator level objects, and often have the "Gen" prefix attached (GenMET, GenJets, etc.).

After the particles have been generated, they interact with the detector components. The interaction of the particles with the material of a sensitive detector is stored as a simulated hit. No detector noise is added at this stage, and the various detector electronics are not accounted for at this stage. A hit is the energy deposited

in a single cell for an individual event. For example, if a pion is incident on a detector which is geometrically divided into multiple cells. As the pion showers, let's say it deposits energy into four different cells. There would then be four hits for that one event. The pcalohits discussed later in this chapter are one such variety of simulated hit.

Reconstructed level objects take the simulated hits and add in the various effects of the detector in order to simulated the results that would be obtained from the real, physical detector (noise, electronics limitations, etc.). These reconstructed level objects often have the "Rec" prefix attached (RecMET, RecJets, etc.).

The term jet will be referred to many times throughout the rest of this work. A jet is the resulting cone of particles produced from the hadronization of a quark or gluon. A GenJet exactly contains all of the particles and the energy from this hadronization, as it keeps track of all of the showering particles. A RecJet, on the other hand, is an attempted reconstruction of the jet (whether a simulation or from actual collision data). The energy of the resulting ReJet will depend on the particular jet reconstruction algorithm and cone size used.

3.2 Simulation of PMT Hits for Single Particles and Pythia Jets

The results presented in this section were originally reported in [30].

3.2.1 Datasets

The Monte Carlo datasets used in this study were generated using CMSSW_3.2.4. Datasets of 100,000 particles each were generated for 100 GeV electrons, 150 GeV muons, and 100 GeV pions using a particle gun. A dataset of 100,000 jets at 50 GeV p_T was generated using a particle gun like interface for Pythia. The pseudorapidity range for all datasets was $3 \leq |\eta| \leq 3.3$, which roughly corresponds to the position of the readout box behind HF containing the PMTs.

3.2.2 Long and Short Fiber Energies

The energies in the long fibers (depth 1) and the energies in the short fibers (depth 2) for both 100 GeV pions and 100 GeV electrons are shown in Figures 3.3 and 3.4. The energies in general seem somewhat low. For 100 GeV Pions, the ratio of the energy in the long fibers to the energy in the long fibers for 100 GeV electrons was 0.62, and the ratio of the energy in the short fibers to that in the long fibers for 100 GeV electrons was 0.42. For 100 GeV electrons, the ratio of energy in the short fibers to that in the long fibers was 0.17. (Compare to values of about 0.7, 0.55, and 0.3 for long and short fiber pion ratios, and short fiber electron ratios, respectively, [23].)

3.2.3 PMT Hits

In agreement with the data from TB04 [28], in this simulation, hits are seen in the PMTs for 150 GeV Muons (Figure 3.5), 100 GeV Pions (Figure 3.6), and 50 GeV p_T Pythia jets (Figure 3.7). For muons, pions, and jets, there is a peak at about

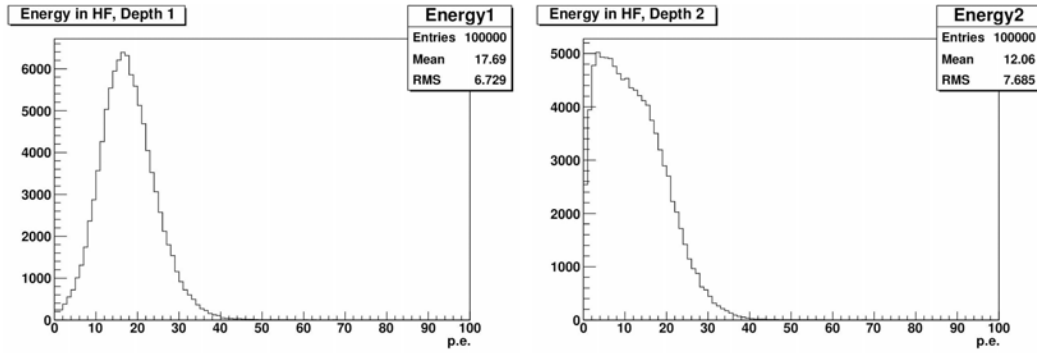


Figure 3.3: Energy in long and short fibers (depths 1 and 2, respectively) for 100 GeV Pions. Energies are in photoelectrons.

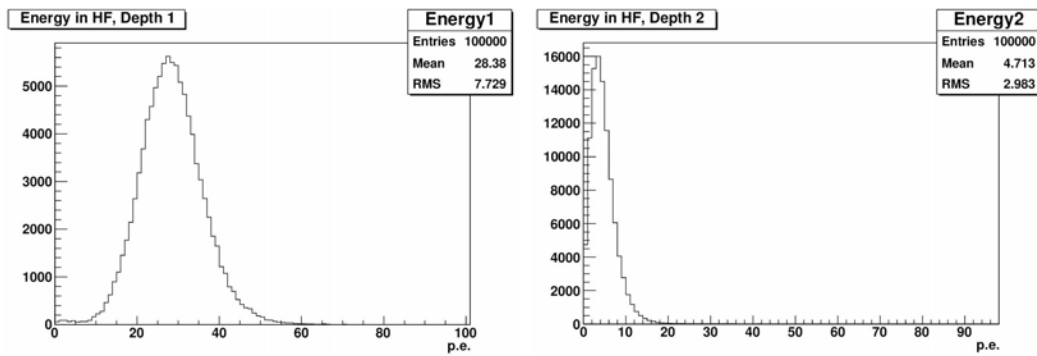


Figure 3.4: Energy in long and short fibers (depths 1 and 2, respectively) for 100 GeV Electrons. Energies are in photoelectrons.

50 photoelectrons. If a lower energy threshold of 12.5 photoelectrons (50 GeV) in the PMTs per event is imposed, 0.753% of pion, 17.8% of muon, and 3.70% of Pythia jet events are PMT events, where the incident particle is aimed at the PMT region, as explained earlier. Note that the numbers in Figures 3.5, 3.6, and 3.7 indicate the number of hits, and not the number of simulated events.

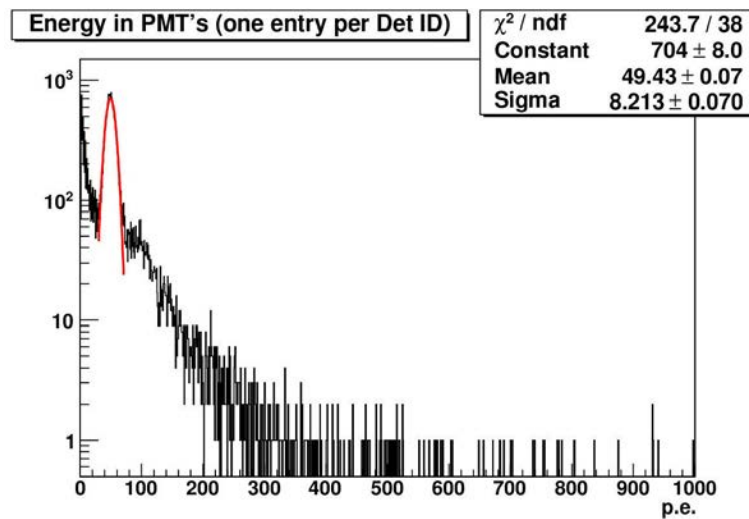


Figure 3.5: Energy in PMTs for 150 GeV Muons. Energy in photoelectrons. The red line is a gaussian fit of the peak only (30 p.e. < energy < 70 p.e.).

3.2.4 GenJets and RecJets for Pythia Jets

The p_T distribution (Figure 3.9) of the 50 GeV p_T Pythia jet dataset was investigated briefly. The GenJet p_T is also shown in Figure 3.8 to confirm the jet p_T . Figure 3.9 shows the p_T of the leading RecJet for all events in the left histogram, and the p_T of the leading RecJet for non-PMT events only in the right histogram,

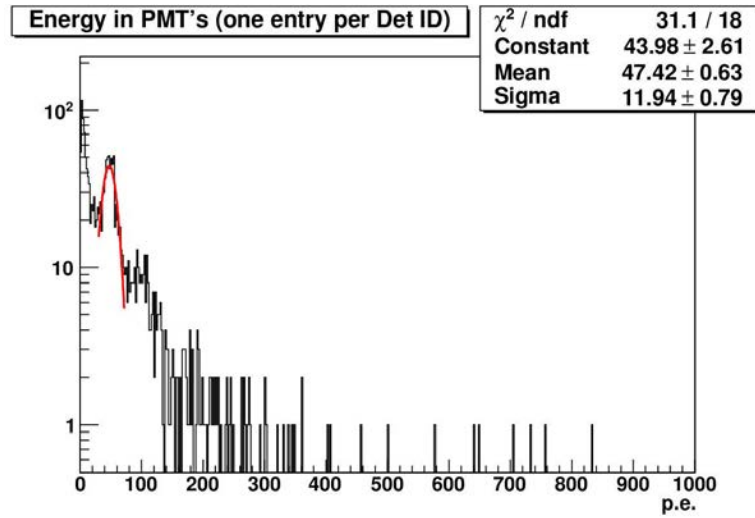


Figure 3.6: Energy in PMTs for 100 GeV Pions. Energy in photoelectrons. The red line is a gaussian fit of the peak only (30 p.e. < energy < 70 p.e.).

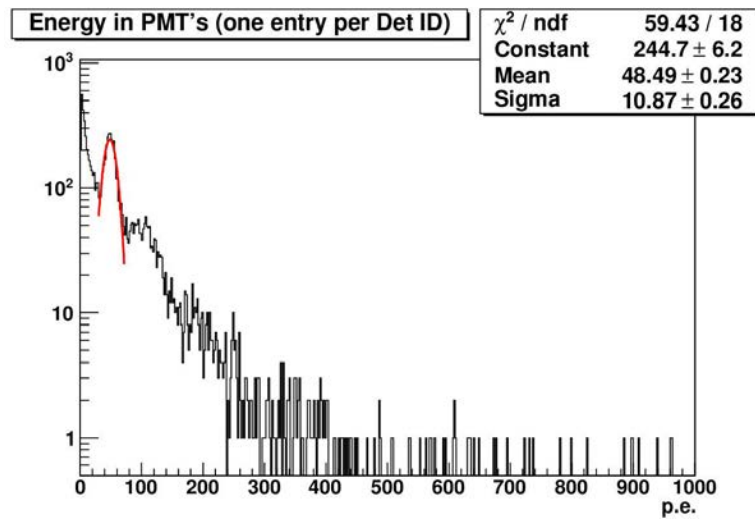


Figure 3.7: Energy in PMTs for 50 GeV p_T Pythia Jets. Energy in photoelectrons. The red line is a gaussian fit of the peak only (30 p.e. < energy < 70 p.e.).

with no energy cuts imposed. Even though roughly 4% of jet events are PMT events, only about 0.01% occur in the high energy tail. This may mislead some to believe that such events are of minimal impact. But for those trying to reconstruct physics events, a PMT hit that is not in the high p_T tail but that is still above jet p_T cuts will provide not only an incorrect value of p_T , but will provide incorrect geometrical information as well. Even though the pseudorapidity range of all PMT hits is roughly $3 \leq |\eta| \leq 3.2$ due to the location of the readout box behind HF, the PMT hit will have an η value that corresponds to the η of the tower corresponding to that PMT.

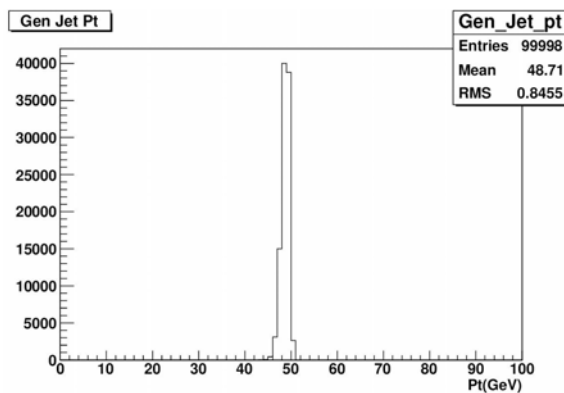


Figure 3.8: p_T of GenJets for 50 GeV p_T Pythia Jets.

3.2.5 Timing

Particles traveling through HF travel at close to the speed of light, while the signal traveling through the HF fibers travels at a reduced speed that is dependent on the index of refraction of the fiber material. This means that PMT events should

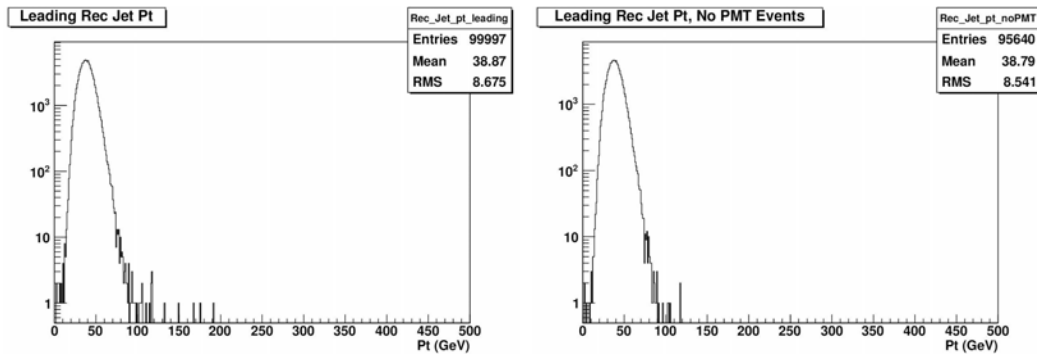


Figure 3.9: p_T of leading RecJet for 50 GeV p_T Pythia Jets. The left figure includes PMT events, the right figure does not.

occur at an earlier time than normal HF events. The energy weighted time is shown for muon, pion, and jet hits in Figures 3.11, 3.12, and 3.13, with pcalohit times on the left, and rechit times on the right. For all three cases, the PMT hit times peak at 46-47 ns for the pcalohits, while normal hits occur several ns later. Note that the time scales for pcalohits and rechits are not identical, as the pcalohit time is the time of flight from the interaction point taken from the generated ("true") information, while such information is not available for rechit times, which have a more arbitrary time scale. Although no PMT hits are expected for electrons, similar timing information for 100 GeV electrons is shown in Figure 3.10.

A few simple cuts based on the pcalohit times are summarized in Table 3.1. As can be seen from the table, if all events which have any hits with a time of less than 47 ns are rejected, 98.6% of PMT events and 6.5% of normal events for muons are eliminated, 88.8% of PMT events and 9.3% of normal events for pions are eliminated, and 93.6% of PMT events and 34.8% of normal events for jets are eliminated. It

should also be noted that all of the cuts used in the table eliminate approximately 4.5% of electron events. The problem is that changing the cut to either 46 or 48 ns significantly worsens the results. This suggests that nanosecond precision timing is necessary in order for timing based cuts to be effective. A hit by hit timing rather than an event by event timing based cut might be more efficient.

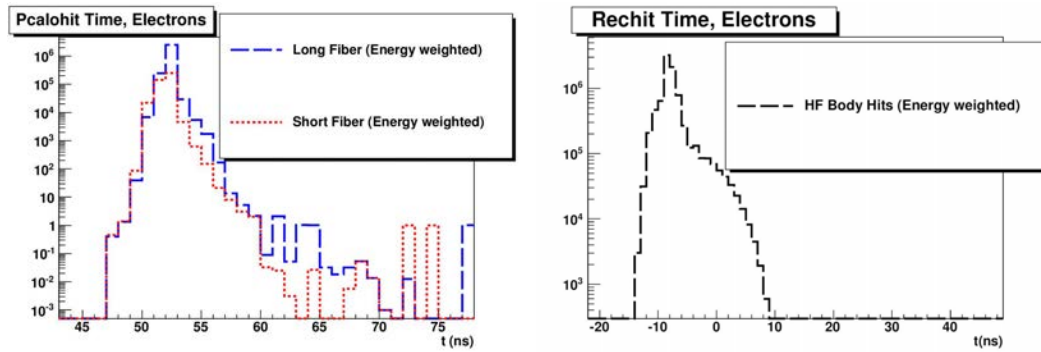


Figure 3.10: Timing information for 100 GeV Electrons. Pcalohit time on the left, rechit time on the right. Time in ns.

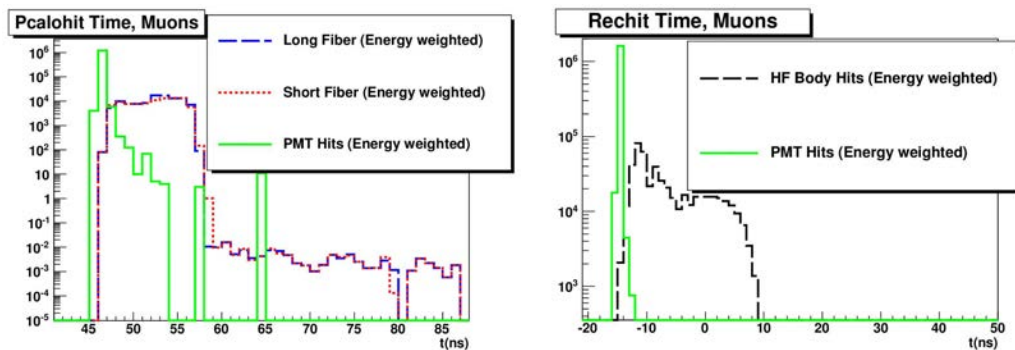


Figure 3.11: Timing information for 150 GeV Muons. PMT hits are indicated by the green line. Pcalohit time on the left, rechit time on the right. Time in ns.

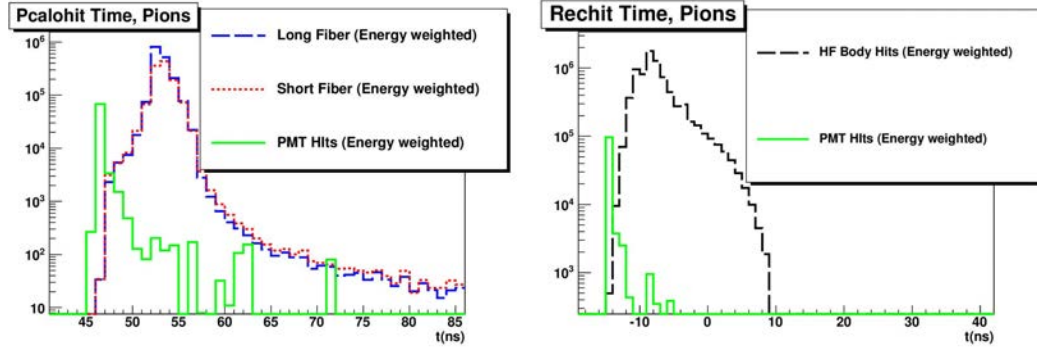


Figure 3.12: Timing information for 100 GeV Pions. PMT hits are indicated by the green line. Pcalohit time on the left, rechit time on the right. Time in ns.

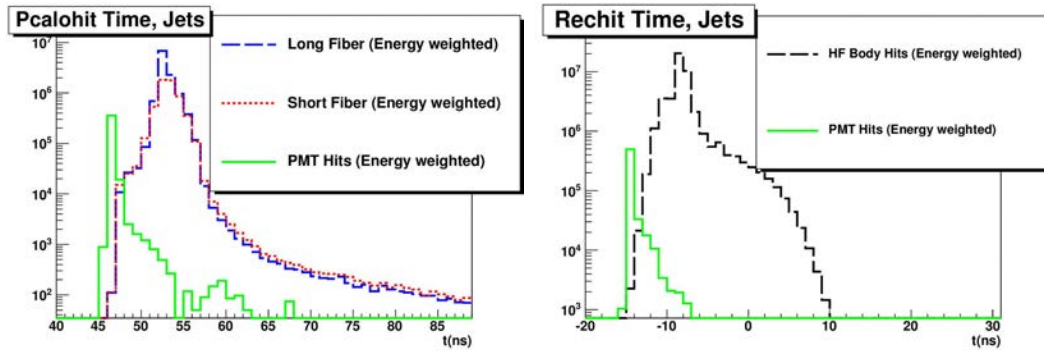


Figure 3.13: Timing information for 50 GeV p_T Pythia Jets. PMT hits are indicated by the green line. Pcalohit time on the left, rechit time on the right. Time in ns.

The only currently available timing information is contained in 25 ns time slices, as the CMS software only stores timing information in 25 ns bins. The ADC counts (which are proportional to the energy measured) for 150 GeV muons, 100 GeV pions, and 50 GeV p_T Pythia jets are shown in Figures 3.14, 3.15, and 3.16. Non-

Table 3.1: Events eliminated for both PMT and normal events when all events with hits of less than 46, 47, 48, 49, or 50 ns are rejected.

Particle	Cutoff Time (ns)	PMT Events	Normal Events
Muon	46	161 (0.8%)	247 (0.3%)
Muon	47	19570 (98.6%)	5229 (6.5%)
Muon	48	19849 (99.9%)	76375 (95.3%)
Muon	49	19853 (100%)	80146 (100%)
Muon	50	19853 (100%)	80146 (100%)
Pion	46	64 (7.0%)	8694 (8.8%)
Pion	47	815 (88.8%)	9214 (9.3%)
Pion	48	912 (99.3%)	20710 (20.9%)
Pion	49	915 (99.7%)	32104 (32.4%)
Pion	50	917 (99.9%)	53646 (54.1%)
Jet	46	1512 (34.7%)	31991 (33.4%)
Jet	47	4078 (93.6%)	33279 (34.8%)
Jet	48	4352 (99.9%)	57874 (60.5%)
Jet	49	4357 (100%)	72192 (75.5%)
Jet	50	4357 (100%)	86193 (90.1%)

PMT events are on the left, PMT events are on the right. These plots show the total ADC counts for the respective event types in each dataset. Dividing by the number of events would give an average pulse shape. Non-PMT events occur in time slice 3, while PMT hits occur early enough that there is significant energy sharing between time slices 2 and 3. A PMT hit detection algorithm based on energy sharing may be rather effective with simulated data, where the phase can be adjusted precisely, where the phase refers to the timing relative to the LHC clock. The effectiveness of such a technique on real data would be dependent on how precisely the phase can be adjusted using the actual CMS electronics.

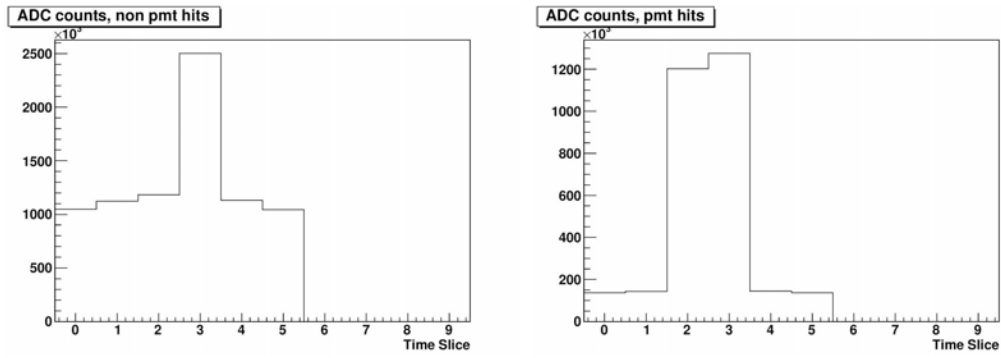


Figure 3.14: Total ADC counts for 150 GeV Muons. Non-PMT events on the left, PMT events on the right.

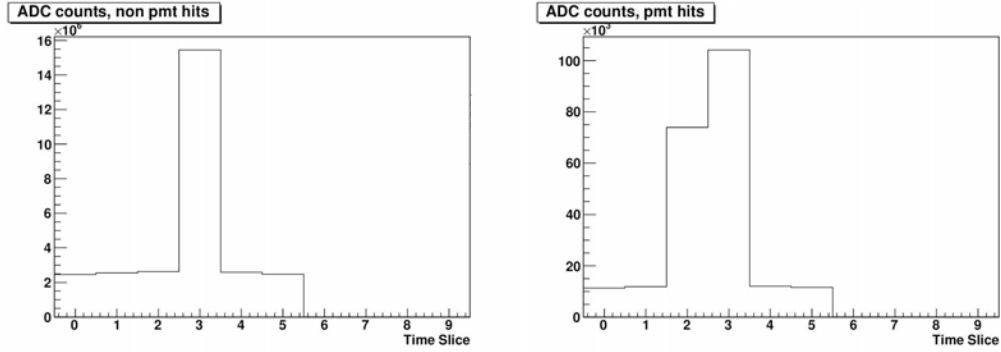


Figure 3.15: Total ADC counts 100 GeV Pions. Non-PMT events on the left, PMT events on the right.

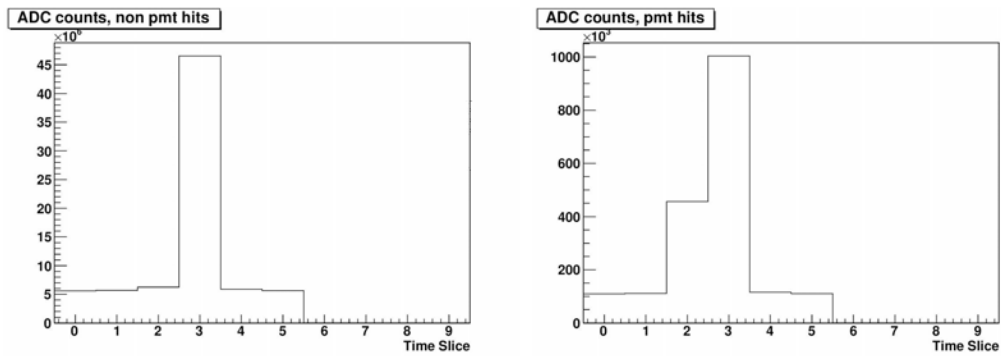


Figure 3.16: Total ADC counts for 50 GeV p_T Pythia Jets. Non-PMT events on the left, PMT events on the right.

3.2.6 $S/(L+S)$

A PMT hit detection method utilizing the energy in the long (L) and short fibers (S) was used to analyze data from the 2004 HF testbeam. See the previous chapter as well as [28]. A PMT in the readout box corresponds to only long or short fibers for a tower. Because of this, a PMT hit should only register a hit in the long or the short fibers, but not both. Using the formula $S/(L+S)$, a hit in a long fiber PMT would have an $S/(L+S)$ value of 0, and a hit in a short fiber PMT would have an $S/(L+S)$ value of 1. As shown in Figures 3.17, 3.18, 3.19, 3.20, and 3.21, this would work reasonably well for identifying abnormal events for muons and for hadronic decays such as pions, but could be problematic for early electromagnetic showering particles such as electrons. For both the testbeam and simulated electrons (Figure 3.17), there are many electrons with $S/(L+S)$ values close to zero, indicating that the energy is primarily in the long fibers.

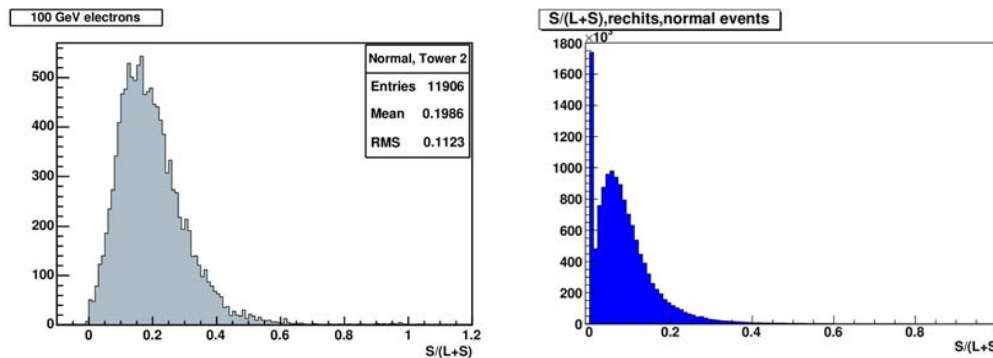


Figure 3.17: $S/(L+S)$ for 100 GeV electrons. Testbeam on the left [28], simulation on the right.

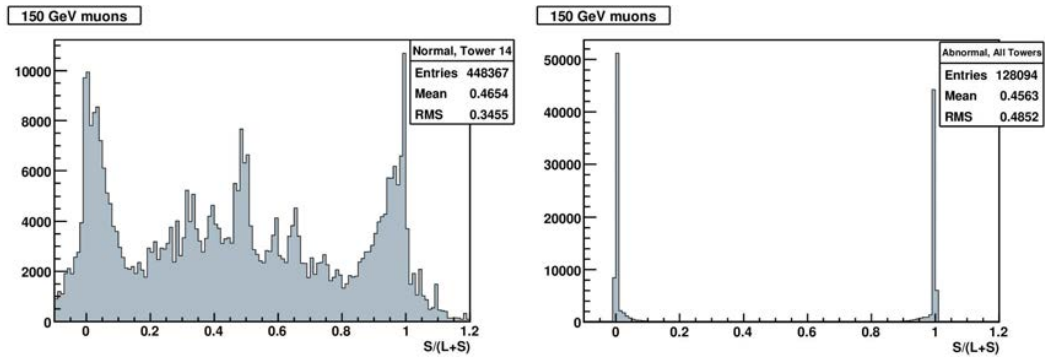


Figure 3.18: $S/(L+S)$ for 150 GeV muons, testbeam. "Normal" events on the left, "Abnormal" events on the right [28].

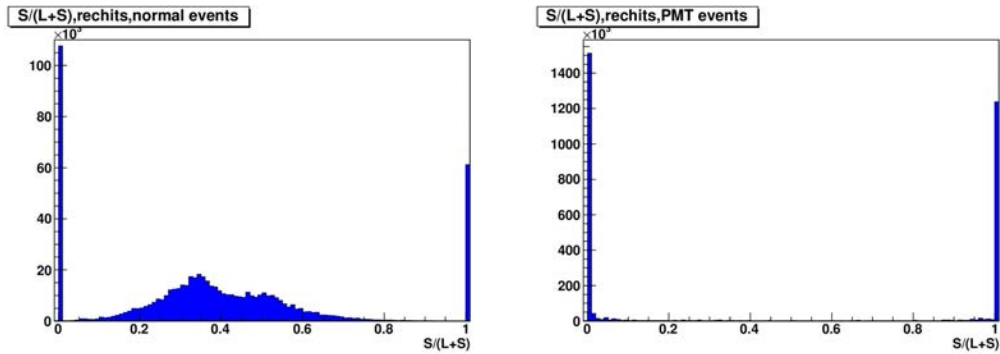


Figure 3.19: $S/(L+S)$ for 150 GeV muons, simulation. Non-PMT events on the left, PMT events on the right.

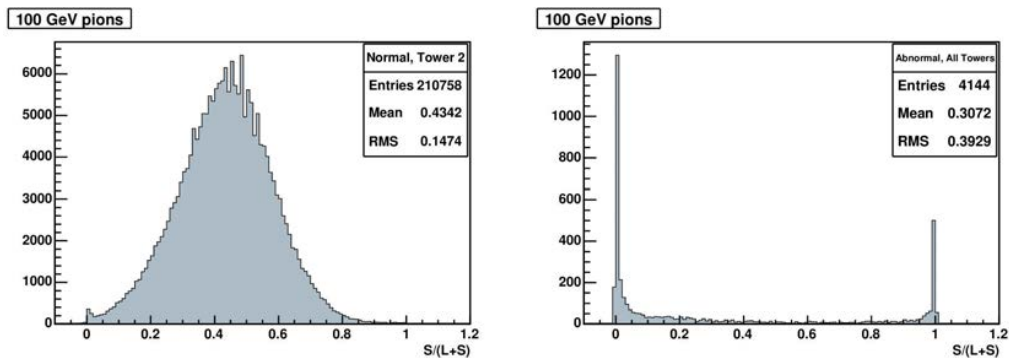


Figure 3.20: $S/(L+S)$ for 100 GeV pions, testbeam. "Normal" events on the left, "Abnormal" events on the right [28].

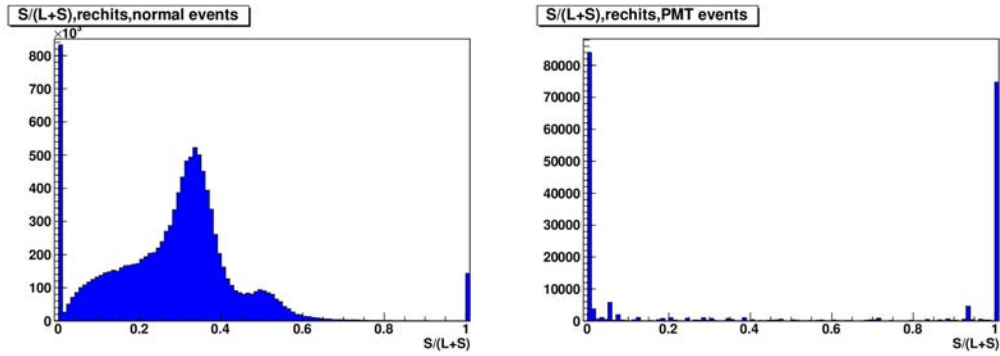


Figure 3.21: $S/(L+S)$ for 100 GeV pions, simulation. Non-PMT events on the left, PMT events on the right.

3.2.7 $(L-S)/(L+S)$

A slightly different algorithm has become more favored for trying to detect PMT events in collision data. Instead of $S/(L+S)$, $(L-S)/(L+S)$ is being used. The values of $(L-S)/(L+S)$ for simulated electrons, muons, pions and Pythia jets are shown in Figures 3.22, 3.23, 3.24, and 3.25. It is similar to the previous algorithm, but now hits in long fiber PMTs have values of +1, and hits in short fiber PMTs have values of -1. It is likely that events with values of $(L-S)/(L+S)$ near -1 can be rejected as PMT hits, but those with values of +1 must be treated more carefully, as it is possible for an early showering particle such as an electron to have an $(L-S)/(L+S)$ value close to +1.

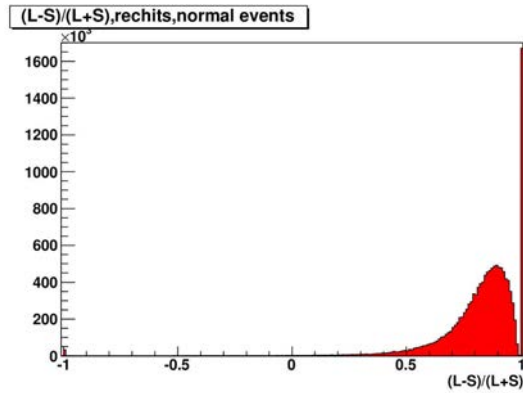


Figure 3.22: $(L-S)/(L+S)$ for 100 GeV electrons.

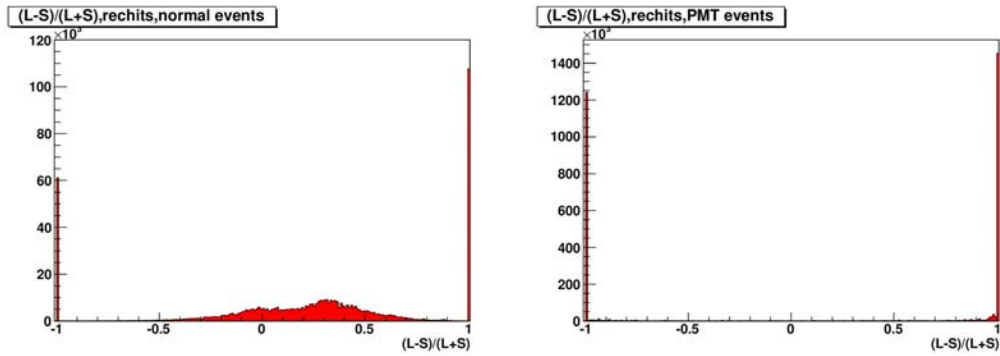


Figure 3.23: $(L-S)/(L+S)$ for 150 GeV muons. Non-PMT events on the left, PMT events on the right.

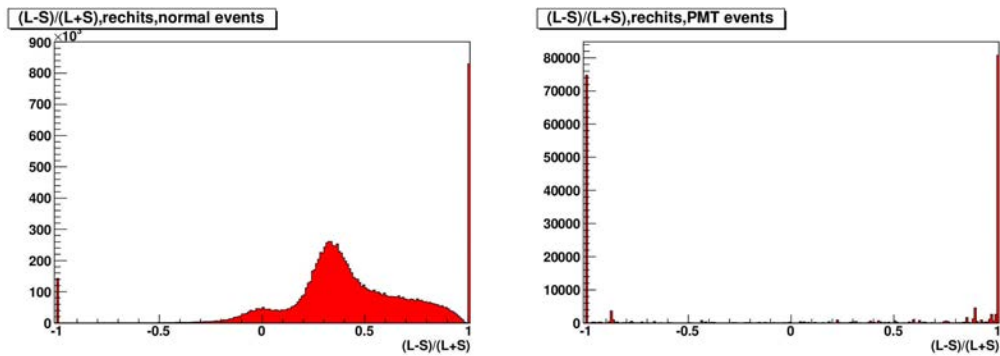


Figure 3.24: $(L-S)/(L+S)$ for 100 GeV pions. Non-PMT events on the left, PMT events on the right.

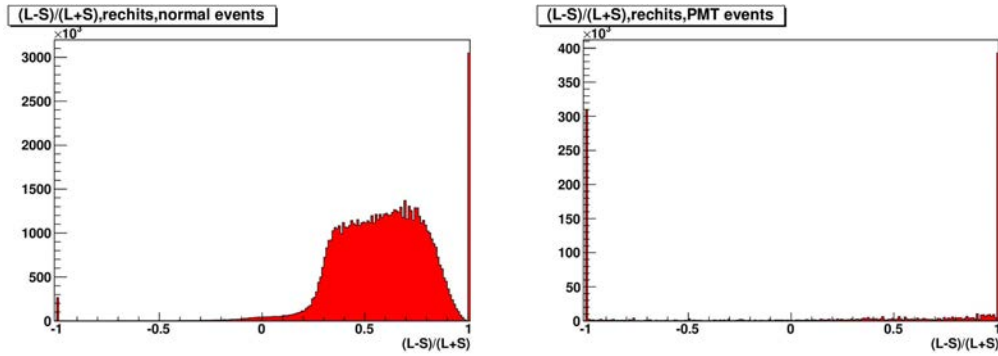


Figure 3.25: $(L-S)/(L+S)$ for 50 GeV p_T Pythia Jets. Non-PMT events on the left, PMT events on the right.

Table 3.2: Number of events per dataset.

COM Energy (TeV)	No. of Events
7	96000
10	93000
14	95000

3.3 Simulation of PMT Hits for Minimum

Bias Events

3.3.1 Datasets

The Monte Carlo datasets used in this study were generated with Pythia using CMSSW_3_5_2. About 100,000 minimum bias events were generated for collision energies of 7, 10 and 14 TeV (The actual number of events varies somewhat for each energy, and can be found in Table 3.2).

3.3.2 PMT Hits

In agreement with the data from TB04 [28], in the single particle study, hits were seen in the PMTs for muons and pions. For single particles, a peak was seen at about 50 photoelectrons. See reference [30] for more on PMT hits with single particles, including rates.

For all three minimum bias datasets, a peak was also seen at about 50 photoelectrons. If a lower energy threshold of 12.5 photoelectrons (50 GeV) in the PMTs per event is imposed, 0.70% of 7 TeV, 0.85% of 10 TeV, and 0.93% of 14 TeV minimum bias events are PMT events. Note that the numbers in Figures 3.43, 3.27, and 3.28 indicate the number of hits, and not the number of simulated events. These figures show only the energy deposited in the PMT windows, and do not include the energy in the long and short fibers from the body of HF.

3.3.3 RecJet Distributions

The RecJet (iterative cone 5 calojet) p_T distribution (Figures 3.45, 3.30, 3.31) of the different minimum bias samples was investigated briefly. The figures show the RecJet p_T of the leading jet for the case where PMT hit events were excluded as well as for all events. From the figures it can be seen that the PMT hits do not necessarily create a high energy tail, but do create a small but noticeable number of events throughout the distribution. This may mislead some to believe that such events are of minimal impact. But for those trying to reconstruct physics events, a PMT hit that is not in the high p_T tail but that is still above jet p_T cuts will provide not only

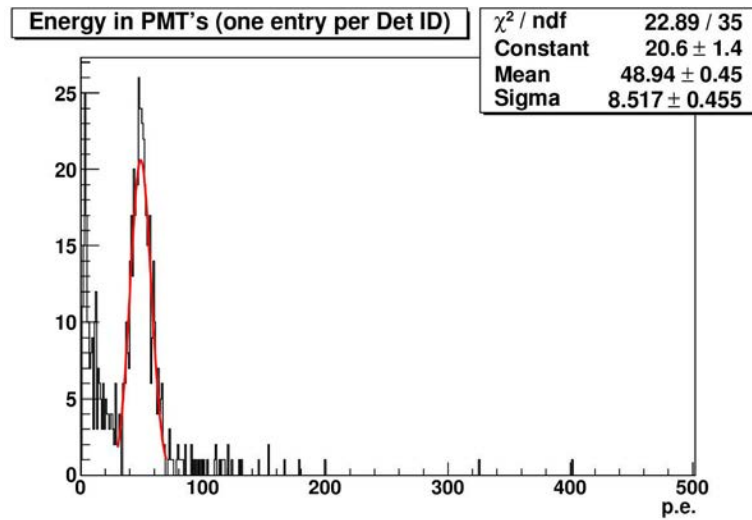


Figure 3.26: Energy in PMTs for 7 TeV minimum bias events. Energy in photoelectrons. The red line is a gaussian fit of the peak only (30 p.e. < energy < 70 p.e.)

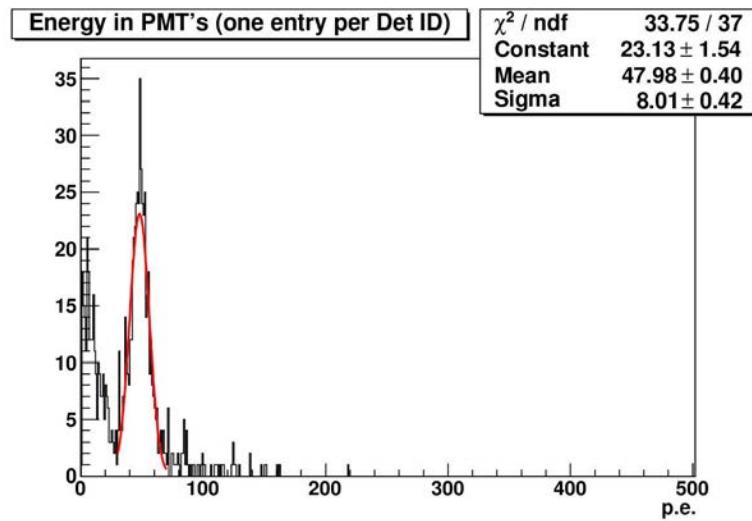


Figure 3.27: Energy in PMTs for 10 TeV minimum bias events. Energy in photoelectrons. The red line is a gaussian fit of the peak only (30 p.e. < energy < 70 p.e.)

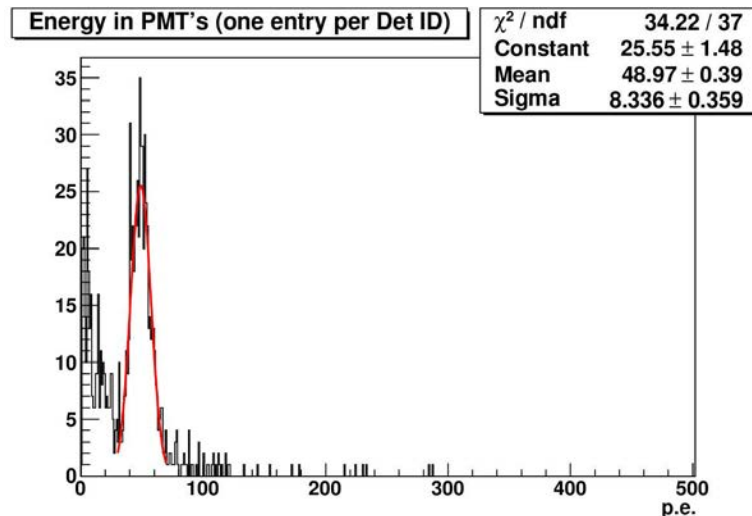


Figure 3.28: Energy in PMTs for 14 TeV minimum bias events. Energy in photoelectrons. The red line is a gaussian fit of the peak only (30 p.e. < energy < 70 p.e.)

an incorrect value of p_T , but will provide incorrect geometrical information as well. Even though the pseudorapidity range of all PMT hits is roughly $3 \leq |\eta| \leq 3.2$ due to the location of the readout box behind HF, the PMT hit will have an η value that corresponds to the η of the tower corresponding to that PMT.

3.3.4 Timing

Particles traveling through HF travel at close to the speed of light, while the signal traveling through the HF fibers travels at a reduced speed that is dependent on the index of refraction of the fiber material. This means that PMT events should occur at an earlier time than normal HF events. The energy weighted time is shown for 7, 10, and 14 TeV minimum bias event hits in Figures 3.32, 3.33, and 3.34, with pcalohit times on the left, and rechit times on the right. For all three cases, the PMT

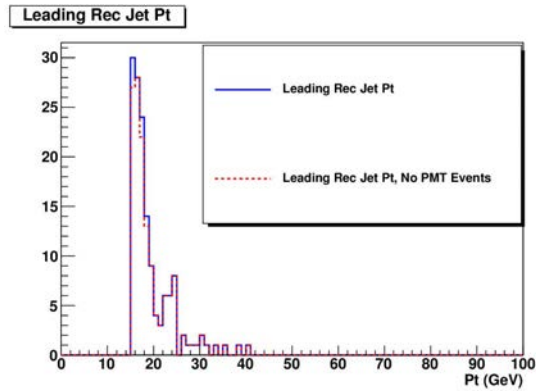


Figure 3.29: p_T of RecJets for 7 TeV minimum bias events. The solid blue line is the leading RecJet p_T for all events, the dotted red line excludes PMT hit events.

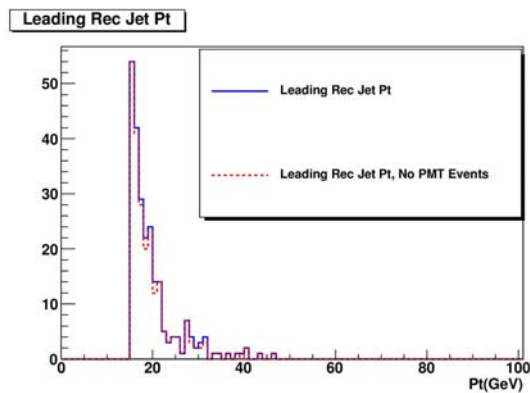


Figure 3.30: p_T of RecJets for 10 TeV minimum bias events. The solid blue line is the leading RecJet p_T for all events, the dotted red line excludes PMT hit events.

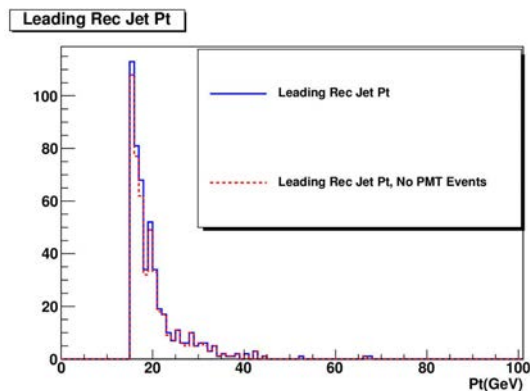


Figure 3.31: p_T of RecJets for 14 TeV minimum bias events. The solid blue line is the leading RecJet p_T for all events, the dotted red line excludes PMT hit events.

hit times peak at 46-47 ns for the pcalohits, while normal hits occur several ns later. Note that the time scales for pcalohits and rechits are not identical, as the pcalohit time is the time of flight from the interaction point, while such information is not available for rechit times, which have a more arbitrary time scale.

A few simple cuts based on the pcalohit times are summarized in Table 3.3. As can be seen from the table, if all events which have any hits with a time of less than 48 ns are rejected, in all three cases more than 85% of PMT hit events can be rejected, but as much as one third of non PMT events would also be rejected. Changing the cut by even 2 or 3 ns can make a significant difference. This suggests that nanosecond precision timing is necessary in order for timing based cuts to be effective. A hit by hit timing rather than an event by event timing based cut might be more efficient.

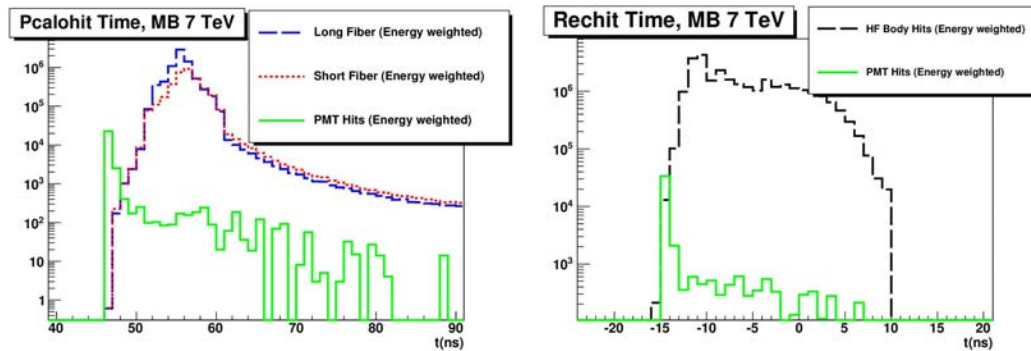


Figure 3.32: Timing information for 7 TeV minimum bias events. Pcalohit time on the left, rechit time on the right. Time in ns.

The only currently available timing information is contained in 25 ns time

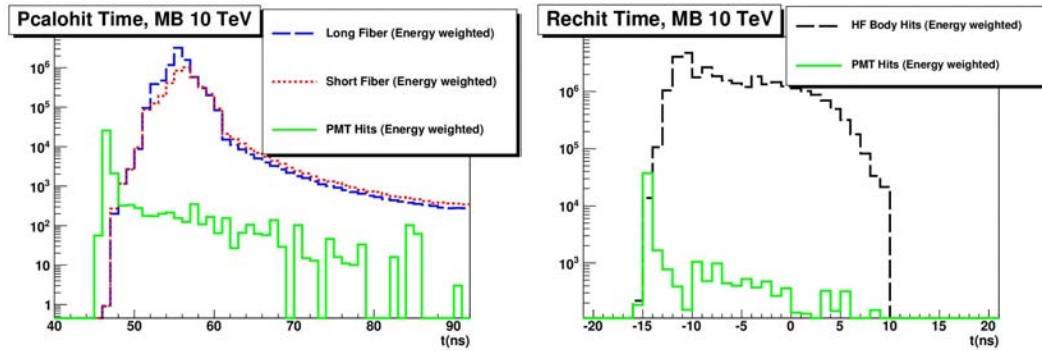


Figure 3.33: Timing information for 10 TeV minimum bias events. PMT hits are indicated by the green line. Pcalohit time on the left, rechit time on the right. Time in ns.

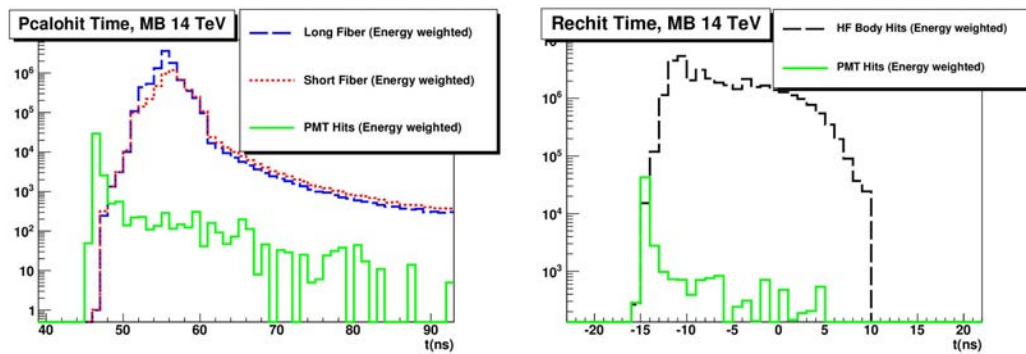


Figure 3.34: Timing information for 14 TeV minimum bias events. PMT hits are indicated by the green line. Pcalohit time on the left, rechit time on the right. Time in ns.

Table 3.3: Events eliminated for both PMT and normal events when all events with hits of less than 46, 47, 48, 49, or 50 ns are rejected.

COM Energy (TeV)	Cutoff Time (ns)	PMT Events	Normal Events
7	46	337 (48.1%)	24751 (26.0%)
7	47	563 (80.3%)	24794 (26.0%)
7	48	19849 (85.3%)	27674 (29.0%)
7	49	19853 (88.3%)	32209 (33.8%)
7	50	19853 (90.9%)	40754 (42.8%)
10	46	434 (53.1%)	25638 (27.8%)
10	47	677 (82.8%)	25680 (27.8%)
10	48	716 (87.5%)	28606 (31.0%)
10	49	742 (90.7%)	32987 (35.8%)
10	50	917 (92.5%)	41195 (44.7%)
14	46	504 (55.1%)	28027 (29.8%)
14	47	756 (82.6%)	28080 (29.8%)
14	48	792 (86.6%)	31014 (33.0%)
14	49	810 (88.5%)	35424 (37.7%)
14	50	834 (91.1%)	43574 (46.3%)

slices. This explains why there is not a clear separation between the rechit times for PMT hit and non PMT hit times. The ADC counts for all three energies are shown in Figures 3.35, 3.36, and 3.37. Non-PMT events are on the left, PMT events are on the right. These plots show the total ADC counts for each dataset. Dividing by the number of events would give an average pulse shape. Non-PMT events clearly occur in time slice 3, while for some events PMT hits occur early enough that there is some energy sharing between time slices 2 and 3, as indicated by the small shoulder in time slice 2 for the PMT hit plots. The energy sharing between time slices 2 and 3 is not as significant as was seen in the single particle study [30]. A PMT hit detection algorithm based on energy sharing may be rather effective with simulated

data, where the phase can be adjusted precisely. The effectiveness of such a technique on real data would be dependent on how precisely the phase can be adjusted using the actual CMS electronics.

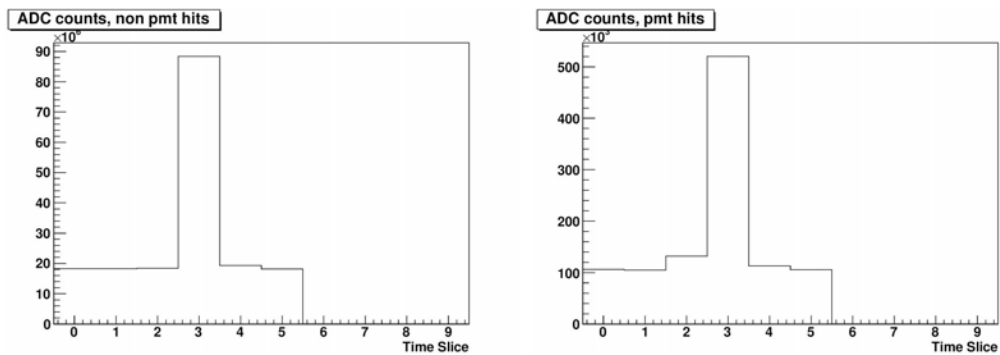


Figure 3.35: Total ADC counts for 7 TeV minimum bias events. Non-PMT events on the left, PMT events on the right.

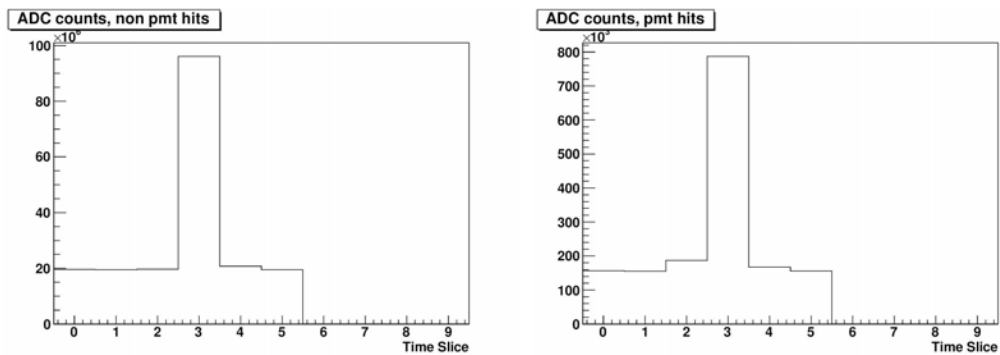


Figure 3.36: Total ADC counts for 10 TeV minimum bias events. Non-PMT events on the left, PMT events on the right.

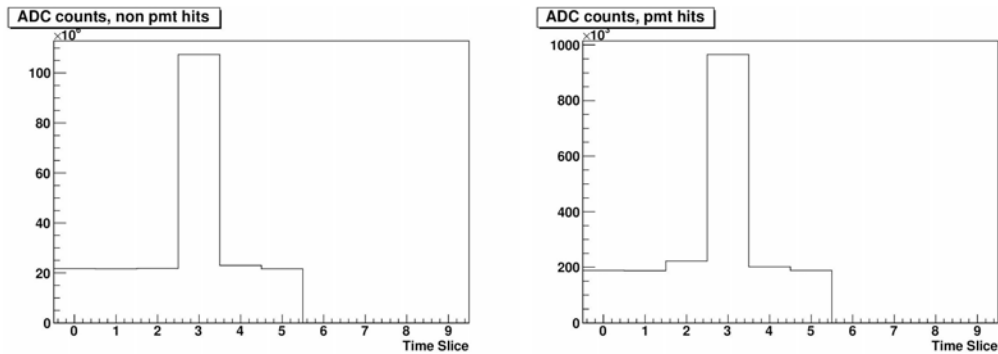


Figure 3.37: Total ADC counts for 14 TeV minimum bias events. Non-PMT events on the left, PMT events on the right.

3.3.5 $(L-S)/(L+S)$

The values of $(L-S)/(L+S)$ for the three different energies of minimum bias events are shown in Figures 3.38, 3.39, and 3.40. Hits in long fiber PMTs have values of +1, and hits in short fiber PMTs have values of -1. It is likely that events with values of $(L-S)/(L+S)$ near -1 can be rejected as PMT hits, but those with values of +1 must be treated more carefully, as it is possible for an early showering particle such as an electron to have an $(L-S)/(L+S)$ value close to +1. See references [28] and [30].

3.4 Comparison of Two Different PMT

Window Thicknesses

3.4.1 Datasets

Datasets of about 100,000 events for 150 GeV muons, 50 GeV p_T Pythia jets, and 7 TeV minimum bias events were generated for both window thicknesses (6 mm and 0.6 mm). The thick window muons and Pythia jets were generated in

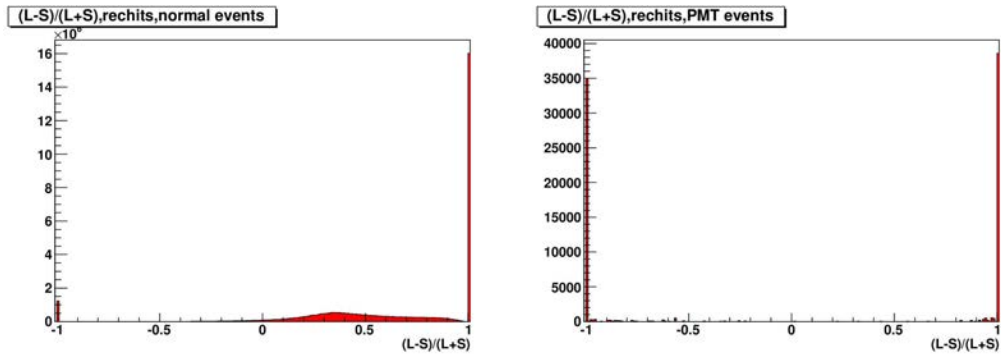


Figure 3.38: $(L-S)/(L+S)$ for 7 TeV minimum bias events. Non-PMT events on the left, PMT events on the right.

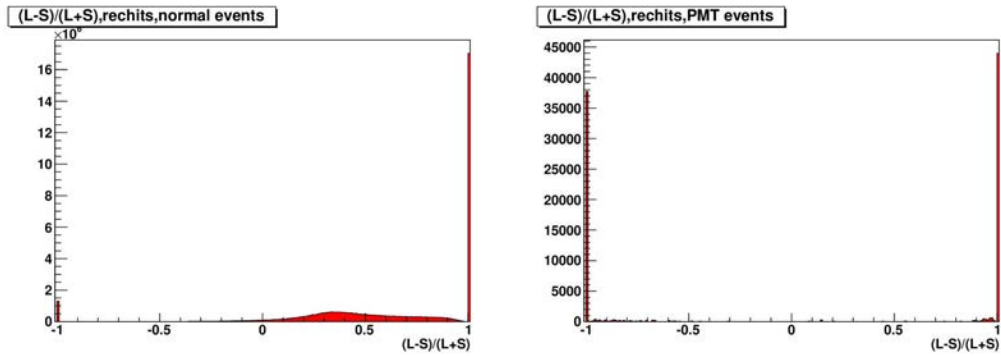


Figure 3.39: $(L-S)/(L+S)$ for 10 TeV minimum bias events. Non-PMT events on the left, PMT events on the right.

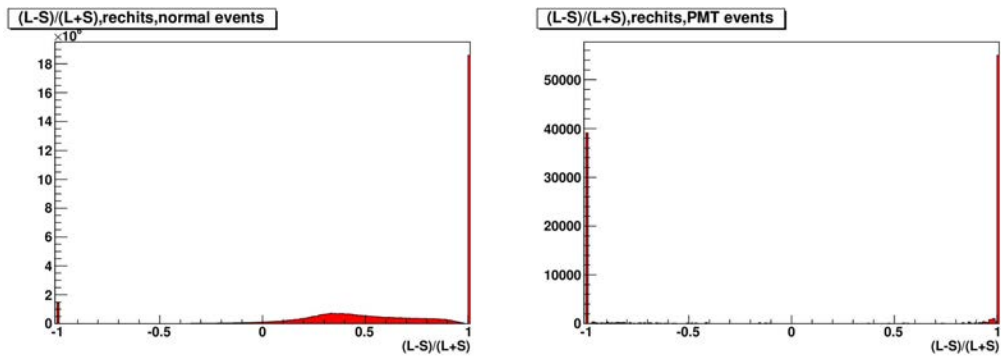


Figure 3.40: $(L-S)/(L+S)$ for 14 TeV minimum bias events. Non-PMT events on the left, PMT events on the right.

CMSSW_3_2_4. All other datasets were generated in CMSSW_3_5_2. All datasets were analyzed using CMSSW_3_5_2.

3.4.2 PMT Hits

In agreement with the data from TB04 [28], in the single particle study, hits were seen in the PMTs for muons and pions. For single particles, Pythia jets, and minimum bias events, a peak was seen at about 50 photoelectrons (200 GeV).

Figures 3.41, 3.42, and 3.43 show the energy deposited in the PMT windows for 150 GeV Muons, 50 GeV p_T Pythia jets, and 7 TeV minimum bias events, respectively. Note that these figures show only the energy deposited in the PMT windows, and do not include the energy in the long and short fibers from the body of HF. In all three cases, the location of the peak drops from about 50 p.e. for the 6 mm window to about 5 p.e. for the 0.6 mm window. For more details on the amount of Cerenkov radiation produced in the glass window, see the Cerenkov radiation discussion in the previous chapter. If a lower threshold of 12.5 p.e. (50 GeV) is imposed, the number of PMT hits seem in muons drops quite dramatically for the thinner window (from 18.0% to 1.5%). A significant, although not as dramatic, decrease is also seen for the minimum bias events (from 0.70% to 0.37%), and Pythia jets (from 4.4% to 3.2%).

3.4.3 RecJet Distributions

The RecJet (iterative cone 5 calojet) p_T distributions for 50 GeV Pythia jets and 7 TeV minimum bias events are shown in Figures 3.44 and 3.45, respectively. In both figures, the case with a 6 mm thick window is shown on the left, and the 0.6 mm

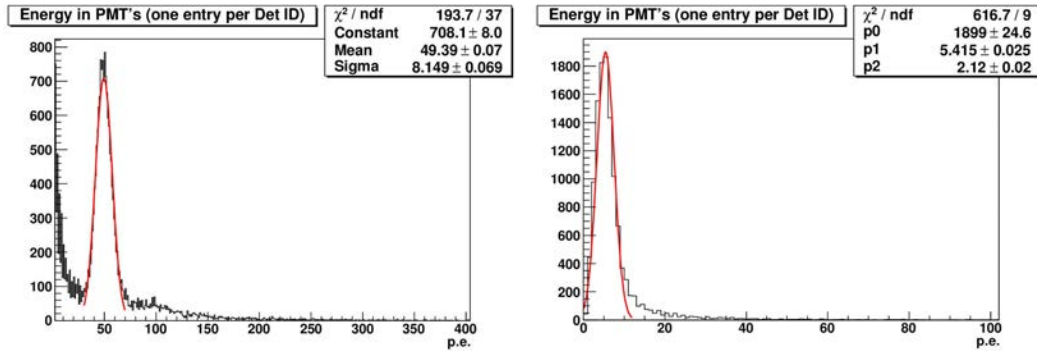


Figure 3.41: Energy in PMT's for 150 GeV muons. Results for the 6 mm window on the left, 0.6 mm window on the right. Energy in photoelectrons. The red line is a gaussian fit of the peak only.

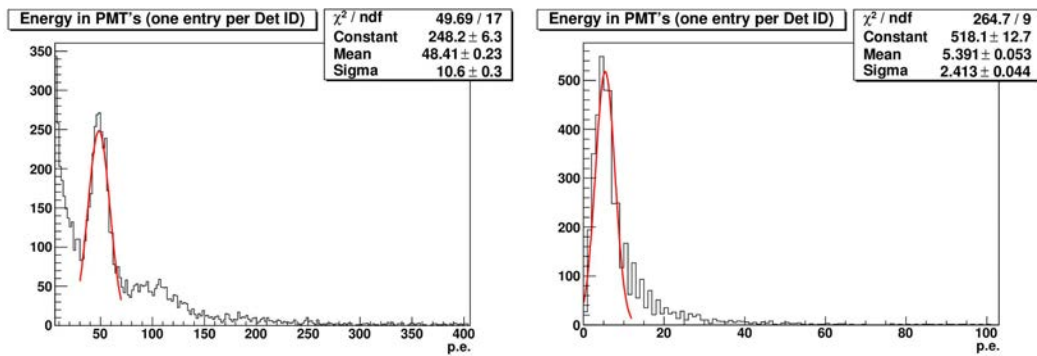


Figure 3.42: Energy in PMT's for 50 GeV p_T Pythia jets. Results for the 6 mm window on the left, 0.6 mm window on the right. Energy in photoelectrons. The red line is a gaussian fit of the peak only.

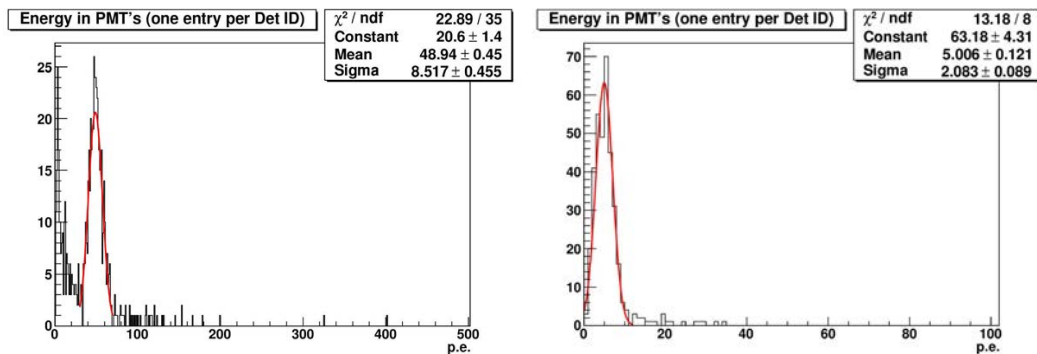


Figure 3.43: Energy in PMT's for 7 TeV minimum bias events. Results for the 6 mm window on the left, 0.6 mm window on the right. Energy in photoelectrons. The red line is a gaussian fit of the peak only.

window on the right. While differences can be seen for both the Pythia jets and the minimum bias events, the most dramatic difference is seen for the Pythia jets. When a lower cut of 15 GeV in p_T is imposed, a large number of the fake jets created from PMT window hits fall below the threshold in the 0.6 mm case. The high energy tail seen for the 6 mm case is eliminated. This indicates that if a thinner PMT window is used, a large number of the fake jets created will likely go unnoticed as the jet p_T threshold in most studies is at least 30 GeV.

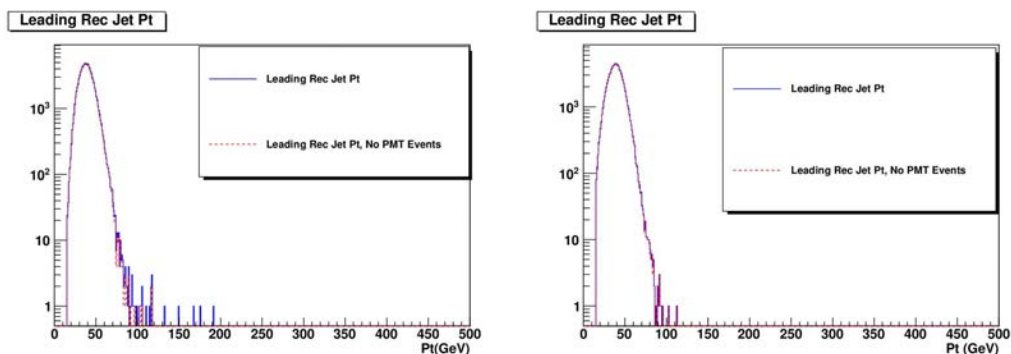


Figure 3.44: p_T of RecJets for 50 GeV Pythia jets. Results for the 6 mm window on the left, 0.6 mm window on the right. The solid blue line is the leading RecJet p_T for all events, the dotted red line excludes PMT hit events.

3.5 Discussion of HF PMT Simulation Results

The inclusion of PMT windows in the HF simulation show that showering particles from minimum bias events can leak out of HF and strike the PMT window, creating a large signal from Cerenkov radiation. Upon reconstructing jets, relatively few fake jets from these PMT hits are in the high p_T tail. Yet any of these hits that

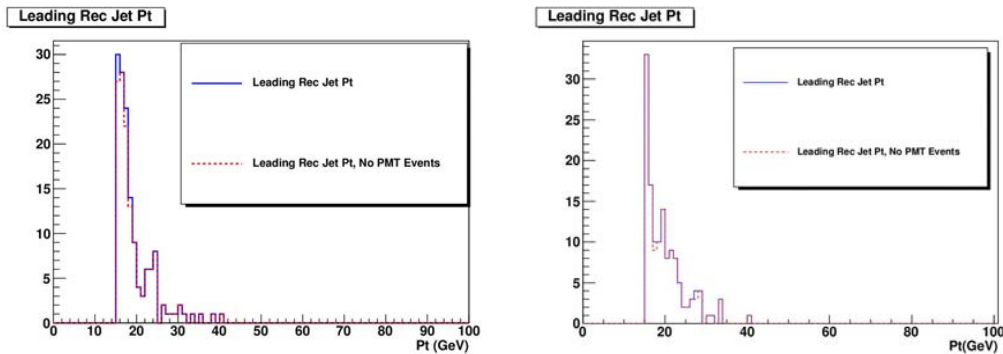


Figure 3.45: p_T of RecJets for 7 TeV minimum bias events. Results for the 6 mm window on the left, 0.6 mm window on the right. The solid blue line is the leading RecJet p_T for all events, the dotted red line excludes PMT hit events.

pass jet p_T thresholds in either the trigger or individual analyses would yield incorrect geometrical information in addition to incorrect values of p_T .

Timing would be an ideal way to distinguish PMT hits from non-PMT hits, as PMT hits typically occur several nanoseconds before non-PMT hits, but this would require more detailed timing information than is currently available in CMS.

If the phase could be properly adjusted, it may be possible to have PMT hits occur in the time slice prior to that in which the HF signal normally occurs. Some form of energy sharing algorithm would then be possible. This could work well in the simulation, but timing jitter in the actual experiment could be problematic for such a detection system.

Detection algorithms utilizing the energy in long and short fibers are promising, but one must be careful not to exclude early showering particles such as electrons, which may deposit much of their energy in the long fibers.

If a PMT with a thinner window were used, less Cerenkov radiation is gener-

ated, creating a smaller spurious signal. It is quite possible that the majority of fake jets created from PMT hits will fall below the lower jet p_T limits imposed by most studies.

The results of these HF PMT simulations led to a study on replacing the original HF PMTs with a new PMT with a thinner window, as well as segmented anodes which can be used to help detect such abnormal events [33], [35].

CHAPTER 4 VECTOR BOSON FUSION HIGGS

4.1 The Standard Model

The Standard Model is the currently accepted description of matter. All major components of the standard model have been verified experimentally (See the introductory sections of Chapter 1 for a list of major discoveries in particle physics). Several theories which are extensions of the standard model (Supersymmetry, Grand Unification Theories, etc.) have sound theoretical backgrounds, but have not yet been confirmed experimentally. A diagram of the components of the Standard Model is shown in Figure 4.1. In the standard model, all matter is composed of leptons, quarks, and bosons (also referred to as mediators or force carriers). [37]

There are six leptons. They are the electron, the muon, the tau, and their corresponding neutrinos. The elementary unit of charge is the charge of an electron ($-1.602 \times 10^{-19}\text{C}$). The muon and tau have the same charge as the electron (the *positive* value of this charge is referred to as e), while the neutrinos have a charge of 0 and are nearly massless. The electron is contained in everyday matter, muons can be seen in cosmic rays, but taus are not seen without an accelerator. Each lepton has a corresponding anti-particle, for a total of 12 leptons.

There are six quarks: up, down, strange, charm, top, and bottom (the bottom quark is still occasionally referred to as beauty). Quarks have a charge that is either $1/3$ or $2/3$ (positive or negative) of e , but only occur naturally in ways that yield an

integer multiple of e . For example, a proton consists of two up quarks and one down quark for a total charge of positive e , while a neutron consists of one up quark and two down quarks, giving it a net charge of zero (See Figure 4.1 for the charge of each quark). Everyday matter only contains up or down quarks. Particles containing charm, strange, top, or bottom quarks are referred to as exotic matter. As with the leptons, each quark has an oppositely charged anti-particle. In addition to this, each quark and anti-quark can be found in three "colors", which refer to the color quanta of r, g, and b, which combine to form colorless particles.

The final category are the force carrier bosons. The photon is the mediator of the electromagnetic force, and is massless. The gluon, the mediator of the strong force, is also massless. The weak force, however, is somewhat different. It has three mediator bosons: a positive and negatively charged W and a Z. Unlike the photon and gluon, the W and Z are *not* massless.

4.2 The Higgs Boson

If the electromagnetic and weak forces can truly be combined into one electroweak force, the standard model initially called for the force carrier bosons (the photon, the positively and negatively charged W, and the Z) to be massless. But as mentioned in the previous section, the photon is indeed massless, but the W and Z are not. This is referred to as electroweak symmetry breaking. In the 1960s Francois Englert [40] and Peter W. Higgs [39] independently developed the theoretical framework for how this electroweak symmetry breaking can be accounted for in the

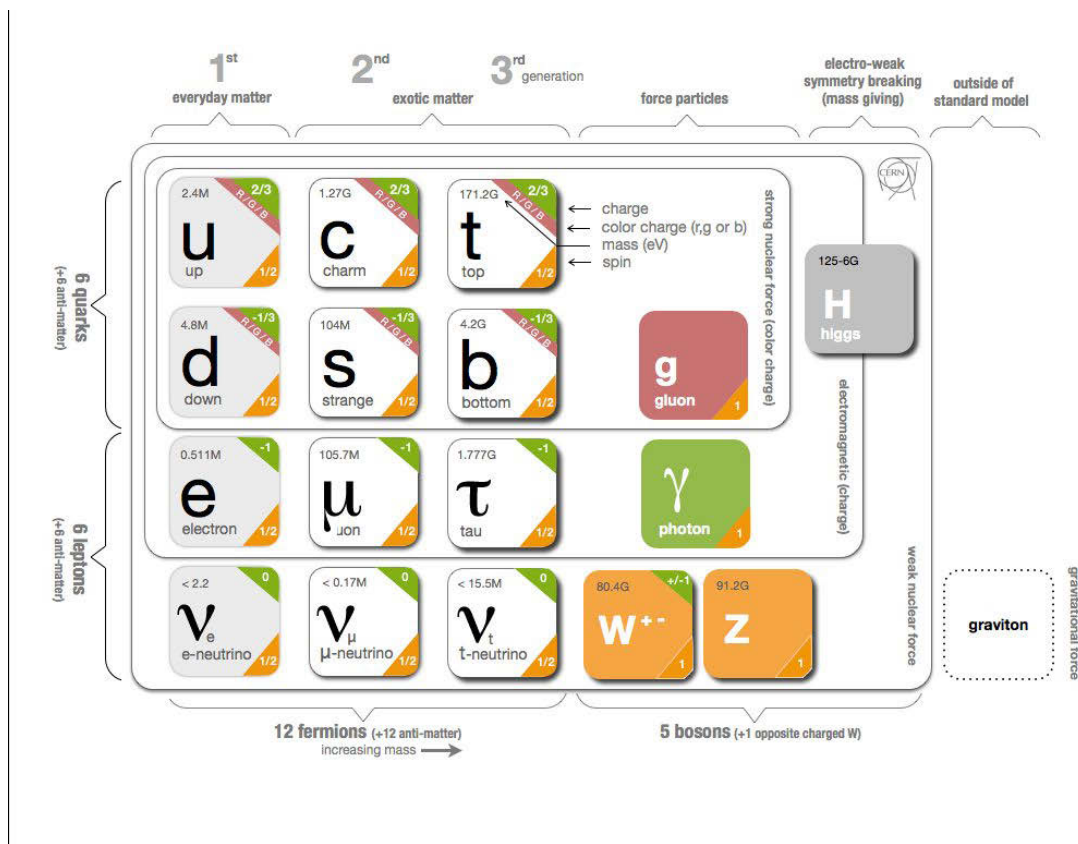


Figure 4.1: The Standard Model. [38].

Standard Model. This is what we now refer to as the Higgs Mechanism. When the W and Z bosons interact with the Higgs field, they obtain mass. This new field results in yet another boson - the Higgs boson.

4.3 Vector Boson Fusion

There are several possible Higgs production mechanisms. Two of the more prominent methods are gluon fusion and vector boson fusion. Gluon fusion processes are expected to be the dominant mechanism, see Figure 4.2 [36]. Vector boson fusion, however, has a feature which make it a favorable discovery channel - forward jets, which will be covered in more detail in Chapter 6. In vector boson fusion, two quarks radiate virtual W or Z bosons, which in turn inverse decay (or fuse) to produce a Higgs boson. A Feynman diagram of this process is shown in Figure 4.3.

4.3.1 Higgs Decay Products

The Higgs itself will not be directly detectable. Instead it is the decay products of the Higgs which will be identified and reconstructed to form the hypothesis of the Higgs Boson. CMS Higgs searches for the Higgs boson are primarily focused on five decay channels: Higgs to two photons, Higgs to ZZ to 4 leptons, Higgs to WW, Higgs to tau tau, and Higgs to $b\bar{b}$. For a summary of CMS Higgs search results, see Chapter 8.

This study focuses on the Higgs to tau tau decay channel (see Figure 4.3). More specifically, it focuses on the specific case where both tau particles decay leptonically, which means that each tau decays to an electron or muon and respective

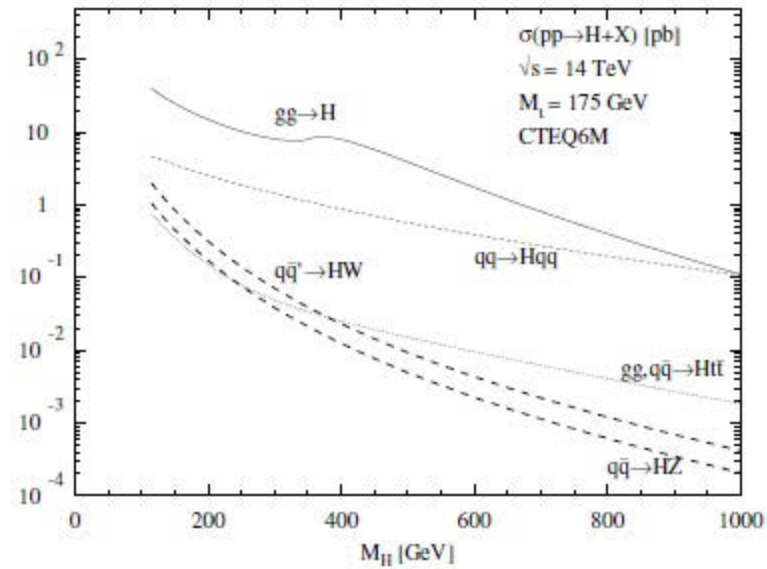


Figure 4.2: Higgs cross section for various production mechanisms as a function of Higgs mass. Of particular note are gluon fusion (shown on graph as $gg \rightarrow H$) and vector boson fusion (shown on graph as $qq \rightarrow Hqq$.)

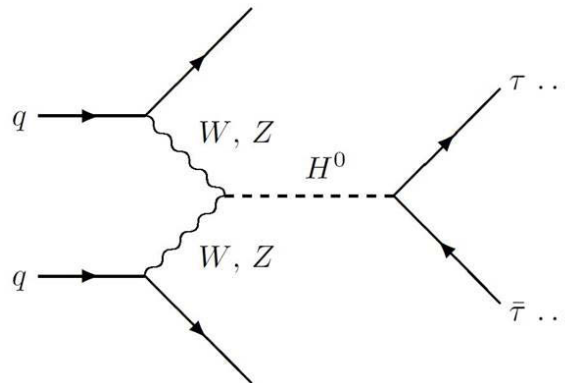


Figure 4.3: Feynman diagram of a vector boson fusion Higgs decaying into two tau particles.

neutrinos. Note that the tau is the only lepton heavy enough to decay hadronically. Hadronic decays of the tau cannot be effectively modeled using the mass reconstruction methods which will be detailed in Chapter 5, therefore this decay channel is not appropriate for this particular study. For studies involving semi-leptonic tau decays (one tau decay is leptonic, the other hadronic), see [42] and [43].

4.4 Data Set

Two data sets were used in the analysis that follows in the rest of this chapter through Chapter 7. The results presented in these chapters were originally described in [48]. Monte Carlo data samples from the summer of 2008 for qqH , $H \rightarrow \tau \tau$ with Higgs masses of 115 and 130 GeV were used. The 115 GeV data set contains 158340 events, and the 130 GeV data set contains 124381 events. The data sets used are:

`/H115_tautau_2l/Summer08_IDEAL_V11_redigi_v1/GEN-SIM-RECO`

`/H130_tautau_2l/Summer08_IDEAL_V11_redigi_v1/GEN-SIM-RECO`

In these data sets, the τ particles are forced to decay leptonically, therefore this data set does not contain events where the decay of one or both of the τ particles is hadronic. In reality however, the branching ratios for the τ decays must be taken into consideration. The branching ratio of the τ decaying into an electron and two neutrinos is 17.85%, and the ratio of it decaying into a muon and two neutrinos is 17.36% [44]. Therefore the branching ratio of the τ decaying leptonically into either electrons or muons is $17.85\% + 17.36\% = 35.21\%$, and the branching ratio for both

τ particles decaying leptonically is thus $(0.3521)^2 = 0.1240$, or 12.40%. So while the number of $q\bar{q}H, H \rightarrow \tau\tau$ events in which both τ particles decay leptonically is not large, it is still quite significant.

4.5 The $q\bar{q}H \rightarrow \tau\tau \rightarrow$ Leptons Signal

In this channel, the Higgs decays to two τ particles, each of which decays into a lepton (electron or muon) and two corresponding neutrinos. The η and p_T distributions of the leptons, both at the generator level as well as reconstructed, are shown in Figures 4.4, 4.6, 4.5, and 4.7.

While direct access to the neutrinos is possible at the generator level in the simulated data, direct information about the neutrinos is not accessible in real LHC data. Therefore we must look at missing transverse energy (\cancel{E}_T) to determine the energy from the neutrinos. If all decay results from the collision are detectable except for neutrinos, and the collision energy is precisely known, conservation of energy can be used to determine how much energy is missing. This missing transverse energy (\cancel{E}_T) can then be attributed to the undeposited energy from the neutrinos. In this study, both generated and reconstructed \cancel{E}_T have been used. In this study, when generated \cancel{E}_T is mentioned, it should be noted that it is not the generated \cancel{E}_T obtained directly from the dataset. The generated \cancel{E}_T in this study was calculated by looping over all stable generator level particles, excluding neutrinos, and then multiplying by -1. The missing transverse momentum (\cancel{p}'_T) distributions (obtained from the corresponding \cancel{E}_T objects in the data) for both generated and reconstructed level

objects are shown in Figures 4.8 and 4.9, respectively.

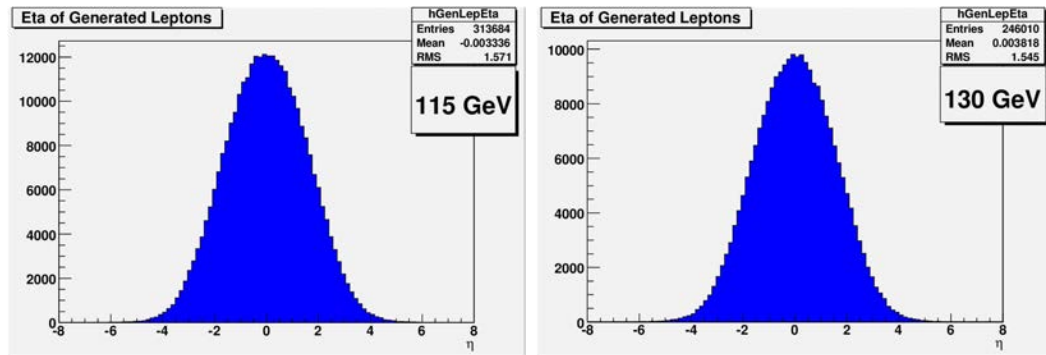


Figure 4.4: η of generated leptons for 115 and 130 GeV Higgs boson decaying to taus.

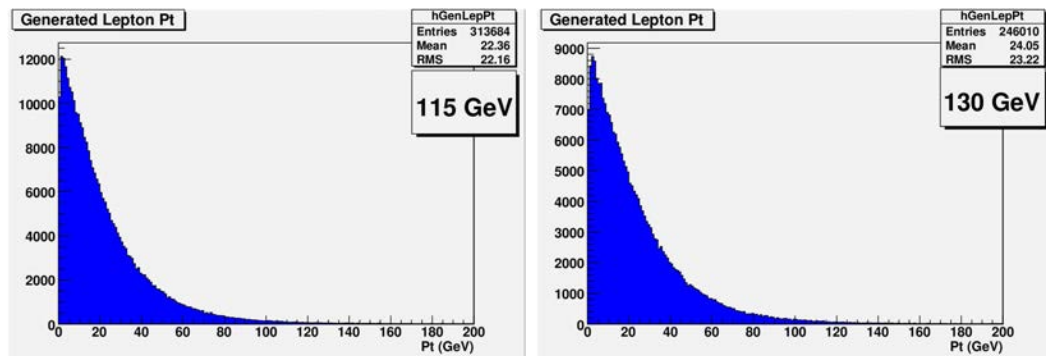


Figure 4.5: p_T of generated leptons for 115 and 130 GeV Higgs boson decaying to taus.

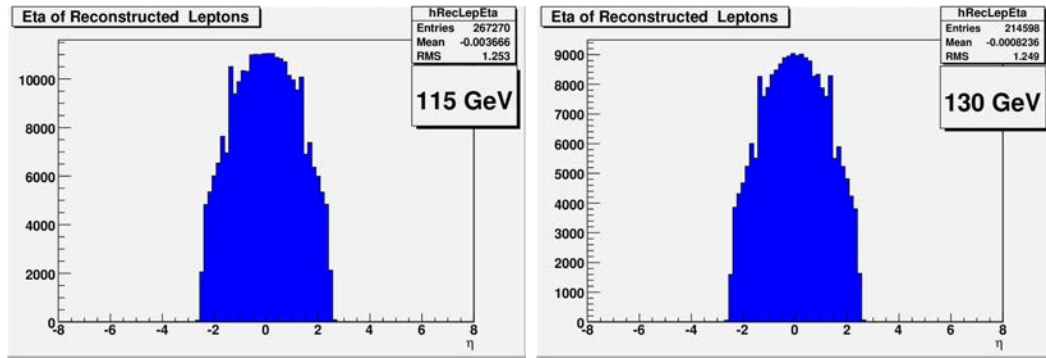


Figure 4.6: η of reconstructed leptons for 115 and 130 GeV Higgs decaying to taus.

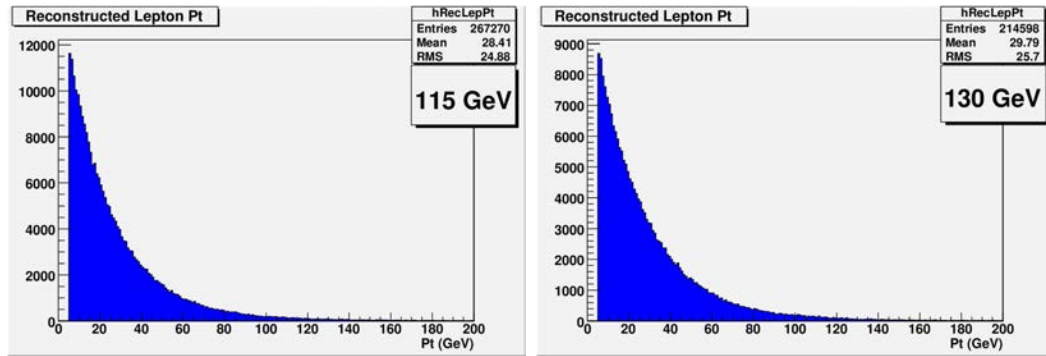


Figure 4.7: p_T of reconstructed leptons for 115 and 130 GeV Higgs decaying to taus.

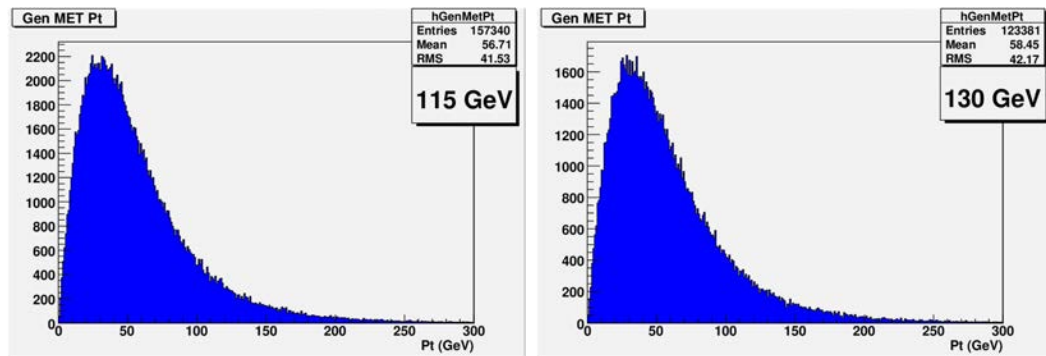


Figure 4.8: Generator level p_T (indicated as Gen MET Pt on the graph) for 115 and 130 GeV Higgs decaying to taus.

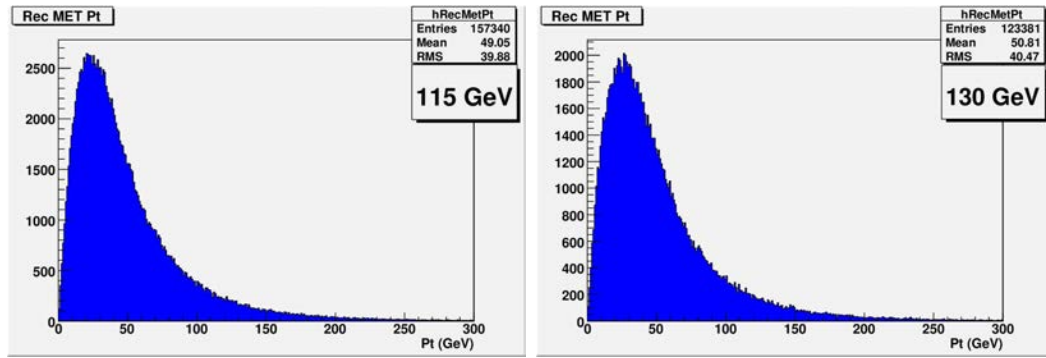


Figure 4.9: Reconstructed level p_T (indicated as Rec MET Pt on the graph) for 115 and 130 GeV Higgs decaying to taus.

CHAPTER 5 MASS RECONSTRUCTION METHODS

5.1 Higgs Mass Reconstruction

According to Rainwater and Zeppenfeld [45], the mass of the Higgs can be determined using a collinear approximation. In this approximation, the mass of the Higgs can be constructed if two quantities are known. The first quantity required is the mass of the final state leptons (muons or electrons). The second quantity is the fraction of the τ 's momentum that is carried by the neutrinos. With these quantities, the mass of the Higgs is given by $M_H \cong \frac{M_l}{\sqrt{X_1 X_2}}$, where M_H is the mass of the Higgs, M_l is the final state mass of the leptons, and X_1 and X_2 are the fractions of each τ momentum carried by their corresponding neutrino pairs.

In addition, the neutrinos should be relatively close to their corresponding leptons in eta/phi space. As seen in Figure 5.1, the separation between leptons and neutrinos is generally quite small (on the order of a couple degrees), although a few events do have a significantly larger angle. A small separation between the neutrinos and the leptons implies that by knowing the direction of the leptons, the direction of the neutrinos (and thus the \cancel{E}_T) is known, and thus for the purposes of this study, that the direction of the τ particles is known. This allows the construction of the Higgs invariant mass, as opposed to just the transverse mass.

In this study two different mass reconstruction methods have been applied [47]. From this point on, they will simply be referred to as Method 1 and Method 2.

In the following two subsections, only generator level information is used in order to establish the methods. Reconstructed Higgs masses using detector level reconstructed objects will be described in the following chapter.

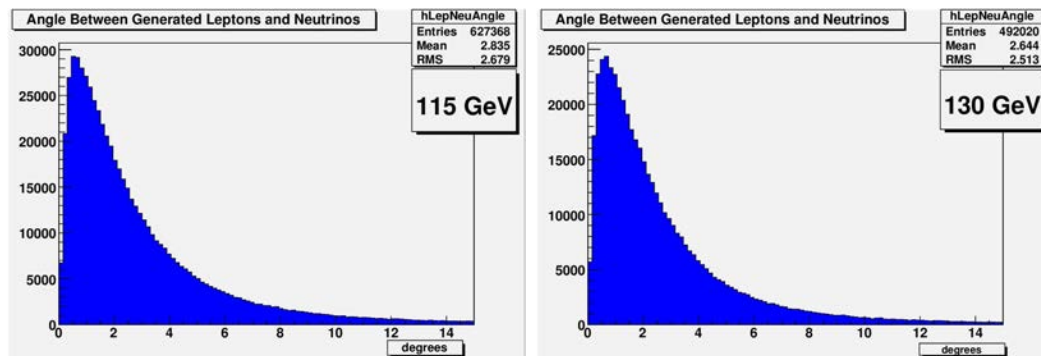


Figure 5.1: Angle (in degrees) between generator level leptons and neutrinos for 115 and 130 GeV Higgs.

5.1.1 Method 1

In Method 1, the \cancel{E}_T in the transverse plane is calculated, with the assumption that the same momentum ratio will be valid on the z -axis as well. The neutrino pair from each τ is then treated as a single particle, using the above information to calculate a mass for each neutrino pair. The mass of the Higgs is thus the sum of the dilepton mass and the two neutrino pair masses, or $M_H = M_{ll} + M_{12} + M_{34}$, where M_{ll} is the final state mass of the leptons, and M_{12} and M_{34} are the masses of each neutrino pair. Method 1 gives a rather broad mass peak, with a mean close to the correct mass, but it has a rather large high mass tail. Reconstructed Higgs masses

using generator level information are shown in Figure 5.2.

5.1.2 Method 2

Method 2 utilizes the collinear approximation formula from Rainwater and Zeppenfeld[45] to reconstruct the Higgs mass. In order to make use of this formula, it is necessary to find X_1 and X_2 . In Method 2, all of the \cancel{E}_T is added to one of the leptons in the transverse plane. Then the cross product of this quantity with the momentum of the other lepton is calculated. The ratio of the cross product of the momentum of the two leptons to the the \cancel{E}_T added cross product is then assumed to give X . For more information on this reconstruction method, see [46].

$$X_1 = \frac{l_1 \cdot p_x \cdot l_2 \cdot p_y - l_1 \cdot p_y \cdot l_2 \cdot p_x}{l_2 \cdot p_y (l_1 \cdot p_x + \cancel{p}_{T_x}) - l_2 \cdot p_x (l_1 \cdot p_y + \cancel{p}_{T_y})}$$

$$X_2 = \frac{l_1 \cdot p_x \cdot l_2 \cdot p_y - l_1 \cdot p_y \cdot l_2 \cdot p_x}{l_1 \cdot p_x (l_2 \cdot p_y + \cancel{p}_{T_y}) - l_1 \cdot p_y (l_2 \cdot p_x + \cancel{p}_{T_x})}$$

The dilepton mass M_{ll} is shown in Figure 5.4. Since X_1 and X_2 are fractions, $0 < X_1 < 1$, and $0 < X_2 < 1$. In addition, the restriction $X_1^2 + X_2^2 < 1$ is also imposed. These restrictions provide the first necessary cuts for Method 2. X_1 and X_2 are shown without cuts in Figure 5.5. Method 2 does give fewer events than Method 1 (see Table 5.1), but the mass peak is dramatically narrower, and the high mass tail is absent. Reconstructed Higgs masses using generator level information are shown in Figure 5.3.

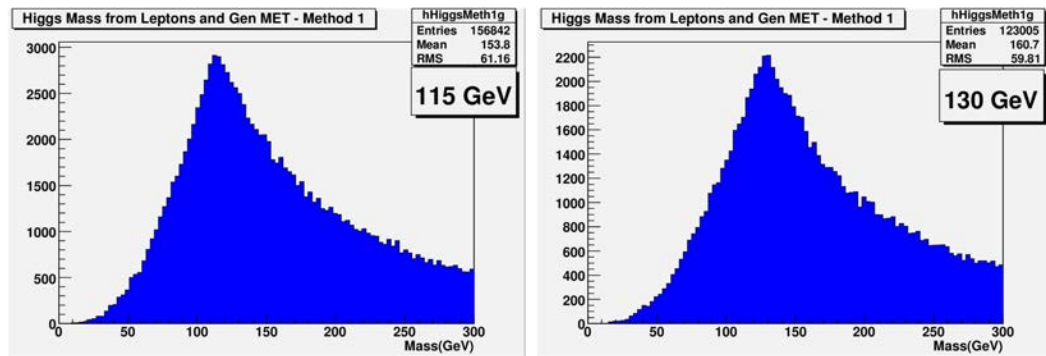


Figure 5.2: Mass reconstruction of 115 and 130 GeV Higgs using generated leptons and E_T , Method 1.

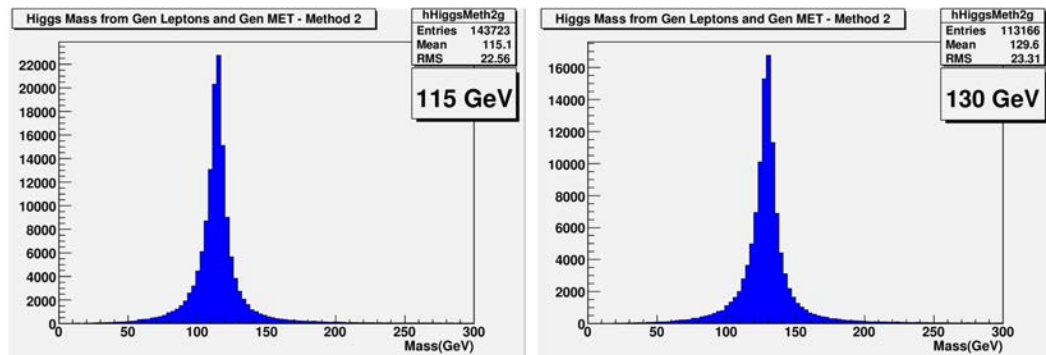


Figure 5.3: Mass reconstruction of 115 and 130 GeV Higgs using generated leptons and E_T , Method 2.

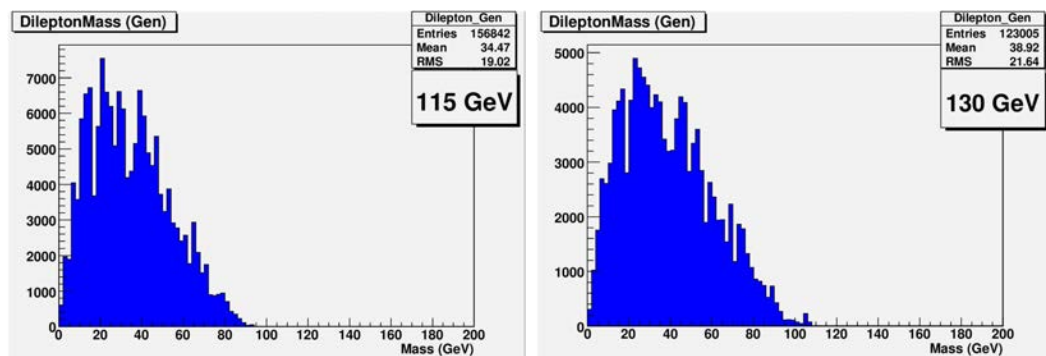


Figure 5.4: Dilepton mass for 115 and 130 GeV Higgs from generated leptons.

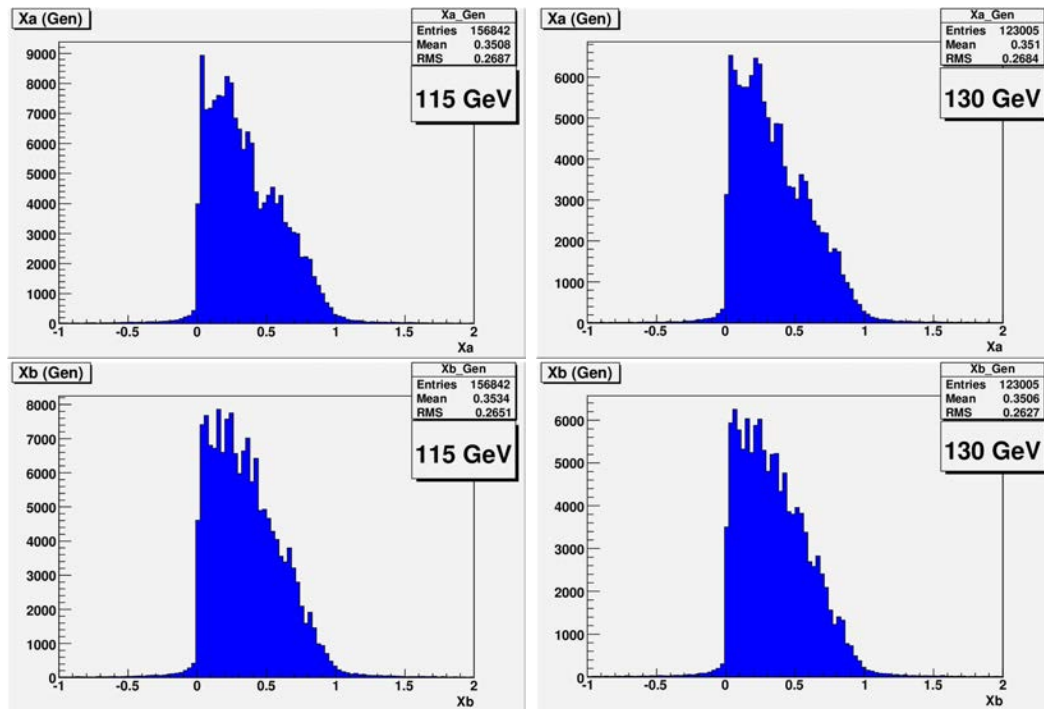


Figure 5.5: X_1 and X_2 (labeled as X_a and X_b in figure) for 115 and 130 GeV Higgs from generated leptons and \cancel{E}_T .

Table 5.1: Number of events per file, as well as the number of Higgs mass reconstructions for Method 1 and Method 2 using generator level information.

	115 GeV	130 GeV
Events in File	158340 (3706 fb^{-1})	124381 (4450 fb^{-1})
Method 1 (Gen level leptons and \cancel{E}_T)	156842 (3671 fb^{-1})	123005 (4401 fb^{-1})
Method 2 (Gen level leptons and \cancel{E}_T)	143723 (3364 fb^{-1})	113166 (4049 fb^{-1})

CHAPTER 6 FORWARD JET TAGGING

6.1 Forward Jets

As first discussed in Section 4.3, in the vector boson fusion process two quarks radiate W or Z bosons which fuse to create a Higgs boson. The initial quarks hadronize into jets which can be detected at forward angles. So in addition to the final state decay products, the signal from this channel also contains these forward jets, which are useful in distinguishing the Higgs signal from that of background processes. While several different reconstructed jet algorithms are available, only IterativeCone5CaloJets have been used in this study. The p_T of these reconstructed jets is shown in Figure 6.1. As seen in this figure, there are a large number of low p_T jets ($p_T \lesssim 10\text{GeV}$). While most events do contain more than two jets, the jets of interest are the forward tagging jets. To be selected as a forward jet pair, the jets were required to meet the following requirements:

1. $\eta_{j1} \cdot \eta_{j2} < 0$
2. $\Delta\eta \geq 4.5$
3. The p_T of each jet must be higher than the p_T cut. p_T cuts of 10, 20 and 30 GeV were imposed.

The η distribution of the forward jet pairs for all three p_T cuts is shown in Figure 6.2.

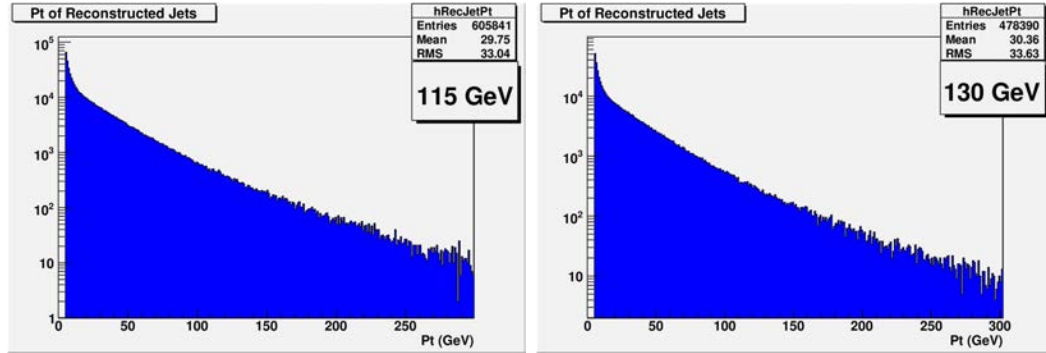


Figure 6.1: p_T of reconstructed jets for 115 and 130 GeV Higgs.

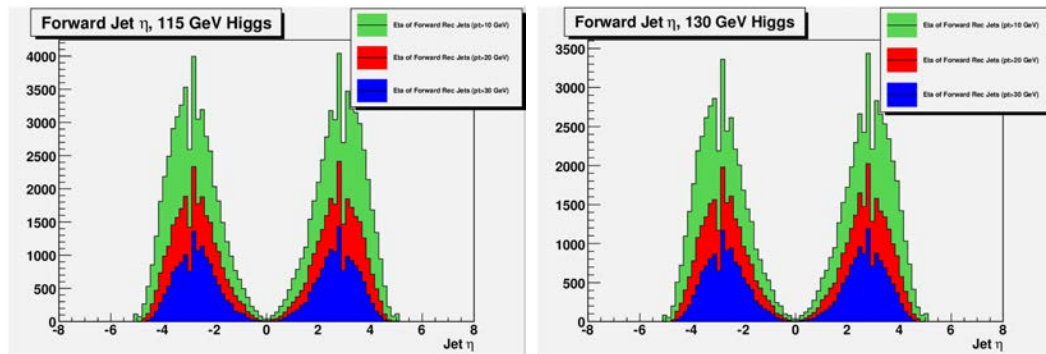


Figure 6.2: η of forward jets for 115 and 130 GeV Higgs.

6.2 Combining Forward Jet Tagging with Mass Reconstruction Methods

As the mass reconstruction using all generator level information for Method 2, and to a lesser extent, Method 1, look reasonable, with a clearly discernable mass peak near the generated Higgs mass for each dataset, the next step is to apply mass reconstruction to detector level reconstructed leptons and \cancel{E}_T . Method 2 has three significant advantages over Method 1:

1. The mass peak for Method 2 is much narrower than that of Method 1.
2. Method 2 does not have the problematic high mass tail of Method 1.
3. Method 2 can be applied using only reconstructed leptons and \cancel{E}_T , while Method 1 would require the use of reconstructed τ 's.

Due to these reasons, Method 1 was abandoned for this study and the focus was shifted to applying only Method 2 to the reconstructed detector level objects.

The reconstructed leptons used were MuonCollection and GsfElectronCollection, for muons and electrons, respectively. Ideally, each event would contain two oppositely charged leptons, whether it be two electrons, two muons, or one muon and one electron. However, that is not the case. The multiplicity of reconstructed leptons is shown in Figure 6.3. Mass reconstruction was only attempted on those events which had exactly one positively charged and one negatively charged lepton.

The dilepton mass M_{ll} is shown in Figure 6.4. As mentioned before, since X_1 and X_2 are fractions, $0 < X_1 < 1$, and $0 < X_2 < 1$. In addition, $X_1^2 + X_2^2 < 1$. X_1 and X_2 are shown without cuts in Figure 6.5. It should be noted that when using reconstructed data, there are a significantly larger number of cases where these values do not fall between 0 and 1. In most cases this is due to the angular separation between the leptons and the \cancel{E}_T being too large (see Section 5.1).

For these methods to be truly productive, these mass peaks must be observable over the presence of background events. These background events are other processes with final state similar to the channel of interest. In this particular study, that primarily means processes with a two lepton final state. See Chapter 7 for more about background events. The forward jets present in this channel should be useful in reducing the background. In preparation for using the jets as a way to filter out the background, the forward jet cuts previously mentioned (See Figure 6.2) were applied. Figures 6.6 and 6.7 show the Higgs mass reconstruction using Method 2 using reconstructed leptons and reconstructed \cancel{E}_T with forward jet cuts applied. The remaining number of events after each cut can be found in Table 7.1. Although the number of events does decrease as the threshold of the jet p_T cuts increases, the overall shape is not affected greatly.

Figure 6.8 superimposes the Higgs mass using only generator level objects and only reconstructed level objects onto the same histogram. As can be seen in these histograms, the mass peak is significantly broader when reconstructed level objects are used, and the position of the peak decreases by several GeV. The histograms are

normalized to the same number of events (y axis is in arbitrary units).

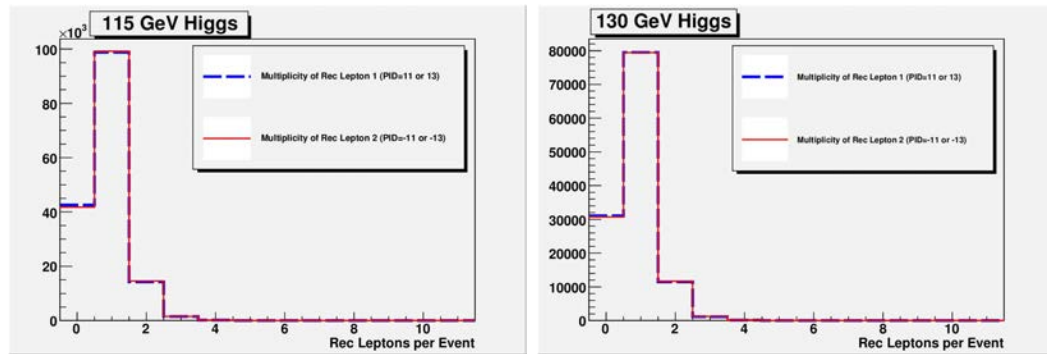


Figure 6.3: Multiplicity of reconstructed leptons (PID=11 corresponds to electrons, 13 to muons).

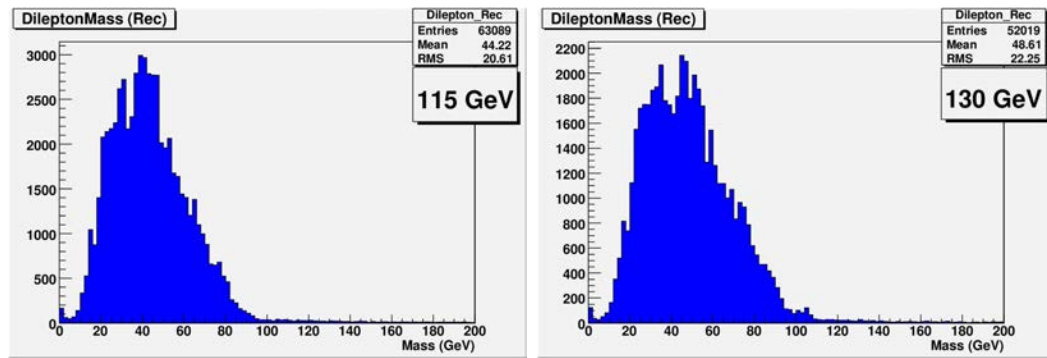


Figure 6.4: Dilepton mass for 115 and 130 GeV Higgs from reconstructed leptons.

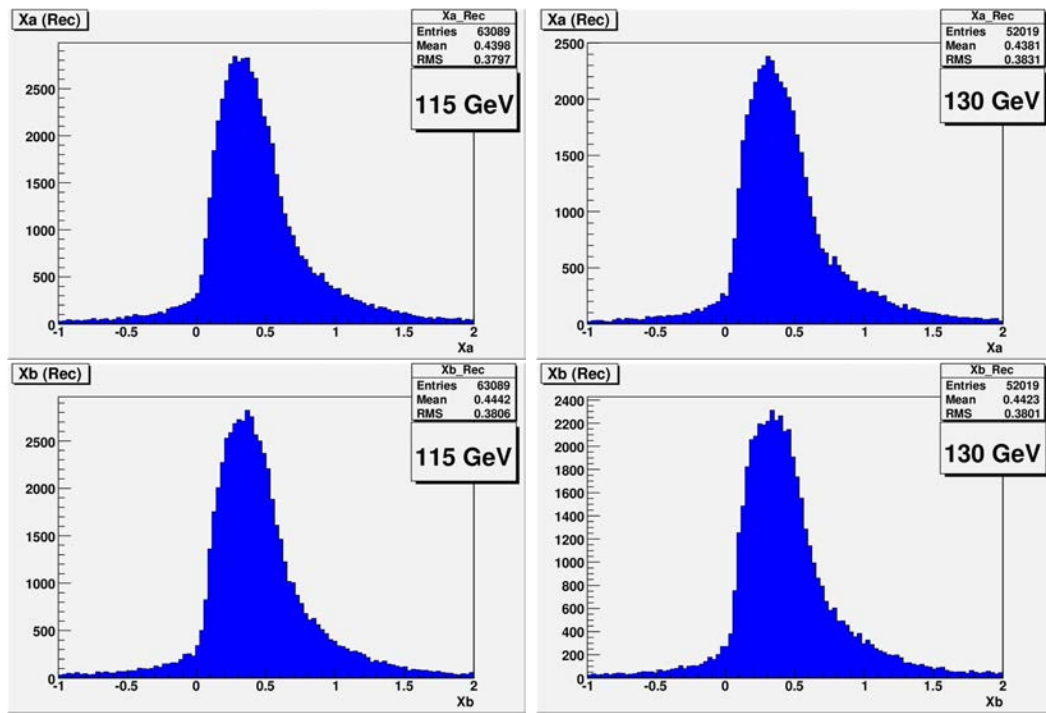


Figure 6.5: X_1 and X_2 (labeled as X_a and X_b in figure) for 115 and 130 GeV Higgs from reconstructed leptons and \cancel{E}_T .

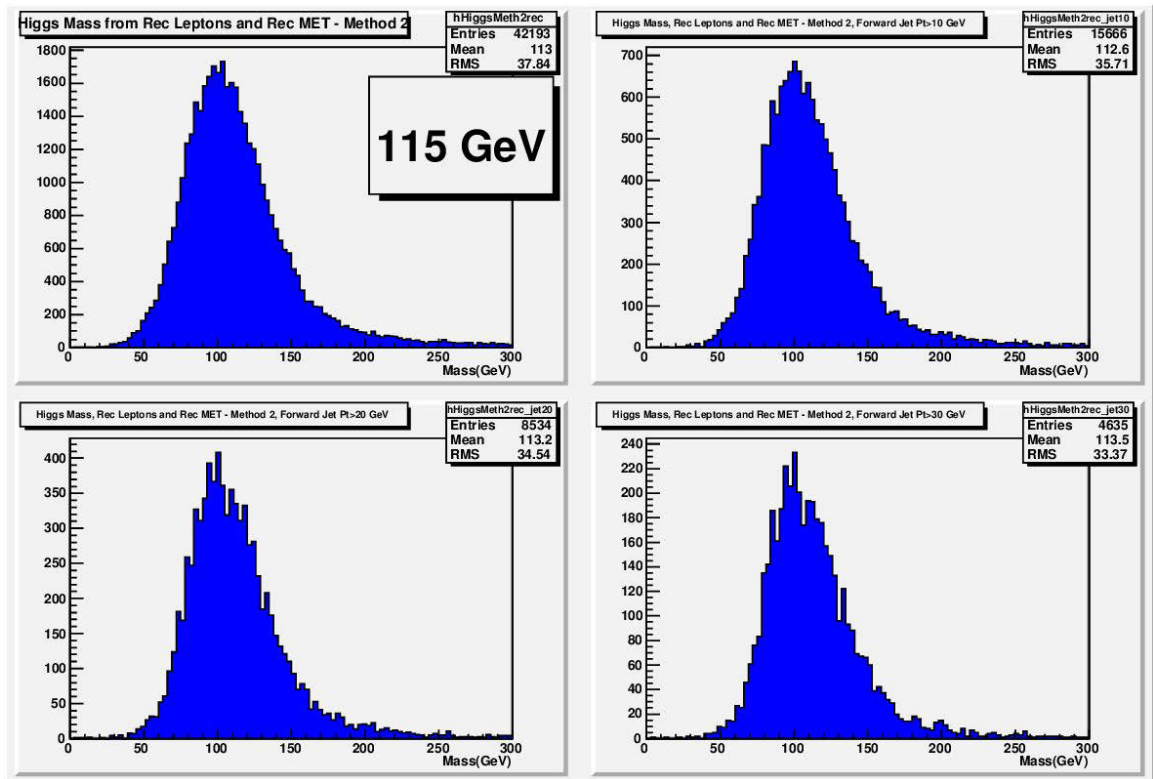


Figure 6.6: Results of forward jet p_T cuts on Higgs mass reconstruction (115 GeV Higgs, Method 2). The top left histogram does not make use of forward jet cuts. For the remaining three histograms, jet $\Delta\eta > 4.5$, and $\eta_{j_1}\eta_{j_2} < 0$. The top right histogram is for jet $p_T > 10$ GeV, bottom left for jet $p_T > 20$ GeV, and the bottom right for jet $p_T > 30$ GeV.

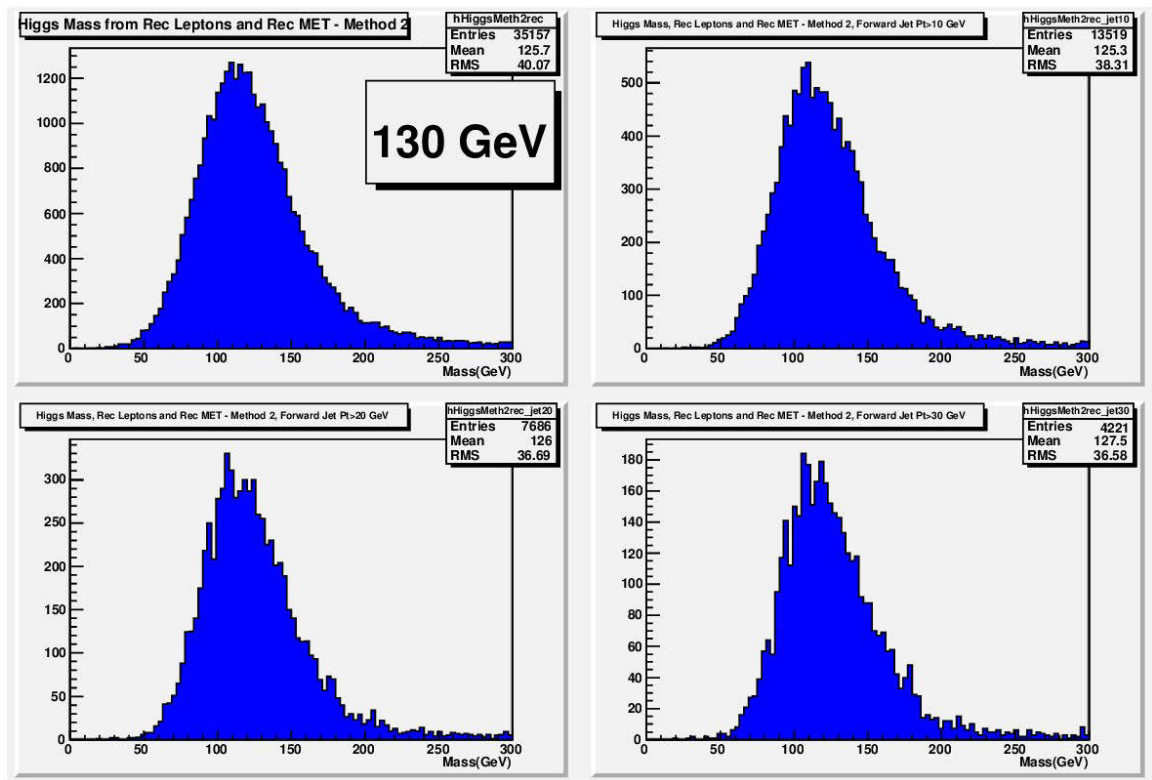


Figure 6.7: Results of forward jet p_T cuts on Higgs mass reconstruction (130 GeV Higgs, Method 2). The top left histogram does not make use of forward jet cuts. For the remaining three histograms, jet $\Delta\eta > 4.5$, and $\eta_{j1}\eta_{j2} < 0$. The top right histogram is for jet $p_T > 10$ GeV, bottom left for jet $p_T > 20$ GeV, and the bottom right for jet $p_T > 30$ GeV.

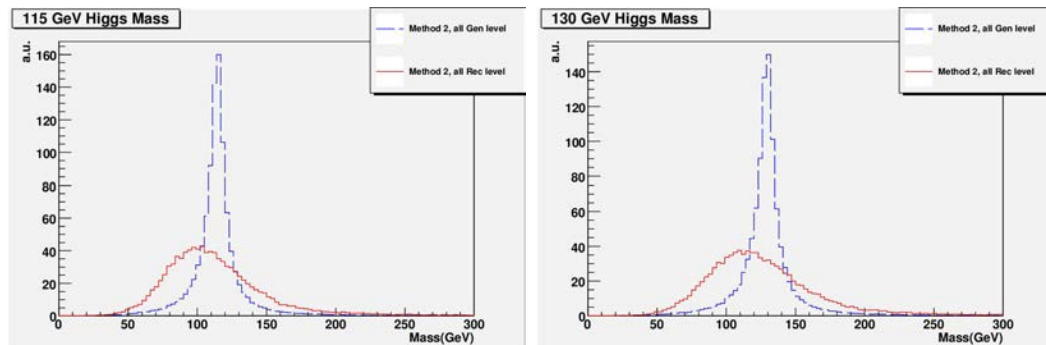


Figure 6.8: Mass of 115 GeV and 130 GeV Higgs using Method 2, gen level and rec level results superimposed on same histogram. The y axis is in arbitrary units.

CHAPTER 7 APPLYING MASS RECONSTRUCTION METHODS AND FORWARD JET TAGGING TO BACKGROUNDS

7.1 Use of Forward Jet Tagging to

Reduce Background

The previously mentioned cuts were designed to eliminate background processes from the Higgs signal. Method 2 was applied to certain significant background channels using the same cuts applied to the Higgs datasets. The Monte Carlo datasets which model the backgrounds along with the number of events per file and the number of events remaining in each background file are shown in Table 7.1. The results shown in Table 7.1 were used with the corresponding cross sections and branching ratios [36] to determine the number of remaining events from each process in 30 fb^{-1} of data, see Table 7.2. A stack plot of these backgrounds is shown in Figure 7.1. The significance was calculated using $S = \sqrt{2 \ln Q}$ with $Q = (1 + \frac{N_S}{N_B})^{N_S + N_B} e^{-N_S}$, where N_S is the number of signal events, and N_B is the number of combined background events remaining in 30 fb^{-1} of data using the 30 GeV jet p_T cut, see Table 7.3. The number of expected events before and after jet based cuts (minimal cuts based on X_1 and X_2 are included in both plots) are also displayed as a histogram in Figure 7.2. As can be seen from these tables and plots, these cuts do eliminate a large fraction of the total background events, although more stringent cuts are needed as the significance is still very low (0.279 for 115 GeV and 0.205 for 130 GeV). It should also be noted that this study is also severely limited by statistically small background samples, as

small background datasets were weighted based on their corresponding cross sections.

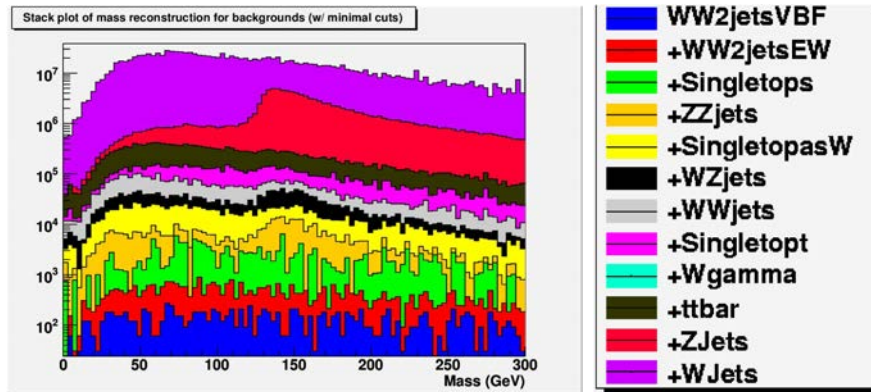


Figure 7.1: This stack plot shows the result of applying the mass reconstruction method to the background processes in the Higgs search.

7.2 Discussion of Method 2 and Forward

Jet Tagging

Method 2 gives a sharper mass peak, and does not have the large high mass tail as seen in Method 1. The focus from this point on will be on Method 2, although conditions in the future with real collision data may suggest a reexamination of Method 1. When Method 2 is applied to all detector level objects, as well as with forward jet cuts, the number of events which survive all cuts is somewhat small, although these methods reduce the number of background events at a higher rate. The focus of this study up to this point has been largely on the methods used to reconstruct the mass of a low mass Standard Model Higgs formed through VBF processes, decaying into two τ particles, both of which decay leptonically.

Table 7.1: Number of events remaining after p_T cuts on jets for signal and backgrounds.

Data Set	Total Events	10 GeV	20 GeV	30 GeV
115 GeV Higgs	158340	15666	8534	4635
130 GeV Higgs	124381	13519	7686	4221
W+Jets	9970000	510	111	43
Z+Jets	1287404	1104	96	45
Ttbar+Jets	1000000	3761	1146	529
Single Top t-channel	281756	765	299	136
Single Top s-channel	11999	12	4	1
Single Top associated W	169048	586	182	78
W+gamma	102012	29	4	0
WW+Jets	204722	196	47	20
WZ+Jets	236550	358	95	34
ZZ+Jets	199810	308	70	19
WW+2Jets (electroweak)	39299	509	347	257
WW+2Jets (VBF)	21868	558	383	245

Table 7.2: Number of events expected in 30 fb^{-1} of data for various jet p_T cuts. Note that for both Higgs entries, the cross section given is actually the cross section times the branching ratio for the leptonic decay channel of interest to this study.

Data Set	Cross Section(pb)	10 GeV	20 GeV	30 GeV
115 GeV Higgs	0.04272	127	69	38
130 GeV Higgs	0.02795	91	52	28
W+Jets	40000	61384	13360	5176
Z+Jets	3700	94329	8203	3845
Ttbar+Jets	414	46712	14233	6570
Single Top t-channel	130	10589	4139	1882
Single Top s-channel	5	150	50	13
Single Top associated W	29	3016	937	401
W+gamma	292	2.5	0.34	0
WW+Jets	74	2125	510	217
WZ+Jets	32	1453	386	138
ZZ+Jets	10.5	486	110	30
WW+2Jets (electroweak)	0.942	366	250	185
WW+2Jets (VBF)	0.41	314	215	138

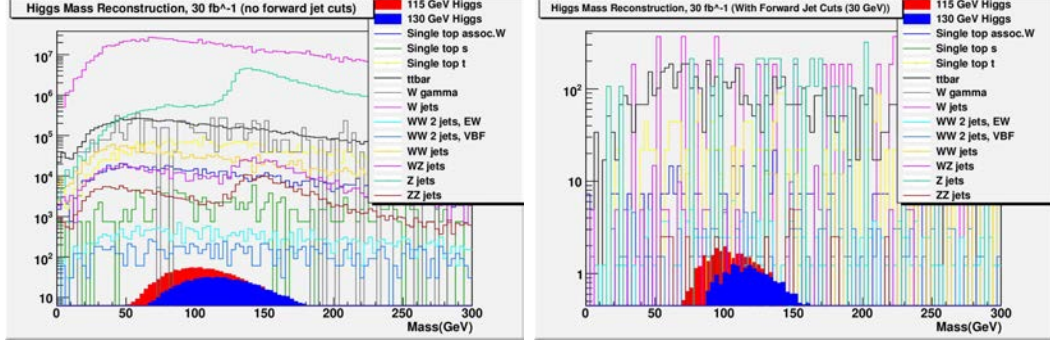


Figure 7.2: Reconstructed mass of the Higgs and backgrounds in GeV. The left figure is with minimal cuts while the right figure includes jet based cuts.

Table 7.3: Significance for 115 and 130 GeV datasets with backgrounds $S = \sqrt{2\ln Q}$, $Q = (1 + \frac{N_S}{N_B})^{N_S+N_B} e^{-N_S}$ (30 GeV jet p_T cut).

Data Set	Significance
115 GeV Higgs	0.279
130 GeV Higgs	0.205

The methods explored in this study show promise in reconstructing the Higgs mass in the $qqH \rightarrow \tau \tau \rightarrow$ leptons channel for a low mass Higgs. This method could prove especially interesting as a new boson consistent with the expected properties of the Higgs boson has been discovered at the LHC with a mass of about 125 GeV [49], [50]. Method 2 from this study could have considerable use in the further studies of this new boson. A brief overview of CMS results of this new discovery will be discussed in the next chapter.

CHAPTER 8 CMS RESULTS: THE HIGGS BOSON

8.1 Experimental Results

The Higgs to two photons(Figure 8.1) and Higgs to ZZ to 4 leptons (Figure 8.1)channels are considered high mass resolution channels, and contribute significantly to the CMS Higgs search reported in [50].

Three low mass resolution channels were also included in the same study: Higgs to WW (Figure 8.3) , Higgs to tau tau(Figure 8.4), and Higgs to bb (no data shown). The Higgs to tau tau channel is largely dominated by Z to tau tau background events. With improved forward jet tagging methods similar to those discussed in Chapters 6 and 7, the mass reconstruction method discussed in Chapter 5 could have real value in improving results for this channel. The Higgs to bb channel actually has the largest branching fraction of the decay modes discussed, but is a significant challenge due to the signal being overwhelmed by QCD b quark production.

Figure 8.5 shows the confidence level for all five decay channels mentioned above. It excludes the Higgs with a 95% confidence level for masses of 110-121.5 GeV. In the range 121.5-128 GeV this study cannot exclude the existence of the Higgs. Masses above 128 GeV were previously excluded in [51]. The most likely mass of the Higgs is about 125 GeV.

8.2 Nobel Prize for Englert and Higgs

The Nobel Prize in Physics 2013 was jointly awarded to Francois Englert and Peter W. Higgs for "the theoretical discovery of a mechanism that contributes to our understanding of the origin of mass of subatomic particles, and which recently was confirmed through the discovery of the predicted fundamental particle, by the ATLAS and CMS experiments at CERN's Large Hadron Collider".

The discovery of the Higgs boson is not the end of the story. Much work continues on the study of this newly discovered particle, including, but not limited to, better measurements of its mass, experimental evidence of which production methods yield a Higgs boson, and experimental evidence of the Higgs decaying into specific channels.

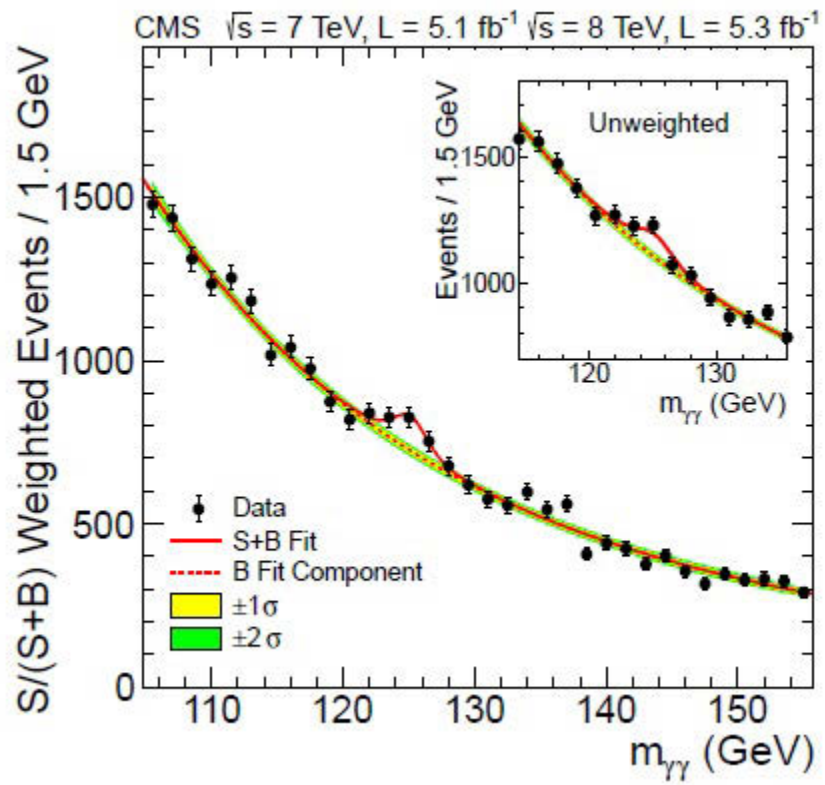


Figure 8.1: Di-photon mass for Higgs decay to two photons.[50].

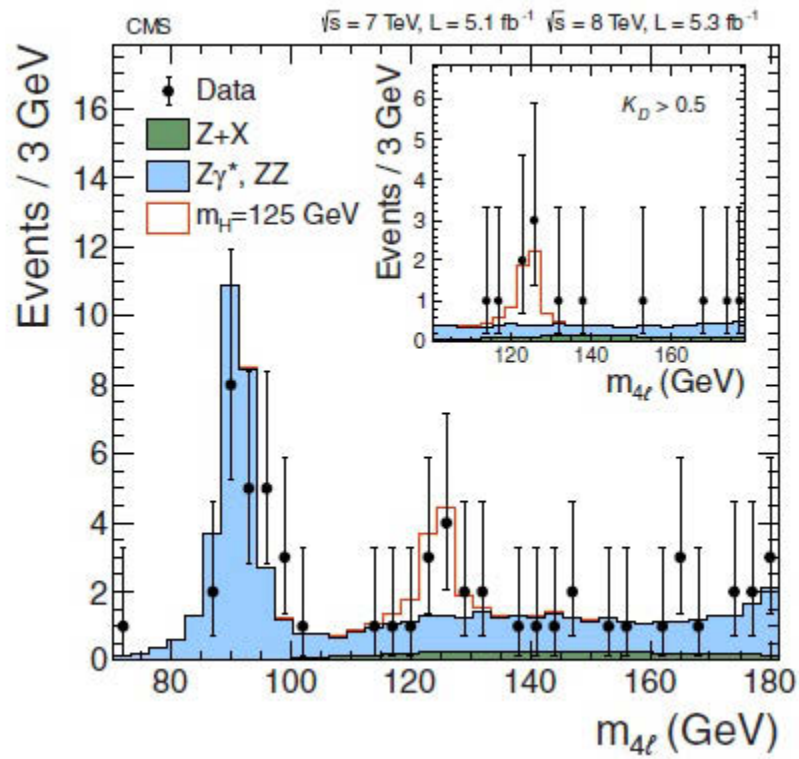


Figure 8.2: Four-lepton mass for Higgs decay to ZZ to four leptons.[50].

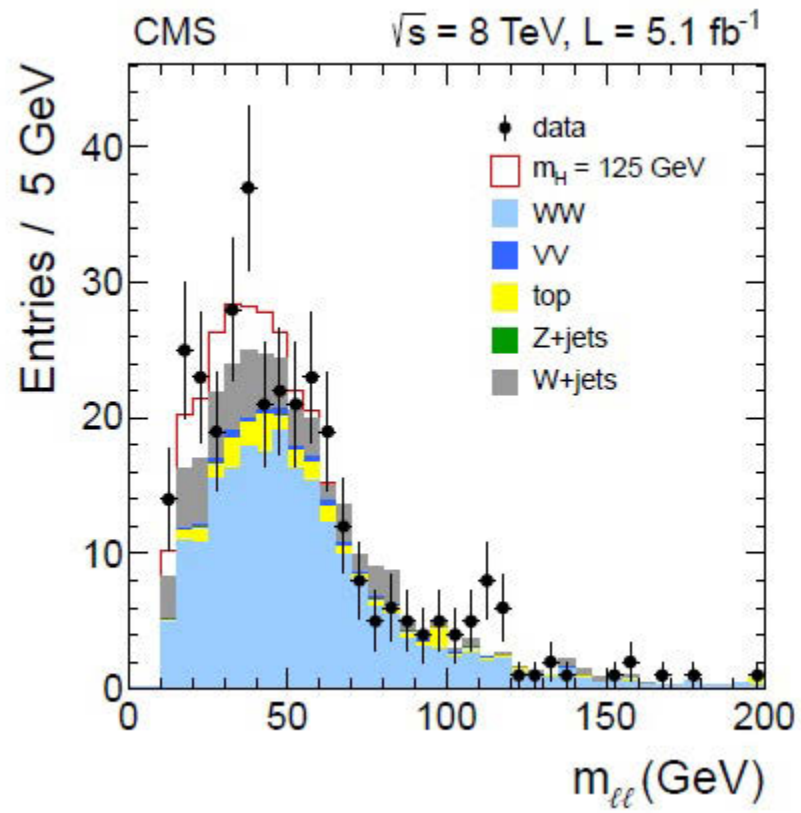


Figure 8.3: Di-lepton mass for Higgs decay to WW to two leptons.[50].

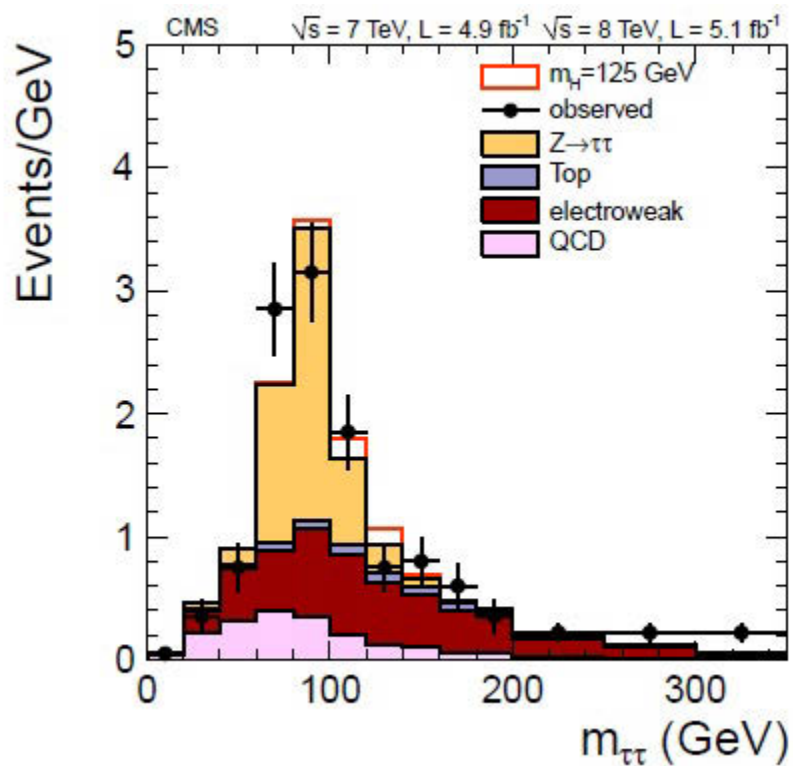


Figure 8.4: Di-tau mass for Higgs decay to two taus.[50].

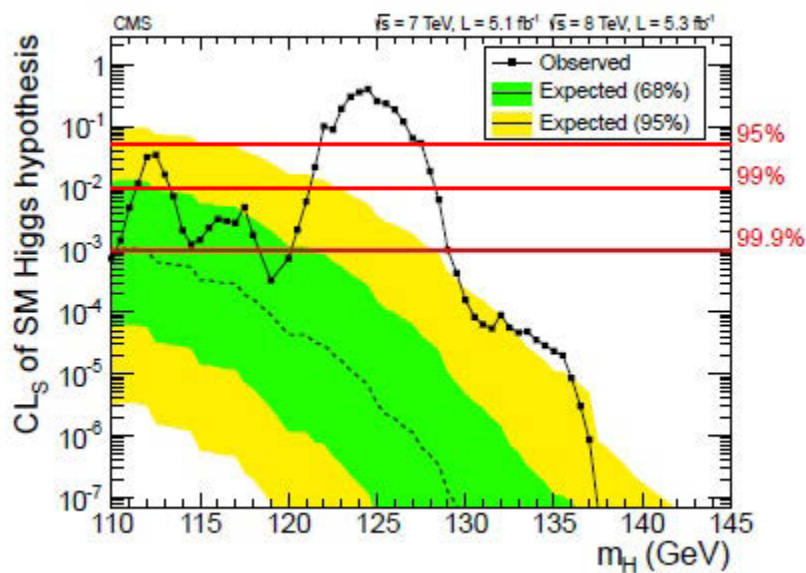


Figure 8.5: Combined confidence level for multiple Higgs decay channels.[50].

CHAPTER 9

TYING IT ALL TOGETHER: A BRIEF STUDY ON THE IMPORTANCE OF HF TO FORWARD JET TAGGING

9.1 Conclusion: HF PMT Hits

A modified HF simulation that includes the PMT windows as sensitive detectors shows that some component of hadronic showers can leak out the back of HF. Cerenkov radiation from charged particles passing through the PMT windows creates large anomalous signals, in agreement with the testbeam results from 2004. These PMT window events must be able to be efficiently tagged or eliminated for HF to give correct information. Although the rate of these events is small (less than 1%), they are still extremely problematic. If not properly identified as PMT hits, such high energy events could be mistaken for actual high energy hits, which could then be mistaken for indications of new physics. This will be even more important in the near future when the LHC is upgraded to even higher center of mass collision energies. With higher collision energies, it may be possible to discover new physics, one example being Supersymmetry. In Supersymmetry, every currently discovered elementary particle has a corresponding superpartner. Every integer spin boson would have a half-integer spin fermion as its superpartner, and every fermion would have a boson as its partner. If Supersymmetry is correct, the Supersymmetric particles must be at higher masses than can be discovered at current collision energies. With higher collision energies, it may be possible to discover Supersymmetry (or other new physics) at the LHC. If this is to happen, PMT hits must not be misidentified as high

energy indications of new physics such as supersymmetry.

While several methods such as timing or energy sharing ratios involving long and short fiber energies were investigated to try to tag PMT hits, it was determined that they were not sufficient. In the end, it was decided that the existing PMTs must be replaced. The new PMTs have a window which is thinner and has a smaller area. The smaller area means that fewer particles will actually hit the window. A thinner window means that those particles which do hit the window will create less Cerenkov radiation, resulting in much smaller signals which would likely fall below jet energy threshold cuts. In other words, these events would be eliminated in the low energy noise and never make it into the data. Additionally, these new windows have four anodes. A normal event coming through the fibers and light guides should have photons striking three or four anodes, but a PMT hit would most likely only hit one anode. This would allow PMT hit detection algorithms that could eliminate any events that might be energetic enough to make it past jet energy thresholds. These new PMTs should allow high energy events in HF to be seen as possible indications of new physics, and not a problem with the detector.

9.2 Conclusion: Higgs Mass Reconstruction

Methods

When used on simulated Higgs data in the $qqH \rightarrow \tau \tau \rightarrow$ Leptons channel at 115 and 130 GeV, the mass reconstruction method referred to as Method 2 gives a nice, clear peak at the appropriate mass. Although Method 1 did not give such clear

results and was largely abandoned in favor of Method 2 for the majority of this study, it did give a somewhat reasonable mass peak, and may be worth investigating in more detail in the future.

When forward jet tagging is applied to both the Higgs and background events, the background events are reduced at a much higher rate, even though more background events remain than signal.

The methods explored in this study show promise in reconstructing a low mass Higgs, which is especially important with the recent discovery of the Higgs boson at the LHC, at a mass of about 125 GeV. As mentioned in Chapter 8, the tau tau channel is considered a low mass resolution channel. With this mass reconstruction method and corresponding forward jet tagging, it may be possible to confirm the Higgs in this particular channel. More importantly, using the methods discussed here, it may be possible to more precisely measure the mass of the Higgs.

As can be seen in Figure 9.1 [53], the Higgs production cross section increases significantly with increasing collision energy. Note that in the figure, the vector boson fusion process is split into WW and ZZ fusion, and are the second and third lines from the top, respectively. As the LHC increases in energy, the number of Higgs bosons produced should increase significantly, allowing much more precise Higgs studies. Additionally, future colliders with center of mass energies 10-15 times that of the LHC could increase Higgs production by more than an order of magnitude.

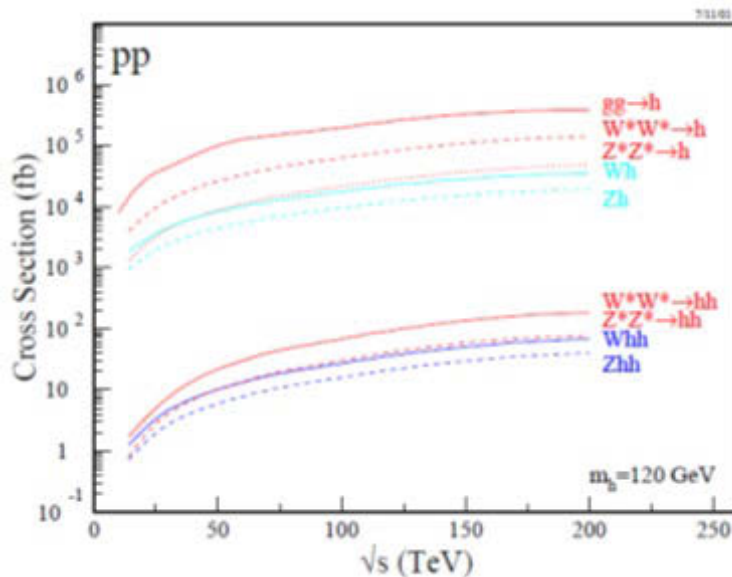


Figure 9.1: Total cross section for single and double Higgs boson production for various production mechanisms as a function of collision energy for a Higgs mass of 120 GeV.

9.3 A Connection between Chapters 2-3 and 4-8

Up to this point it may seem that that the HF PMT simulation study detailed in Chapters 2-3 and the Higgs mass reconstruction study are two entirely unrelated topics, and in some respects, this is true. However, there is a very real connection between having a forward detector which gives a correct picture of what is happening at angles near the beamline and being able to use forward jet tagging in a vector boson fusion study.

As previously discussed in Chapters 6-7, the qqH signal includes forward jets which are not present in many prominent background signals. By requiring that an event contains a pair of forward jets, it should be possible to eliminate many of the

background channels, making it possible to separate the Higgs from the background processes.

It must be possible to find the forward jets to make full use of the mass reconstruction methods described in Chapter 5. If HF gives such spurious signals as the abnormal events described in Chapter 2, it is very possible that these events will show up as fake jets. If the abnormal event problem was deemed significant enough that HF was taken offline completely, then many forward tagging jets would not be detected at all.

9.4 Forward Jets from $qqH \rightarrow \tau \tau \rightarrow$ Leptons

Signal in HF

As one way of checking how important HF would be to detecting new physics using forward jet tagging, the same Monte Carlo data used in Chapters 4-7 was used to see how many of the forward tagging jets would be lost if HF were not online.

As previously described in Chapter 6, to be selected as a forward jet pair, the jets were required to meet the following requirements:

1. $\eta_{j1} \cdot \eta_{j2} < 0$
2. $\Delta\eta \geq 4.5$
3. The p_T of each jet must be higher than the p_T cut. p_T cuts of 10, 20 and 30 GeV were imposed.

As can be seen in Figure 9.2 and Table 9.1, 67-78% of jet pairs have at least one jet with $|\eta| > 3$. As this is in the range of HF coverage, this means that if HF

is not functioning properly, then a very large fraction of forward jets could not be identified. A fully functional HF is essential in order to maximize the new physics discovery potential of the LHC and of the CMS detector in particular.

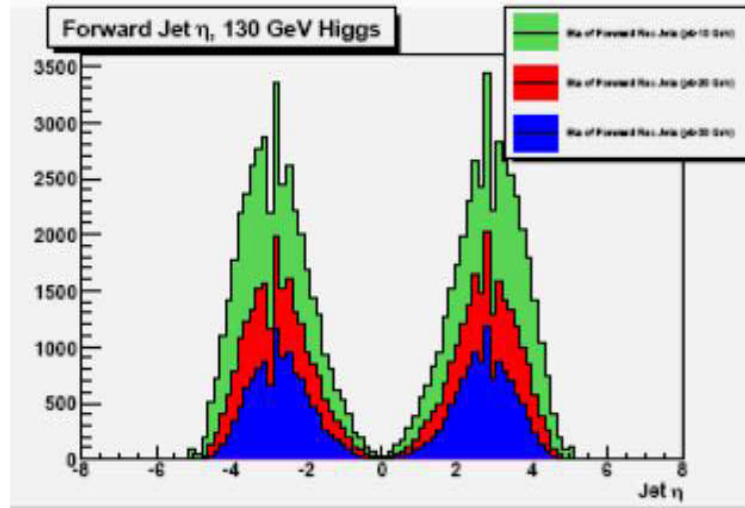


Figure 9.2: Forward jets from Higgs mass reconstruction study.

Table 9.1: Forward jet pairs from Higgs mass reconstruction study which have at least one jet in the HF region. The colors in the first column refer to Figure 9.1

	Total Jet Pairs	At least one jet with $ \eta >3$	% of Total Jet Pairs
10 GeV Cut (green)	41785	32571	78%
20 GeV Cut (red)	22252	16143	73%
30 GeV Cut (blue)	11858	7992	67%

REFERENCES

- [1] J.J. Thomson. "Cathode Rays". *Philosophical Magazine* 44: 293 (1897).
- [2] Wolfgang K. H. Panofsky. *The Evolution of Particle Accelerators & Colliders*, (PDF), Stanford, 1997.
- [3] M. Conversi, E. Pancini, O. Piccioni. "On the Disintegration of Negative Muons". *Physical Review* 71 (3): 209 (1947).
- [4] *Nature* 159, 186 - 190 & 160, 453 - 456 (1947).
- [5] *Nature* 159, 126 - 127 (1947).
- [6] G.D. Rochester, C.C. Butler. "Evidence for the Existence of New Unstable Elementary Particles". *Nature* 160 (4077): 855 (1947).
- [7] History of the Bevatron (Video documentary written and produced by Diane LaMacchia.) Lawrence Berkeley Laboratory, University of California (1993).
- [8] O. Chamberlain, E. Segre, C. Wiegand, T. Ypsilantis. "Observation of Antiprotons". *Physical Review* 100 (3): 947 (1955).
- [9] E.D. Bloom *et al.* "High-Energy Inelastic ep Scattering at 6 and 10". *Physical Review Letters* 23 (16): 930 (1969).
- [10] M. Breidenbach *et al.* "Observed Behavior of Highly Inelastic Electron-Proton Scattering". *Physical Review Letters* 23 (16): 935 (1969).
- [11] J.J. Aubert *et al.* "Experimental Observation of a Heavy Particle J". *Physical Review Letters* 33 (23):1404 (1974).
- [12] J.-E. Augustin *et al.* "Discovery of a Narrow Resonance in e+e- Annihilation". *Physical Review Letters* 33 (23): 1406 (1974).
- [13] M.L. Perl *et al.* "Evidence for Anomalous Lepton Production in e+e- Annihilation". *Physical Review Letters* 35 (22): 1489 (1975).
- [14] S.W. Herb *et al.* "Observation of a Dimuon Resonance at 9.5 GeV in 400-GeV Proton-Nucleus Collisions". *Physical Review Letters* 39 (5): 252 (1977).

- [15] J.J. Aubert *et al.* (European Muon Collaboration). "The ratio of the nucleon structure functions F_2^N for iron and deuterium". Physics Letters B 123 (3–4): 275 (1983).
- [16] G. Arnison *et al.* (UA1 collaboration). "Experimental observation of lepton pairs of invariant mass around 95 GeV/ c^2 at the CERN SPS collider". Physics Letters B 126 (5): 398 (1983).
- [17] F. Abe *et al.* (CDF collaboration). "Observation of Top quark production in $p\bar{p}$ Collisions with the Collider Detector at Fermilab". Physical Review Letters 74 (14): 2626–2631 (1995).
- [18] S. Arabuchi *et al.* (D0 collaboration). "Observation of the Top Quark". Physical Review Letters 74 (14): 2632–2637 (1995).
- [19] LHC: The Guide. <http://cds.cern.ch/record/1165534/files/CERN-Brochure-2009-003-Eng.pdf>
- [20] Bruning, Oliver Sim (ed.) *et al.* *LHC Design Report , v.1 : the LHC Main Ring* **CERN-2004-003-V-1** (2004).
- [21] Bruning, Oliver Sim (ed.) *et al.* *LHC Design Report , v.2 : the LHC Infrastructure and General Services.* **CERN-2004-003-V-2** (2004).
- [22] Benedikt, Michael (ed.) *et al.* *LHC Design Report , v.3 : the LHC Injector Chain* **CERN-2004-003-V-3** (2004).
- [23] S. Abdullin *et al.* "Design, Performance, and Calibration of CMS Forward Calorimeter Wedges". Published in EPJ C, Vol 53, No 1 (2008). **CMS Note 2006/044.**
- [24] N. Akchurin and R. Wigmans. Review of Scientific Instruments, Vol 74, No 6 (2002).
- [25] R. Wigmans. Oxford University Press (2000), *Calorimetry: Energy Measurement in Particle Physics.*
- [26] W.-M. Yao *et al.* *Review of Particle Physics*, J. Phys. G 33, 1 (2006).
- [27] The specifics of the Hamamatsu R7525 PMTs are given at http://sales.hamamatsu.com/assets/pdf/parts_R/R7525.pdf
- [28] A. Moeller *et al.* "Analysis of Abnormally High Energy Events in CMS Forward Calorimeters" **CMS IN 2008/014**(2008).

- [29] S. Banerjee *et al.* "Calorimetry Task Force Report" **CMS Note 2010/007**(2010).
- [30] A. Moeller *et al.* "Simulation of PMT Hits in HF for Single Particles and Pythia Jets" **CMS DN 2010/004**(2010).
- [31] A. Moeller *et al.* "Simulation of PMT Hits in HF for Minimum Bias Events" **CMS DN 2010/010**(2010).
- [32] A. Moeller *et al.* "A Comparison of Two Different PMT Window Thicknesses for the Simulation of PMT Hits in HF" **CMS DN 2010/012**(2010).
- [33] B. Bilki *et al.* "Tests of CMS HF Candidate PMTs with Muons" **CMS DN 2009/011**(2009).
- [34] CMS Collaboration. *CMS Physics TDR: Volume I, Detector Performance and Software*. **CERN-LHCC-2006-001**.
- [35] B. Bilki *et al.* "Study of Various Photomultiplier Tubes with Muon Beams And Cerenkov Light Produced in Electron Showers" **CMS Note 2010/003** (2010).
- [36] CMS Collaboration. *CMS Physics TDR: Volume II, Physics Performance*. **CERN-LHCC-2006-001**.
- [37] D. Griffiths. *Introduction to Elementary Particles*. New York, USA: John Wiley & Sons, 1987.
- [38] A. Purcell. "Go on a particle quest at the first CERN webfest", CERN Bulletin, Issue No. 35-36/2012. <http://cds.cern.ch/journal/CERNBulletin/2012/35/NewsArticles/1473657>.
- [39] P.Higgs. "Broken Symmetries and the Masses of Gauge Bosons". Physical Review Letters 13 (16): 508509 (1964).
- [40] F. Englert and R. Brout. "Broken Symmetry and the Mass of Gauge Vector Mesons". Physical Review Letters 13 (9): 321323 (1964).
- [41] D. Green. Vector boson fusion Higgs production at the LHC: Mass variables, arXiv:hep-ex/0501027 (2005).
- [42] CMS Collaboration."Towards the Search for the Standard Model Higgs boson produced in Vector Boson Fusion and decaying into a τ pair in CMS with 1 fb^{-1} : τ identification studies", *CMS PAS CMS PAS HIG-08-001* (2009).

- [43] CMS Collaboration. "Search for the Standard Model Higgs boson produced in Vector Boson Fusion and decaying into a τ pair in CMS with 1 fb^{-1} ", *CMS PAS CMS PAS HIG-08-008* (2009).
- [44] C. Amsler *et al.* (Particle Data Group), *Physics Letters B* 667, 1 (2008).
- [45] T. Plehn, D. L. Rainwater, D. Zeppenfeld. "A Method for identifying $H \rightarrow \tau\tau \rightarrow e^\pm\mu^\mp p_T$ at the CERN LHC", *Phys. Rev. D* 61, 093005, 2000.
- [46] ATLAS Collaboration. "Expected performance of the atlas experiment - detector, trigger and physics," Dec 2008. [Online]. Available: <http://arxiv.org/abs/0901.0512>.
- [47] Firdevs Duru. "R and D Studies On the Hadronic Calorimeter and Physics Simulations on the Standard Model and Minimal Sypersymmetric Standard Model Higgs Bosons in the CMS Experiment" (PhD Thesis, University of Iowa, 2007), 119-125.
- [48] A. Moeller. *et al.* "Mass Reconstruction Methods for qqH, $H \rightarrow \tau\tau \rightarrow$ Leptonic Decay" **CMS AN 2009/187** (2009).
- [49] S. Chatrchyan *et al.* [CMS Collaboration]. "A New Boson with a Mass of 125 GeV Observed with the CMS Experiment at the Large Hadron Collider," *Science* **338**, 1569 (2012).
- [50] CMS Collaboration. "Observation of a new boson at a mass of 125 GeV with the CMS experiment at the LHC", *Phys. Lett. B* 716 (2012).
- [51] CMS Collaboration. Combined results of searches for the standard model Higgs boson in pp collisions at $\sqrt{s} = 7 \text{ TeV}$, *Phys. Lett. B* 710 (2012).
- [52] "The Nobel Prize in Physics 2013". Nobelprize.org. Nobel Media AB 2013. http://www.nobelprize.org/nobel_prizes/physics/laureates/2013.
- [53] U. Baur *et al.* Report of the Working Group Physics at future colliders, in APS/DPF/DPB Snowmass study, Proceedings of the APS/DPF/DPP Summer Study on the Future of Particle Physics, Snowmass, Colorado, 2001.